

AD-A034 679

HONEYWELL CORPORATE RESEARCH CENTER BLOOMINGTON MINN

F/G 20/6

STRAIN INDUCED WAVEGUIDING IN OPTICAL MATERIALS FOR INTEGRATED --ETC(U)

DEC 76 D CHEN, B KOEPKE, C KNUDSON

N00014-75-C-1097

UNCLASSIFIED

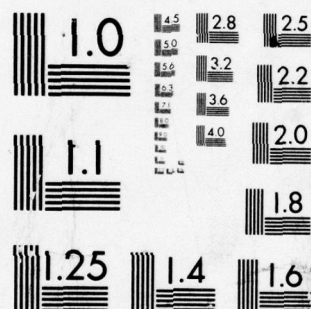
HR-47024

NL

1 OF 2

AD  
A034679





MICROCOPY RESOLUTION TEST CHART  
NATIONAL BUREAU OF STANDARDS-1963-A



ADA034679

STRAIN INDUCED WAVEGUIDING IN  
OPTICAL MATERIALS FOR  
INTEGRATED OPTICS APPLICATION

by

D. Chen, B. Koepke, C. Knudson and G.B. Hocker

Honeywell Inc.  
Corporate Research Center

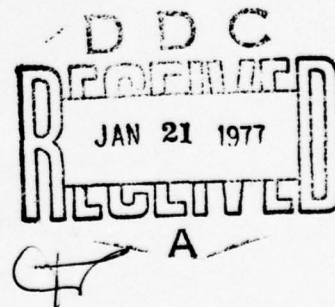
Final Technical Report

1 May 1975 to 30 September 1976

December 1976

Research Supported by  
Office of Naval Research  
Arlington, Virginia, 22217  
Contract No. N00014-75-C-1097

FC  
(12)



DISTRIBUTION STATEMENT A  
Approved for public release;  
Distribution Unlimited

UNCLASSIFIED

SECURITY CLASSIFICATION OF THIS PAGE (WHEN DATA ENTERED)

REPORT DOCUMENTATION PAGE		READ INSTRUCTIONS BEFORE COMPLETING FORM
1. REPORT NUMBER	2. GOV'T ACCESSION NUMBER	3. RECIPIENT'S CATALOG NUMBER
4. TITLE (AND SUBTITLE) STRAIN INDUCED WAVEGUIDING IN OPTICAL MATERIALS FOR INTEGRATED OPTICS APPLICATION.		5. TYPE OF REPORT/PERIOD COVERED Final rept. 1 May 1975 - 30 September 1976.
7. AUTHOR(S) D./Chen, B./Koepke, C./Knudson and G. B./Hocker		6. PERFORMING ORG. REPORT NUMBER HR-47024
9. PERFORMING ORGANIZATIONS NAME/ADDRESS Honeywell Inc., Corporate Research Center 10701 Lyndale Ave S., Bloomington, MN 55420		8. CONTRACT OR GRANT NUMBER(S) N00014-75-C-1097 NEW
11. CONTROLLING OFFICE NAME/ADDRESS Office of Naval Research Department of Navy Arlington, Virginia 22217		10. PROGRAM ELEMENT, PROJECT, TASK AREA & WORK UNIT NUMBERS
14. MONITORING AGENCY NAME/ADDRESS (IF DIFFERENT FROM CONT. OFF.) 12 117p.		12. REPORT DATE December 1976
		13. NUMBER OF PAGES 115
		15. SECURITY CLASSIFICATION (OF THIS REPORT) Unclassified
		15a. DECLASSIFICATION DOWNGRADING SCHEDULE
16. DISTRIBUTION STATEMENT (OF THIS REPORT) <del>Distribution limited to Government agencies unless released by ONR.</del> DISTRIBUTION STATEMENT A Approved for public release; Distribution Unlimited		
17. DISTRIBUTION STATEMENT (OF THE ABSTRACT ENTERED IN BLOCK 20, IF DIFFERENT FROM REPORT) Approved for public release, distribution unlimited.		
18. SUPPLEMENTARY NOTES		
19. KEY WORDS (CONTINUE ON REVERSE SIDE IF NECESSARY AND IDENTIFY BY BLOCK NUMBER) Integrated Optics, Photoelastic Effect, Strain Induced, Laser Heating, Optical Waveguide		
20. ABSTRACT (CONTINUE ON REVERSE SIDE IF NECESSARY AND IDENTIFY BY BLOCK NUMBER) Significant research results achieved under this investigation are: <ul style="list-style-type: none"> <li>Techniques for preparing laser heating strain-induced (LHSI) optical waveguides have been developed, and the properties of waveguides made with optical filter glass were obtained.</li> <li>A microprocessor-controlled LHSI optical waveguide circuit fabrication facility was constructed, and simple waveguide circuit elements were obtained.</li> </ul> → next page		

HD-168 REV 11/74

DD FORM 1 JAN 73 1473 EDITION OF 1 NOV 55 IS OBSOLETE

UNCLASSIFIED 407493

SECURITY CLASSIFICATION OF THIS PAGE (WHEN DATA ENTERED)

LB

UNCLASSIFIED

SECURITY CLASSIFICATION OF THIS PAGE (WHEN DATA ENTERED)

(20 Cont.)

cont → X-ray and optical measurement techniques were developed for the characterization of the photoelastic effect and the effect of optical polishing in selected integrated optic materials.



UNCLASSIFIED

SECURITY CLASSIFICATION OF THIS PAGE (WHEN DATA ENTERED)



# TABLE OF CONTENTS

	<u>Page</u>
SECTION I INTRODUCTION	1
SECTION II LASER HEATING STRAIN-INDUCED CHANNEL WAVEGUIDES IN GLASS	5
Techniques of Laser Heating	5
Properties of Glass for LHSI Waveguides	5
Laser Heating and Temperature Profile	6
Surface Deformation and Laser Beam	8
Refractive Index Profile	12
Residual Stresses in LHSI Waveguides	19
LHSI Waveguide Properties	26
Waveguide Mode Theory for LHSI Guides	26
Losses Due to Index Reversal in LHSI Guides	33
Properties of LHSI Waveguide	36
SECTION III FABRICATION OF LHSI WAVEGUIDE CIRCUIT ELEMENTS	43
Fabrication Technique	43
The Laser Beam Exposure System	43
Microprocessor Controlled Program	48
Properties of Waveguide Circuit Elements	57
LHSI Waveguide Constriction	57
LHSI Waveguide Bends	59
LHSI Waveguide Gaps	61
LHSI Waveguide Coupler	61
SECTION IV RESIDUAL AND INDUCED STRAIN IN WAVEGUIDE MATERIALS	64
Polishing-Induced Residual Strain	64
Waveguiding in PLZT	65
Polishing-Induced Strain in LN Crystals	65
Measurement of Photoelastic Effects	89
Measurement Technique and Theory	89
Results and Discussion	96
SECTION V CONCLUSIONS	103
REFERENCES	107

ADDITIONAL	
White Section <input checked="" type="checkbox"/>	
Built Section <input type="checkbox"/>	
UNANNOUNCED	
JUSTIFICATION	
<i>Letter on file</i>	
BY	
DISTRIBUTION/AVAILABILITY CODES	
Dist.	AVAIL. and/or SPECIAL
A	

## LIST OF ILLUSTRATIONS

<u>Figure</u>		<u>Page</u>
1	Normalized instantaneous temperature rise on the glass sample by a slow scanning focus Ar laser beam. The grid spacings are half of the Gaussian beam radius. Scanning direction is pointing towards lower right.	9
2	Normalized temperature as a function of the normalized distance along the center of the scanning track.	9
3	Profile of a laser heated ridge on Corning filter glass CS-2-60: (a) Tallysurf profile, vertical scale $0.1\mu\text{m}$ /small division, horizontal scale $100\mu\text{m}$ /major division; (b) scanning electron microscope photograph of the ridge, magnification 500X.	10
4	Ridge height $h$ as a function of the laser output power in watts for various values of scanning speed.	11
5	Ridge cross-sectional area parameter $A = h \times w$ as a function of the laser output power in watts for various values of the scanning speed.	11
6	Interference microscope photograph of the LHSI track: (a) top view where the fringes are mainly due to the raised ridge; (b) cross-sectional view which exposes the refractive index profile.	14
7	Refractive index profile of a typical LHSI waveguide.	15
8	Dependence of the peak value of the refractive index as a function of the percent laser power output used for scanning, for three different scanning speeds (100% = 1.04 watts).	16
9	Dependence of the peak value of the refractive index as a function of the scanning speed at 92% of laser power used.	17
10	Dependence of the peak value of the refractive index as a function of the defocussing distance (distance between sample surface to the laser focal point). Data obtained for 100% laser power at $47\mu\text{m}/\text{sec}$ scanning speed.	18
11	Residual stress $\sigma$ as a function of the normalized radius distance $r/a$ from the center of the LHSI track.	20
12	Photograph of fracture around an unannealed LHSI track.	23

# LIST OF ILLUSTRATIONS (Continued)

<u>Figure</u>		<u>Page</u>
13	Scanning electron micrograph of the end view of a crack of an annealed LHSI track.	23
14	Schematic diagram of residual stresses showing model of fracture experienced by the unannealed LHSI waveguide.	24
15	The normalized mode effective index $b$ as a function of the normalized guide radius $V$ for various mode number $m$ , calculated for parabolic index fibers.	31
16	Relative beam intensity at a fixed point in the LHSI waveguide as a function of the incident angle $\theta_1$ to a 45-degree glass prism ( $n = 1.8$ ) coupler for both TM and TE modes.	38
17	Relative beam intensity as a function of the LHSI waveguide path length for both the TM and TE modes.	40
18	Relative beam intensity at a fixed point in the LHSI waveguides as a function of prism input angle for a preannealed sample.	42
19	Schematic diagram of the laser beam exposure system (LBES).	44
20	Block diagram of translation stage - Microprocessor Interface (see Table 3-1 for signal mnemonics).	45
21	LBES Control Main Program flow chart.	50
22	LBES control pulse command word modification flow chart.	55
23	Relative beam intensity measured at narrow and wide part of a constructed LHSI waveguide, as a function of prism input angle. The data for the wide part are $\bullet$ - TM and $\circ$ - TE mode and those for the narrow part are X - TM and $\Delta$ - TE modes.	58
24	Photograph of a LHSI waveguide bend produced by LBES (a) dark-field photograph of waveguide (b) photograph of laser beam propagating through the bend.	60
25	Schematic of a LHSI waveguide directional coupler.	62
26	Schematic showing the Bond symmetrical diffractometer.	68



# LIST OF ILLUSTRATIONS (Continued)

<u>Figure</u>		<u>Page</u>
27	Change in diffraction angle $\Delta\theta$ caused by strain plotted as a function of diffraction angle, $\theta$ . Curves for strains of $10^{-5}$ and $10^{-6}$ are plotted.	70
28	Scanning electron micrographs showing surface structure of (0001) LN face following successive lapping and polishing operations.	72
29	Scanning electron micrographs showing surface structure of (10 $\bar{1}$ 0) LN face following successive lapping and polishing operations.	73
30	Scanning electron micrographs showing surface structure of (10 $\bar{1}$ 1) LN face following successive lapping and polishing operations.	74
31	Scanning electron micrographs showing surface structure of (11 $\bar{2}$ 0) LN face following successive lapping and polishing operations.	75
32	Waveguide effective refractive index $\beta/k$ as a function of the thickness of the waveguide region $W$ for substrate index of 2.5 and waveguide index of 2.5001, 2.501 and 2.51.	88
33	Schematic diagram of the Michelson interferometer for the measurement of photoelastic effect: f-film, C-camera, S. F. - spatial filter, B. S. -beam splitter, S. H. -sample holder, M1-main beam mirror, M2-reference beam mirror, M-corner reflector, B. E. -beam expander, P-polarizer, L-laser.	92
34	Geometry of four point loading on the sample of thickness $a$ .	92
35	Tilting of fringe lines from original unloaded condition (dotted lines).	93
36	Sample holding and loading apparatus with a sample in place.	95
37	Photograph of fringe lines (a) with no load and (b) under a load of 26.1 pounds, measured on Corning CS-2-60 glass sample.	97

# LIST OF ILLUSTRATIONS (Concluded)

<u>Figure</u>		<u>Page</u>
38	Photoelastic coefficients $p_{11}$ and $p_{12}$ of Corning CS-2-60 glass as measured from $\tan \theta/d$ vs applied force plot.	99
39	Photoelastic coefficients $p_{11}$ and $p_{12}$ of Lucite as measured from $\tan \theta/d$ vs applied force plot.	100
40	Photoelastic coefficient $p_{11}$ , $p_{12}$ , $p_{22}$ and $p_{31}$ as measured by the $\tan \theta/d$ vs applied force plot.	101

# LIST OF TABLES

<u>Table</u>		<u>Page</u>
1	Approximate Values of Loss Coefficient $\alpha$ for Various Mode Indices [ $m = 2p+1$ due to index reversal in the guide of Figure 7 using Eq. (32)].	36
2	Signal Mnemonics	46
3	Effect of Surface Treatment on Interplanar Spacing of Lithium Niobate Crystals	78
4	Percentage Change in Lattice Parameter (i.e., strain as a Function of Surface Treatment of LN Crystals)	79
5	Index Change Possibilities	85
6	Crystal and Beam Orientation for Obtaining p Values in LN	90



## PREFACE

This final report on "Strain Induced Waveguiding in Optical Materials for Integrated Optics Application", ONR Contract Number N00014-75-C-1097, covers the research progress made and results achieved during the period from May 1, 1975 to September 30, 1976. This work was carried out at Honeywell Corporate Research, under the monitoring direction of Lt. David G. Janssen and Mr. J. Trimble of the Mathematical and Information Science Division of the Office of the Naval Research.

Significant research results achieved under this investigation are summarized as follows:

- Techniques for preparing laser heating strain-induced (LHSI) optical waveguides were developed, and the properties of waveguides made with optical filter glass were obtained.
- A microprocessor-controlled LHSI optical waveguide circuit fabrication facility was constructed, and simple waveguide circuit elements were obtained.
- X-ray and optical measurement techniques were developed for the characterization of the *photoelastic effect* and the effect of optical polishing in selected integrated optic materials.

Acknowledgement:

The authors wish to express their appreciation to Lt. David Janssen and Mr. J. Trimble of the Office of Naval Research for their encouragement and direction, to Choh Li and O. N. Tufte at Honeywell Corporate Research Center for their guidance. They also wish to acknowledge the various contributions made by their colleagues at the Honeywell Corporate Research Center; especially to J. Huber for technical assistance in the various experimental phases of this work, to K. Koeneman for the construction of the laser beam exposure system, to M. Hafich for the photoelastic effect measurements, to D. Zook and E. Bernal G. for valuable discussions and suggestions, and to R. George for assistance in material evaluation.

## SECTION I

### INTRODUCTION

Techniques of guiding optical waves in planar optical materials or cylindrical optical fibers have been advancing rapidly in recent years. The major objective of this research is to explore the micro-optic fiber-optic approach for optical communication and data processing applications, with the ultimate goal of achieving integrated optical devices similar to the integrated electronics.

In the course of the integrated optics research it was observed that mechanical stress and strain can have profound effect to the waveguide properties and device performance. Stress and strain can be induced by lattice mismatch in epitaxial growth of material, by thermal expansion or contraction, by inclusion of impurities as in the diffusion operation, and by grinding and polishing of the material surface. In fact, it is safe to assume that all material surfaces exhibit some degree of the strain effect. These residual or externally induced strains modify the waveguiding properties through the photoelastic or possibly other effects. For example, in an earlier ONR-supported research effort, we have demonstrated that optical polishing on PLZT ceramic can cause sufficient refractive index increase on the material surface to result in waveguiding<sup>1</sup>.

Besides this interesting example, it is expected that similar effect can be found in other integrated optic material where the surface is prepared by optical polishing. The technique to examine the stress and strain on an optically polished surface, and the correlation of polishing induced strain to the waveguiding properties on integrated optic media are important tasks of integrated optics research.

Alternatively, an attractive technique for the fabrication of integrated optic multimode channel waveguide is to use laser heating to introduce localized strain in an otherwise uniform medium. This approach is adaptable for computer control to generate the desired multimode channel waveguide patterns.

Realizing the importance of the effect of strain on integrated optic applications, the present research was initiated by the Mathematical and Information Science Division of the Office of Naval Research, and a contract was awarded to the Honeywell Corporate Research Center to perform this research study. The first phase of the present contract began from May 1 and ended December 31, 1975. A follow-on contract was granted to cover the period ending September 30, 1976, for the initial work of the second phase research.

The objectives of this research are:

- To determine the usefulness of the strain-induced effect for integrated-optics applications. The strain induced refractive index change on suitable integrated optics materials will be of primary concern.
- To obtain basic understanding and perform measurements of the effects of strain on the various physical phenomena in optical materials useful for integrated optics applications.
- To develop device concepts using selected materials and methods. The use of laser beam heating for strain-induced integrated optic circuit will be emphasized.

These objectives have guided our research during this period of investigation. Specific tasks performed during this research effort are:



- To develop techniques of inducing controlled residual strain for optical waveguiding.
- To measure the effect of strain on selected materials and to correlate them to the properties relevant to optical waveguiding.
- To produce strain-induced planar waveguide or channel waveguide and obtain the waveguide properties.
- To fabricate simple channel waveguide circuits by laser heating.
- To construct a microprocessor controlled facility for automated fabrication of laser-induced channel waveguides.

In this final report, we present the progress made and results obtained in all the above areas. The significant progress and results are:

- Techniques for preparing laser heating strain-induced (LHSI) waveguides were obtained and the waveguide properties measured.
- Techniques for automated fabrication of LHSI waveguide circuits were developed and a microprocessor controlled fabrication facility constructed.
- X-ray and optical techniques were developed for the characterization of residual or induced strain in integrated optic materials.

The techniques and results on the laser heating strain-induced (LHSI) channel waveguide are presented in Section II. The automated method of fabricating the LHSI waveguide circuits and their properties are given in Section III. The results of introducing the residual surface strain by

polishing in PLZT and  $\text{LiNbO}_3$  and the techniques for measuring the effect of strain are presented in Section IV. Section V summarizes the progress and results made in the course of this study.

## SECTION II

### LASER HEATING STRAIN-INDUCED CHANNEL WAVEGUIDES IN GLASS

Introduction of residual strain in a uniform material medium can cause sufficient refractive index change to effect optical waveguiding. To explore the utility of this approach for fabricating multimode-channel waveguide devices, we have developed a refined laser heating strain-induced (LHSI) technique using filter glass wafers. Our approach is similar to that reported by Pavlopoulos, et al<sup>2</sup>. First, the waveguide dimension in our case is of the order of 100 $\mu$ m; therefore it is relatively easy to couple the optical beam to the waveguide. More importantly, the channel waveguide produced by the present method does not involve burning or grooving of the glass wafer, and the wave is guided in a semicylindrical channel on the surface, caused by the localized refractive index gradient due to the laser heating. In this section, the techniques of producing this type of channel waveguide, its refractive index profile, and waveguide properties are presented.

#### TECHNIQUES OF LASER HEATING

##### Properties of Glass for LHSI Waveguides

The technique of laser heating and machining has been under development since the invention of laser. The ability of achieving high energy density, high resolution and the ease of beam control make laser heating ideally suited for fabricating miniature or microscopic structures such as encountered in the microelectronics industry. To extend laser heating for the fabrication of multimode integrated optic devices, it is necessary to identify a material which will absorb the laser energy effectively for the heating laser beam and yet transmit the propagating laser beam with low loss. We have

found that the Corning red filter glass CS-2-60 satisfies this requirement. The properties of this glass, as provided by Corning Glass<sup>3</sup> are:

Corning Glass Number	Glass Type	Dopant	Thermal Expansion Coefficient ( $\times 10^{-7}$ cm/cm°C)	Annealing Temp. (°C)	Softening Temp. (°C)	Working Temp. (°C)	Strain Point (°C)
2408	Zinc Soda	Cd-Sulfo- Selenade	43	537	765	1083	501

The optical properties of this glass were measured at the Argon laser and HeNe laser wavelengths. For the Argon laser of all line output of a Coherent Radiation model 52G laser the absorption coefficient was measured to be  $67 \text{ cm}^{-1}$ . The refractive index and absorption coefficient of this glass at the  $6328 \text{ Å}$  HeNe wavelength is 1.507 and  $0.3 \text{ cm}^{-1}$  respectively. We have also measured the softening temperature by differential thermal analysis and found that it is between  $760\text{--}790^\circ\text{C}$ . The wafer is polished optically flat, with a thickness of typically 2-3mm, and overall dimension of  $2.5 \times 5 \text{ cm}$ .

#### Laser Heating and Temperature Profile

To produce the channel waveguide, the sample is placed near the focal point of an Argon laser beam using a  $f/2$  or  $f/3$  optical lens, and is mounted on a x-y micropositioning stage driven by stepping motors. By controlling the drive speed and laser power level, channel waveguides of various dimensions were obtained.

The temperature rise due to the laser heating has been calculated following Pittaway's treatment<sup>4</sup>.

The temperature rise  $T(^{\circ}\text{K})$  in a material of thermal conductivity  $K$  (watt/ $\text{cm}^2\text{C/cm}$ ) due to a scanning laser beam of scanning velocity  $v$  (cm/sec)



focused on the surface of a semi-infinite target with a power of  $E_0$  watts, and a Gaussian profile of radius  $d$  cm is given by:

$$T = \frac{E_0}{Kd\pi^{3/2}} \int_0^{\pi/2} \exp\left[\left\{\left(m - \frac{1}{\gamma}\right)^2 + \beta^2\right\} \sin^2\mu - \frac{\tan^2\mu}{\gamma^2} (m^2 - \beta^2)\right] d\mu \quad (1)$$

where  $\beta d$  and  $md$  are the distances measured from the center of the beam, perpendicular and along the scanning direction of the laser beam respectively,  $\gamma = 4\kappa/vd$  and  $\kappa$  is the thermal diffusivity ( $\text{cm}^2/\text{sec}$ ).

For the case where  $v = 0$ , the peak temperature is:

$$T_p = E_0/2Kd\sqrt{\pi} \quad (2)$$

using typical values for glass ( $\kappa = 58 \times 10^{-4} \text{cm}^2/\text{sec}$  and  $K = 1.18 \times 10^{-2} \text{watt/cm}^2\text{C/cm}$ ), for a laser beam of available power at the medium surface of 0.5 watt (value used for our experiments) and radius of  $d = 100\mu\text{m}$ , we have

$$T_p = 0.5/1.18 \times 10^{-4} \cdot 2\sqrt{\pi} \approx 1200^\circ\text{C} \quad (3)$$

This is the expected peak temperature at the center of the laser scanned track. Since the thermal diffusion time for a  $100\mu\text{m}$  radius heated spot is approximately given by

$$t = \frac{d^2}{4K} = \frac{10^{-4}}{4 \times 58 \times 10^{-4}} = 4 \text{ msec.} \quad (4)$$

any scanning velocity slower than



$$v \approx \frac{d}{t} \approx 2\text{cm/sec} \quad (5)$$

can be considered essentially stationary.

Calculation of temperature rise as a function of  $m$  and  $\beta$  under slow scan condition ( $\gamma^{-1} = 0$ ) was performed by numerical integration and the result is shown as a 3-d plot in Figure 1. The normalized temperature at  $\beta=0$  is also plotted as a function of  $m$  in Figure 2. It is seen that the temperature-rise falls to about 50 percent of the peak value at  $m=1$  or at a Gaussian radius from the center of the beam. For the type of glass used, we will have a track of approximately  $100\mu\text{m}$  radius heated above the softening temperature.

#### Surface Deformation and Laser Beam

The technique of laser scanning will be described in detail in a later section. Basically, the optically polished glass wafer is transported across the focal point of an Ar laser beam and a heated track is produced. Since the glass temperature around the center of the track has been heated above the softening temperature as was calculated above, and due to thermal expansion, this heated track is physically raised. Upon subsequent cooling, a permanent raised track results. Figure 3(a) shows a typical profile of such a laser-heating-produced ridge as was measured by a Tallysurf profilrecorder. A scanning electron micrograph of the track is shown in Figure 3(b). Since this track (or ridge) dimension is related to its waveguiding property, we have measured the ridge height  $h$  and width at  $\frac{1}{e}$  point,  $w$ , as a function of the scanning speed and laser output power  $P$ . (The absorbed power is approximately 50 percent of the output power.) The result is shown in Figures 4 and 5. The scanning speed varies from  $4\mu\text{m/sec}$  to  $87\mu\text{m/sec}$  and the Ar laser all line output power varies from 1.04 to 0.83 watt. In this scanning speed region, the temperature rise is expected to be essentially independent of the

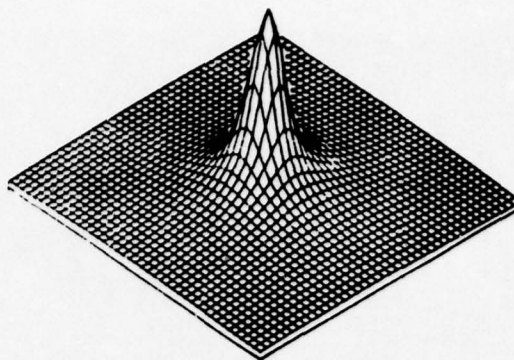


Figure 1. Normalized instantaneous temperature on the glass sample by a slow scanning focus Ar laser beam. The grid spacings are half of the Gaussian beam radius. Scanning direction is pointing towards lower right.

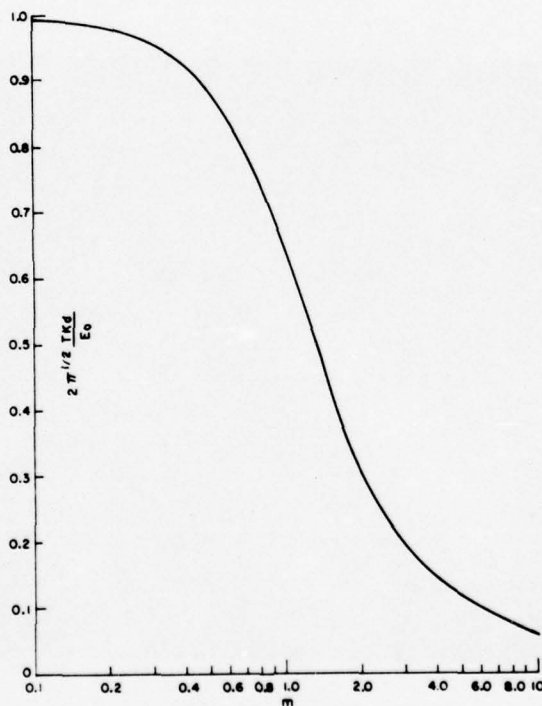
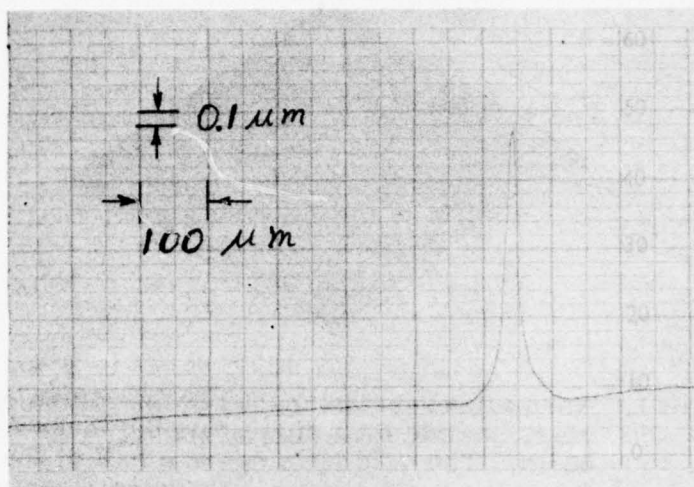
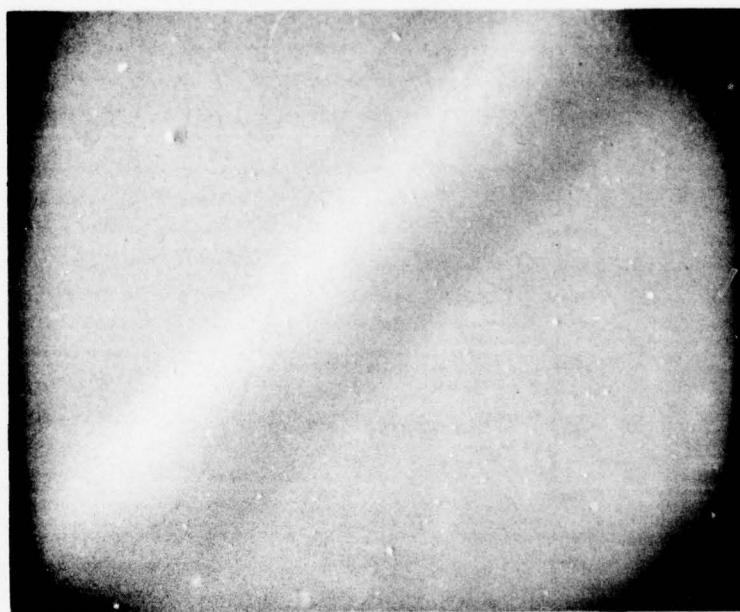


Figure 2. Normalized temperature as a function of the normalized distance along the center of the scanning track.



(a)



(b)

Figure 3. Profile of a laser heated ridge on Corning filter glass CS-2-60: (a) Tallysurf profile, vertical scale  $0.1 \mu m$ /small division, horizontal scale  $100 \mu m$ /major division; (b) scanning electron microscope photograph of the ridge, magnification 500X.

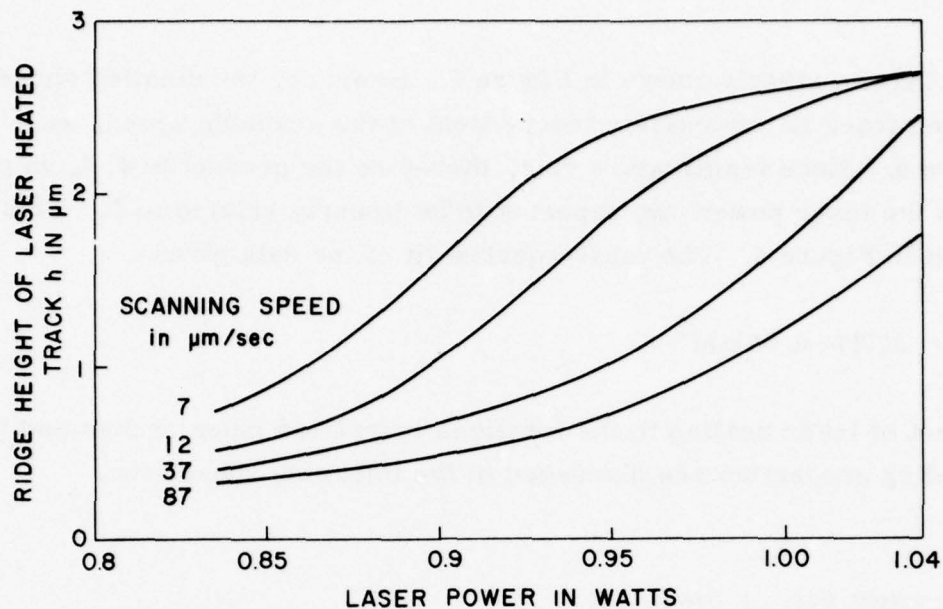


Figure 4. Ridge height  $h$  as a function of the laser output power in watts for various values of scanning speed.

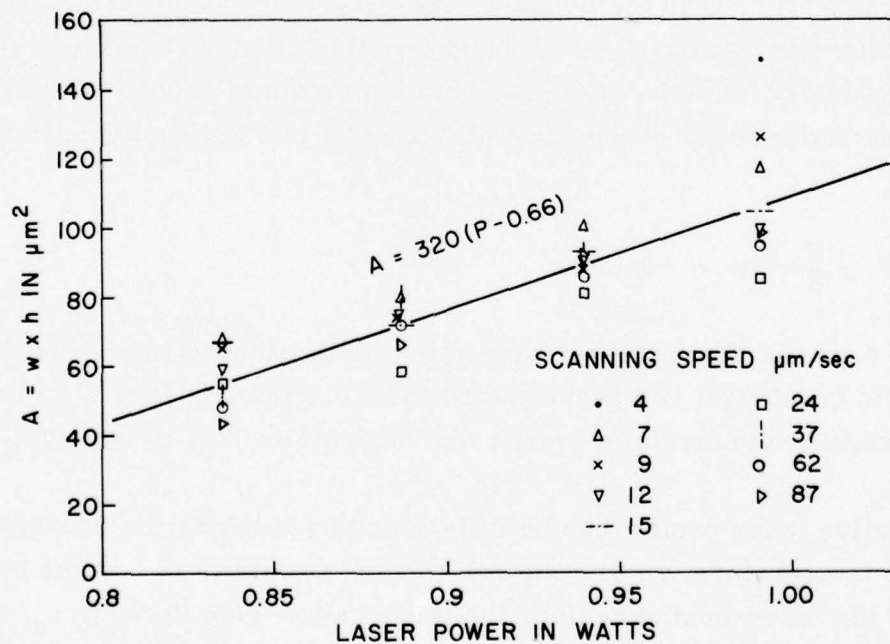


Figure 5. Ridge cross-sectional area parameter  $A = hxw$  as a function of the laser output power in watts for various values of the scanning speed.



speed. This is clearly shown in Figure 5. However, the detailed shape of the heated track is not entirely independent of the scanning speed, as is seen in Figure 4. Since temperature rise, therefore the product  $h \cdot w = A$ , is proportional to the laser power, we expect  $A$  to be linearly related to  $P$ . This is observed in Figure 5. The least-squares fit of the data gives

$$A = 320(P - 0.55) \mu\text{m}^2 \quad (6)$$

The effect of laser heating to the localized refractive index change and the waveguiding properties are discussed in the following subsection.

#### REFRACTIVE INDEX PROFILE

Based on the surface deformation, we can estimate the upper limit of the elastic strains induced in the neighborhood outside the laser-heated region, assuming there is no stress relief during cooling and the change of volume occurs elastically. For  $h = 1 \mu\text{m}$ , we obtain a strain of 0.005. The strain-induced refractive index change  $\Delta n_s$  at this point can in turn be estimated to be

$$\Delta n_s \cong -\frac{1}{2} n^3 p \cong -0.002 \quad (7)$$

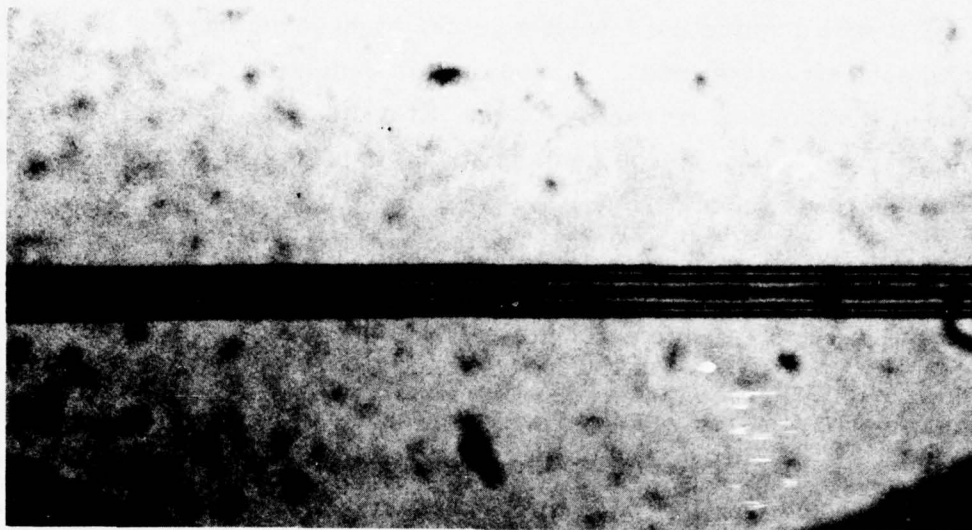
where  $n = 1.507$  is the measured refractive index of the glass.  $p$  is the photoelastic coefficient and is measured to be 0.2 (see Section IV). Outside this region, the strain is tensile and falls off as  $1/r$ , as does  $\Delta n_s$ .

The refractive index profile can be understood by invoking the concept of the fictive temperature,  $\tau$ , and the relation of  $\tau$  to density<sup>5</sup>. In the central portion of the laser-heated region, the temperature rise exceeds  $\tau_0$ , the existing fictive temperature of the glass. The rate of cooling and consequently the fictive temperature is expected to be dependent on the radial coordinate.

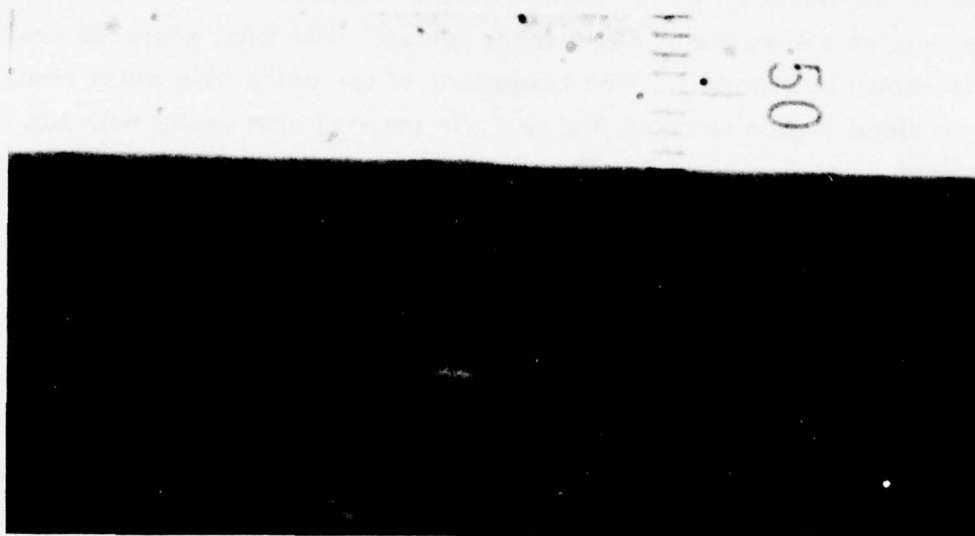
Since the center of the heated region cools at a lower rate than the outer region, it will acquire the lowest  $\tau$  value, highest density and therefore the highest refractive index. Based on this deduction, the cross-sectional profile of the index of refraction of the laser-heating-induced waveguide should take a W shape. The central hump corresponds to the region of higher density resulting from a lower  $\tau$ , and the wings are due to the strain-induced effect.

Experimental measurements of the refractive index profile were obtained using a Jamin-Lebedeff interference microscope. The laser-written track as viewed from the top is shown in Figure 6(a). The glass slab containing a cross section of the laser-heating-induced waveguide was cut and polished optically flat and parallel on both sides to expose the cross section. A photograph of a typical interference pattern of the waveguide cross section is shown in Figure 6(b). The semicylindrical symmetry of the profile is evident here. Careful examination of this interference pattern as the analyzer angle on the microscope is varied reveals that there is a refractive index minimum at a distance of  $80\mu\text{m}$  from center. The final analyzed profile for  $\Delta n$  is shown in Figure 7. The magnitude of the refractive index change in the strained region is about  $3 \times 10^{-3}$ , in general agreement with Eq. (7). The central region has a localized refractive index increase of  $\Delta n \sim 10^{-3}$ . Based on these results, we can estimate the numerical aperture N. A. of the waveguide. Using the analysis for step-index optical fiber<sup>6</sup>,  $\text{N. A.} \approx \sqrt{2n\Delta n}$ , and for  $n = 1.5$ ,  $\Delta n \sim 10^{-3}$ ,  $\text{N. A.} \approx 0.05$ .

The high residual stress could be substantially reduced by a stress-relieve annealing at  $550^\circ\text{C}$  for 1 hour. The resultant refractive index profile in the central core region is essentially unaltered. We have measured the incremental refractive index near the track center for various values of power  $P$ , scanning speed  $v$  and defocusing condition. The results are shown in Figures 8, 9, and 10. These profiles were measured along a 45-degree line



(a)



(b)

Figure 6. Interference microscope photograph of the LHSI track: (a) top view where the fringes are mainly due to the raised ridge; (b) cross-sectional view which exposes the refractive index profile.

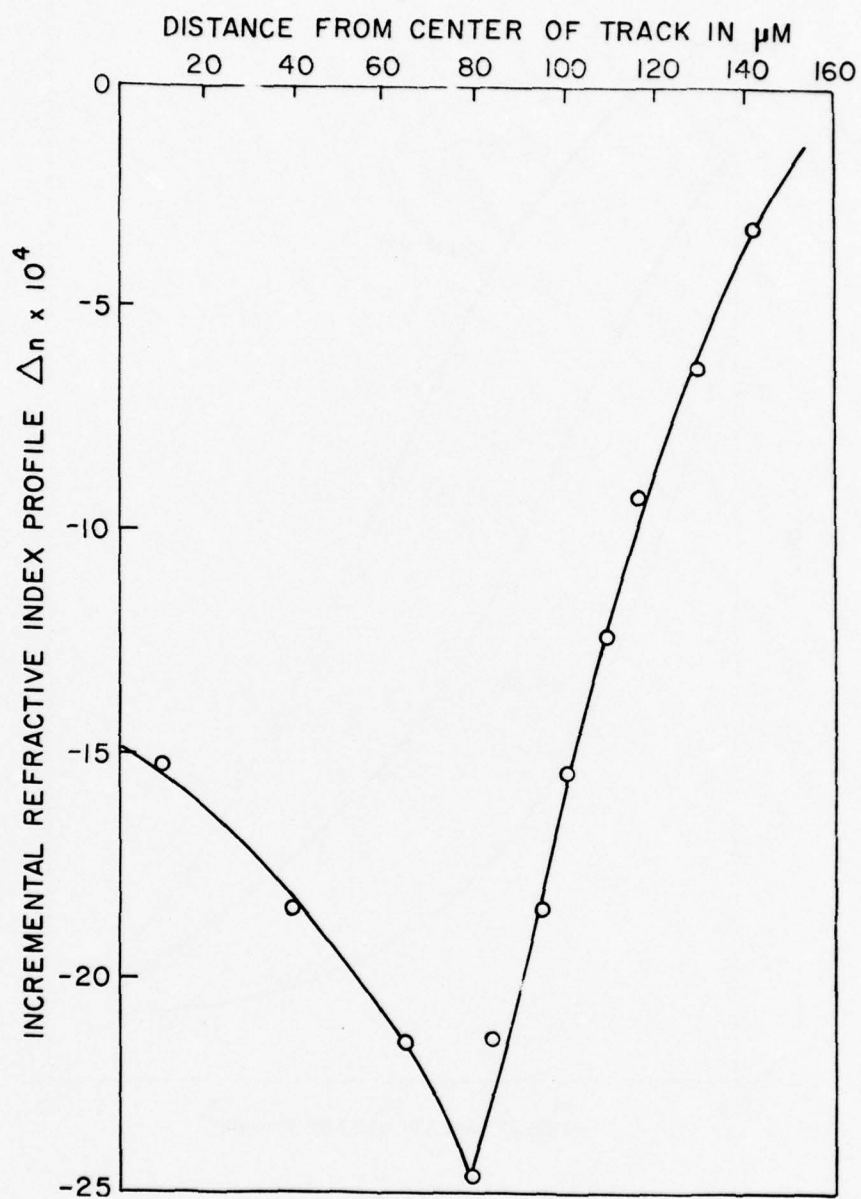


Figure 7. Refractive index profile of a typical LHSI waveguide.



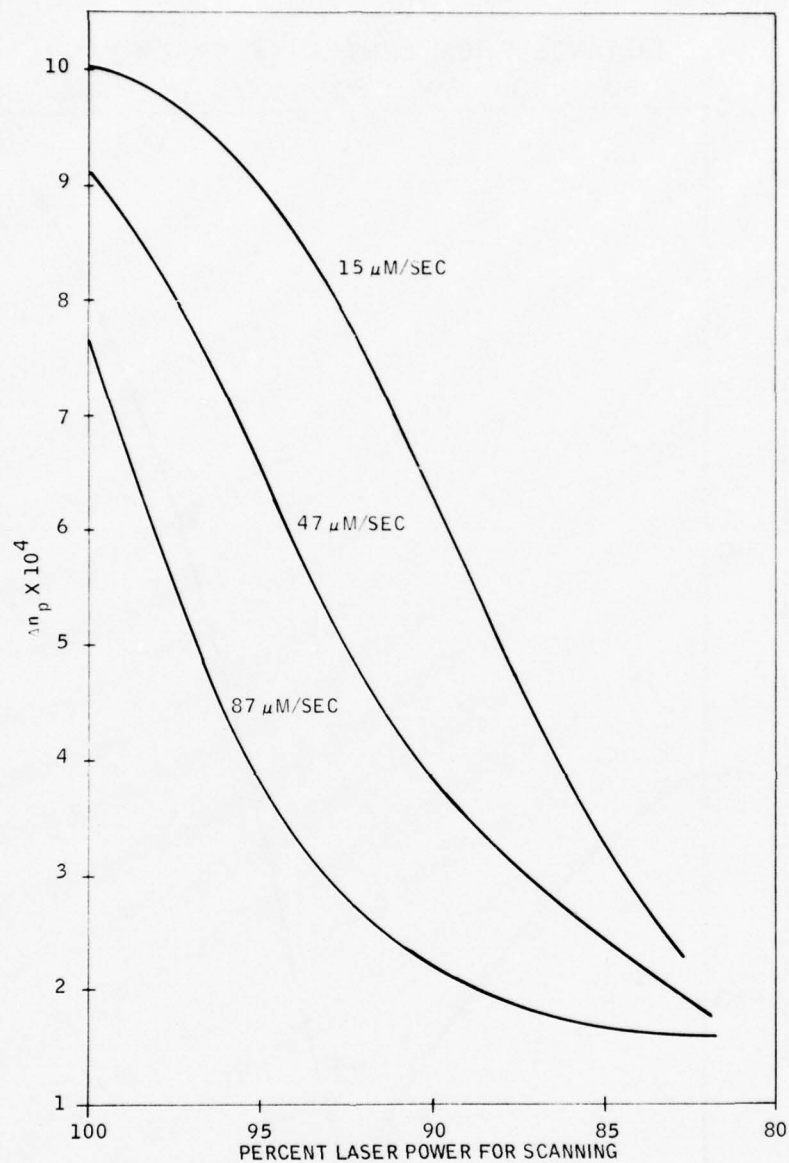


Figure 8. Dependence of the peak value of the refractive index  $\Delta n_p$  as a function of the percent laser power output used for scanning, for three different scanning speeds (100% = 1.04 watts).

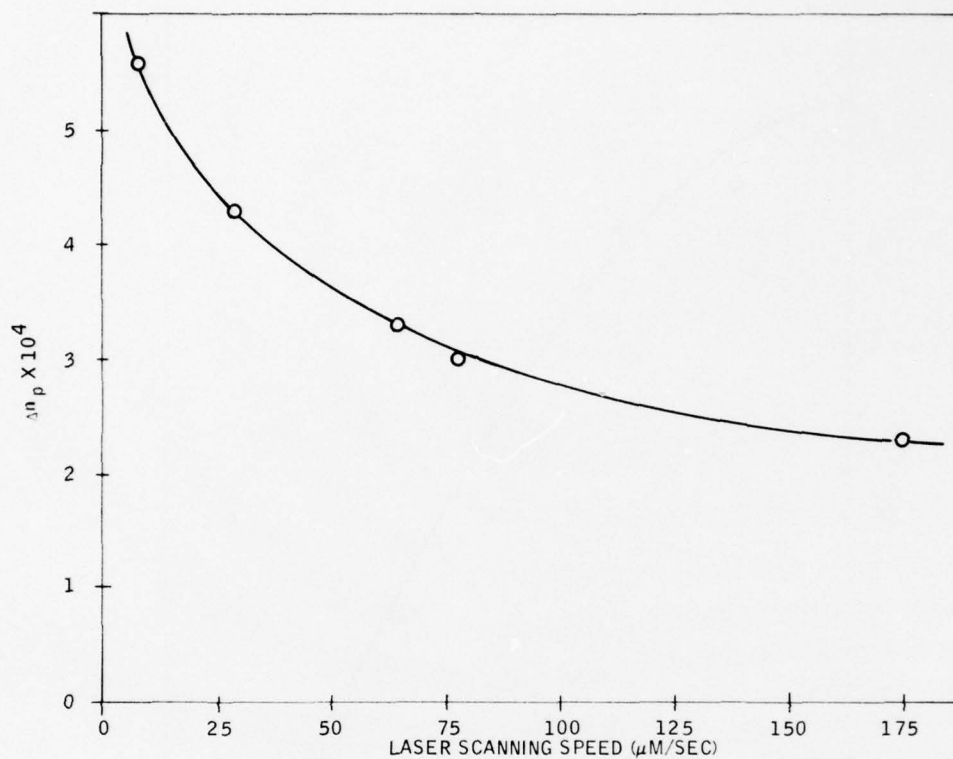


Figure 9. Dependence of the peak value of the refractive index as a function of the scanning speed at 92% of laser power used.

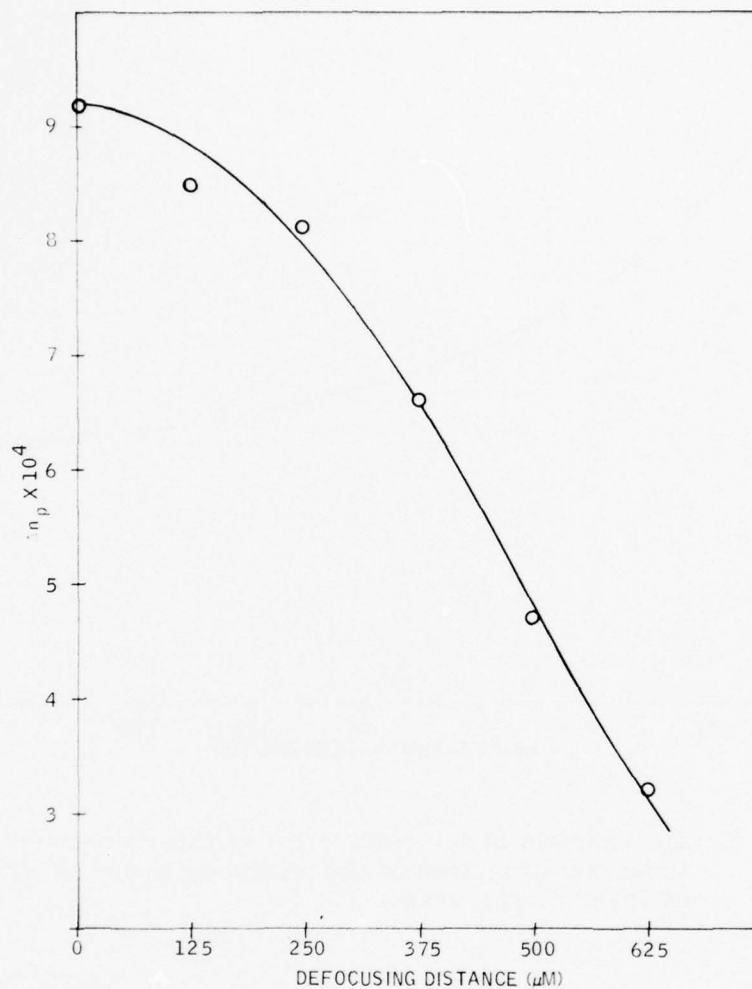


Figure 10. Dependence of the peak value of the refractive index as a function of the defocussing distance (distance between sample surface to the laser focal point). Data obtained for 100% laser power at 47μm/sec scanning speed.

from the center of each track. It is seen that by proper choice of P, v and defocusing condition, the peak value of  $\Delta n$  can be controlled. The profile for all the scanning speed, power and defocusing condition are approximately parabolic. The waveguide mode analysis to follow will therefore use a parabolic profile approximation.

## RESIDUAL STRESSES IN LHSI WAVEGUIDES

In this subsection the residual stresses introduced into the glass by laser heating are discussed. As was discussed earlier, the stresses are substantial and, under some conditions, can cause an intriguing form of fracture. It should be noted that the residual stresses cause a reduction of the refractive index and acted to trap the guided wave which propagates in the softened region. The residual stresses can be substantially removed by a stress relief anneal, the laser heated region still acts as a waveguide and the material is no longer susceptible to fracture. All LHSI waveguides and devices used for waveguiding measurements reported here were annealed and are stable and fracture free.

The residual stresses can be estimated from the refractive index profile shown in Figure 7. The change in refractive index is given by Eq. (7). From this we can derive

$$\sigma = - \frac{2E\Delta n}{n^3 p s} \quad (8)$$

where E is Young's modulus. Residual radial stresses calculated from the index measurements made on the 80 $\mu$ m radius laser heated track shown in Figure 7 are shown in Figure 11. For these calculations the values of the constants were assumed to be  $E = 9.9 \times 10^6$  psi,  $n = 1.5$  and  $p \approx 0.5$ . The stresses are plotted as a function of the distance from the outside of the

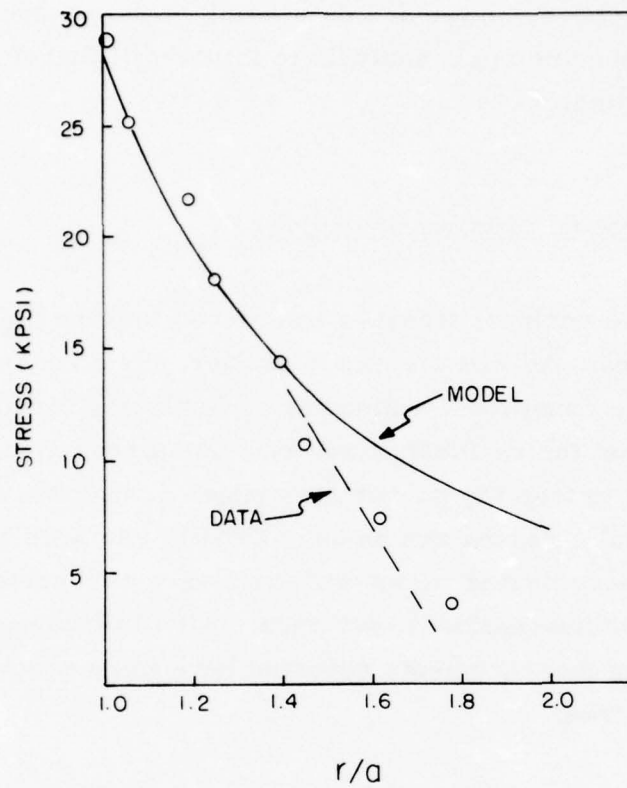


Figure 11. Residual stress  $\sigma$  as a function of the normalized radius distance  $r/a$  from the center of the LHSI track.



heated zone normalized by  $a$ , the radius of the heated zone. Note that the radial stress field is tensile and decreases approximately linearly with distance from the heated region.

These stresses can be estimated with the aid of the following simple model<sup>7</sup>. Assume that a cylindrical region of radius  $a$ , in the glass is suddenly heated to above the softening point,  $\tau_o$  (the fictive temperature). Above  $\tau_o$  the cylindrical region is stress-free. As the region cools through  $\tau_o$  it becomes an elastic solid and starts exerting a radial tensile stress on the surrounding material as it shrinks. The radial tensile stress field resulting from the cylinder cooling to room temperature is given by

$$\sigma_r = \frac{-\alpha E \Delta T}{2(1-\nu)} \left(\frac{a}{r}\right)^2 \quad (9)$$

where  $\alpha$  is the coefficient of thermal expansion,  $\nu$  is Poisson's ratio and  $r$  is the radial distance from the axis of the cylinder;  $E = 9.9 \times 10^6$  psi,  $\nu = .2$ , and  $\alpha$  is assumed to be  $6 \times 10^{-6} \text{ } ^\circ\text{C}^{-1}$ . The radial stresses calculated from the simple shrink fit model are shown in the solid line on Figure 11. The model does not predict the observed linear dependence of  $\sigma_r$  with  $r$  but the values of stress are of the right order. It should be pointed out, however, that the data on both the Young's modulus,  $E$ , and the thermal expansion coefficient,  $\alpha$  are estimated, since values measured at room temperature are not expected to be valid. For this reason the magnitude of stress plotted on Figure 11 should only be considered as approximate.

In the above discussion we have only considered the stresses in the material outside the heated region. The stresses inside the heated region cannot be determined from interference microscope measurements such as those shown in Figure 7 because heating above the softening point has also altered the density. In this case the index of refraction is a function of both the density and the residual stress. The two cannot be separated.

When an unannealed waveguide comes into contact with a foreign object (e. g. , a coupling prism), it sometimes fractures in a most unusual manner. A crack forms at the point of contact, usually at the edge of the glass where the waveguide terminates, and runs along one side of the guide parallel to it. After propagation has continued for some distance the crack turns and runs through the guide at right angles to it until it reaches the opposite side. At this point the crack momentarily stops and then starts moving again parallel to the guide as before but now on the opposite side. After running approximately the same distance as before the crack turns and runs across the guide and stops. At this point the process repeats itself. A top view of this fracture process is shown in Figure 12. The crack itself is cylindrical, as expected from the radial tensile stress field shown in the interference measurements. A scanning electron micrograph of the end view of the crack is shown in Figure 13. The ridge running down the surface of the glass is the top of the region heated above the softening point by the moving argon laser beam. The crack runs at quite a slow rate and it takes many minutes to traverse the whole length of the guide. Thus, the fracture is subcritical and occurs most likely by a stress corrosion mechanism.

In what follows, a phenomenological model describing the fracture is presented. Quantitative discussion must be postponed till further analysis is made. As we have seen, the waveguide is a semicylindrical region at the glass surface that was heated above the glass transition temperature by a moving argon laser beam. The softened region is rapidly quenched following passage of the laser. The quenched region has a lower density than the bulk glass as is evident from the ridge seen in Figure 13. Heat flow during cooling is predominantly into the glass and the resulting residual stress field has radial symmetry about the axis of the guide.

The principal stresses in this case are  $\sigma_r$ , a radial tensile stress,  $\sigma_\theta$ , a compressive tangential stress, and  $\sigma_z$  a tensile stress lying along the axis of the guide. The principal stresses are shown on Figure 14 which is a

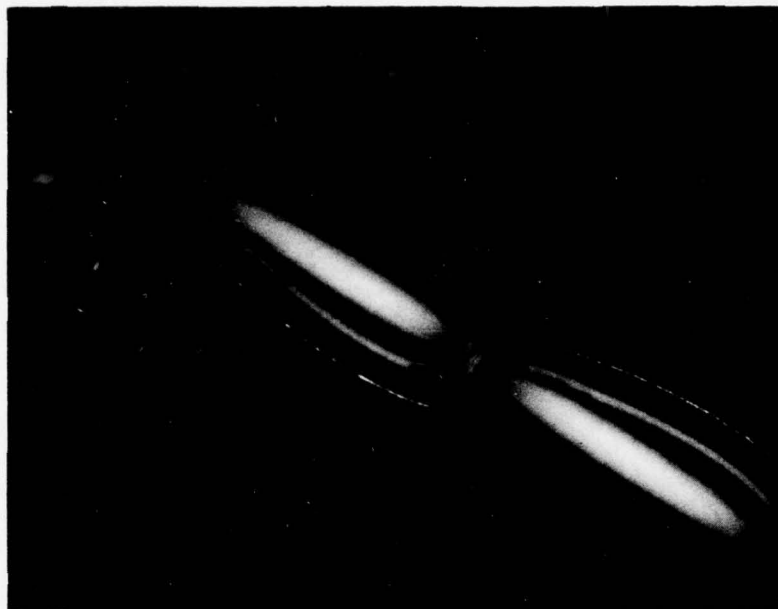


Figure 12. Photograph of fracture around an unannealed LHSI track.

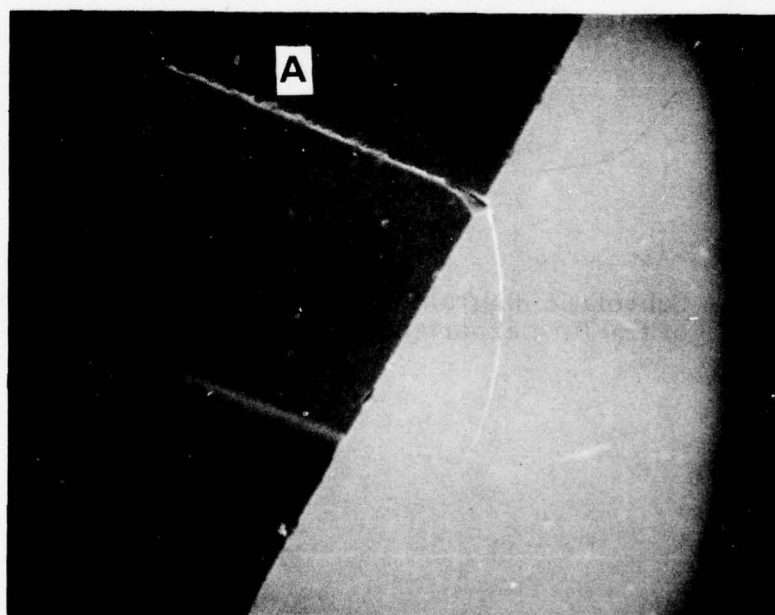


Figure 13. Scanning electron micrograph of the end view of a crack of an annealed LHSI track.



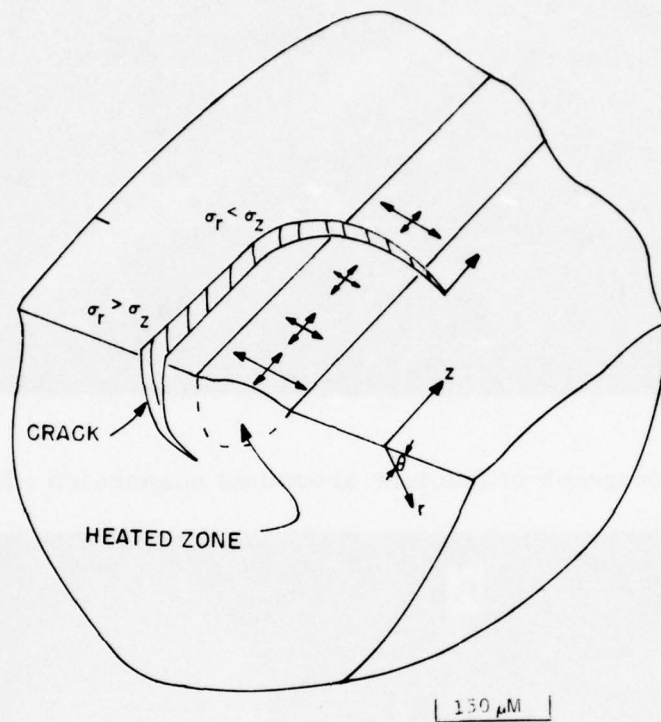


Figure 14. Schematic diagram of residual stresses showing model of fracture experienced by the unannealed LHSI waveguide.

schematic of the proposed fracture model. The magnitudes of the principal tensile stresses,  $\sigma_r$  and  $\sigma_z$  depend on the quenching rate. Glass is a visco-elastic material and can undergo stress relaxation during cooling.  $\sigma_r$  depends on heat flow along the guide in the  $z$  direction which in turn depends on the rate of traverse of the laser beam. We presume that  $\sigma_r > \sigma_z$  as indicated on the figure. The initial crack will be perpendicular to  $\sigma_r$  and will run parallel to the guide in the  $z$ -direction.  $\sigma_r$  is a residual stress and is relieved as the crack propagates. Since the crack will follow the direction of maximum tensile stress it will turn across the guide as the ratio  $\sigma_r/\sigma_z$  decreases. When the crack runs across the guide  $\sigma_z$  is relieved and the crack halts. We have observed that the crack bifurcates (i. e., branches) as it stops. One of the branches is in a favorable orientation with respect to  $\sigma_r$  in the uncracked region and the process repeats itself.

A number of questions concerning the model remain to be answered. First, as mentioned above, due to uncertainties in the Young's modulus and in the thermal expansion coefficient, the stresses in the region outside the heated zone where the crack is running are not known with much certainty. Another estimate of the radial stress can be obtained from the separation at the crack (i. e., at point A in Figure 13). The separation was measured by scanning electron microscopy to be about  $1\mu$  for the crack running  $235\mu\text{m}$  outside of the center of the guide. This corresponds to a surface radial strain of  $2.1 \times 10^{-3}$ . The residual stress corresponding to this strain is 21000 psi which is on the order of the stresses shown in Figure 11.

While the magnitude of the residual stress is reasonable the position of the crack is not. The maximum radial tensile stress is at the interface between the heated zone and the surrounding material. The observed fractures occur at a considerably distance from the heated zone as obvious from Figure 13. Typically the distance of the crack to the waveguide is an order of magnitude larger than the radial dimensions of the guide. At this distance from the guide the stress birefringence shown in Figure 7 is small indicating a low

stress level. At this time we do not understand why the guides crack where they do.

Alternate models of the residual stress in the glass following passage of the laser beam have been suggested which more realistically treat the glass as a viscoelastic material<sup>8</sup>. More analysis and experimentation are needed to achieve a better understanding of this crack mechanism. It should be emphasized here that in all the optical waveguiding experiments, the LHSI waveguides are all preannealed and stresses are substantially removed. No crack was observed in the annealed samples.

## LHSI WAVEGUIDE PROPERTIES

### Waveguide Mode Theory for LHSI Guides

The LHSI guides described above may be conveniently modeled as having an index profile with semicircular symmetry. That is, there is a line of symmetry on the surface of the guide material with the index of the guide a function only of distance from this line inside the material. In this section we present a simple analysis of the modes of multimode graded-index fibers (circular symmetry) and semicircular graded-index guides. Normalized parameters are defined so that a single equation or a single universal chart describes all such guides having a particular index profile shape, such as parabolic, Gaussian, etc. The initial steps in the problem description come from Reference 6. We first consider circularly symmetric graded-index fibers and will later explain the modifications necessary for a description of semicircular guides.

We assume that the fiber waveguide is circularly symmetric with a small index change in the core region, and that index variations on the scale of a wavelength are small. The index profile is a continuous function of radial

position,  $n(r)$ . At any radial position  $r$  the wave vector has the magnitude  $k(r) = 2\pi n(r)/\lambda = k_0 n(r)$ .

The modes of this waveguide are described by two integer mode numbers,  $v$  and  $u$ . The azimuthal mode number,  $v$  describes the number of cycles of the electric field in the azimuthal direction. At position  $r$  the azimuthal component of the wave vector is therefore  $v/r$  ( $= 0, 1, \dots$ ) in order that the phase go through  $v$  cycles around the circumference  $2\pi r$ ; e. g., the variation of amplitude with azimuthal angle  $\theta$  is either  $\sin(v\theta/r)$  or  $\cos(v\theta/r)$ . If a mode exists which propagates down the fiber with wave vector  $\beta$ , then by a geometrical construction the radial component of the wave vector at radial position  $r$  is

$$u(r) = [k^2(r) - \frac{v^2}{r^2} - \beta^2]^{1/2} \quad (10)$$

Only between two radial positions  $R_1$  and  $R_2$  is  $u(r)$  real and the radial phase variation periodic.  $u(R_1) = u(R_2) = 0$  and  $R_1 < R_2$ . Outside this region the field is aperiodic. The wave can be through to undergo reflections from the graded index profile at  $R_1$  and  $R_2$ . Such a reflection introduces a phase shift<sup>9</sup> of  $\pi/4$ . The total radial phase change between  $R_1$  and  $R_2$ , including these phase shifts, must add up to an integer multiple of  $\pi$  for a mode to exist, leading to the mode dispersion equation

$$\int_{R_1}^{R_2} [k^2(r) - \frac{v^2}{r^2} - \beta^2]^{1/2} dr = (\mu + \frac{1}{2})\pi \quad (\mu = 0, 1, 2, \dots) \quad (11)$$

A similar mode dispersion equation applies for diffused planar guides<sup>9</sup>.



Let the index profile be written as

$$n(r)^2 = n_b^2 + (n_a^2 - n_b^2)f(r/R_o) \quad (12)$$

where  $n_a$  is the index at the center of the fiber,  $n_b$  is the constant index away from the graded core, and  $f(r/R_o)$  is the normalized shape of the index profile.  $f(0) = 1$  and  $f(r/R_o)$  declines monotonically to zero with increasing  $r$ . For example, a parabolic index fiber would have  $f(u) = 1 - u^2$  for  $0 \leq u \leq 1$ .  $R_o$  is the scale factor for the index shape.

Two normalized parameters can be defined: The normalized guide radius  $V$ , and the normalized mode effective index  $b$

$$V = k_o R_o [n_a^2 - n_b^2]^{1/2} \quad (13)$$

$$b = \frac{n_{\text{eff}}^2 - n_b^2}{n_a^2 - n_b^2} \quad (14)$$

where the effective index of a waveguide mode is  $n_{\text{eff}} = \beta/k_o$ . Similar normalized parameters can be used to define thin film and diffused planar waveguides<sup>9,10</sup>.

The mode dispersion Eq. (11) can now be written in normalized form as

$$\int_{U_1}^{U_2} \left[ V^2 f(u) - V^2 b - \frac{v^2}{u^2} \right]^{1/2} du = (\mu + 1/2)\pi \quad (15)$$

where we have made the substitution  $u = r/R_o$ , and the limits  $U_1$  and  $U_2$  are where the integrand equals zero, with  $U_1 < U_2$ . For a given profile shape  $f(u)$ , this normalized mode dispersion Eq. (15) describes the modes of all fibers

having such a shape in terms of the normalized parameters  $b$  and  $V$ . Equivalently, for each shape  $f(u)$  a universal chart of  $b$  versus  $V$  can be plotted from Eq. (15) which describes the modes of all waveguides having this index shape.

The total number of modes in a graded-index fiber is shown in Reference 6 to be

$$M = \left(\frac{2\pi}{\lambda}\right)^2 \int_0^a [n(r)^2 - n_b^2] r dr \quad (16)$$

where  $a$  is where  $n(r)$  reaches the cladding index  $n_b$ , and  $M$  includes both a two-fold degeneracy in polarization and a two-fold degeneracy in azimuthal orientation. Changing variables to  $u = r/R_0$  and substituting Eqs. (12) and (13) gives

$$M = V^2 \int_0^{\infty} f(u) u du \quad (17)$$

Many of the index profiles for LHSI guides can be approximated as parabolic. We now show how a parabolic index profile leads to an extremely simple form for the mode dispersion equation.

For a parabolic index fiber, the shape function  $f(u)$  is

$$f(u) = \begin{cases} 1 - u^2 & \text{for } 0 \leq u \leq 1 \\ 0 & \text{for } u \geq 1 \end{cases} \quad (18)$$

Substituting this into the mode dispersion Eq. (15), that equation can then be integrated. The mode dispersion equation for a parabolic index fiber becomes

$$V(1 - b) = 2(2\mu + \nu + 1) = 2m \quad (m = 1, 2, \dots) \quad (19)$$

where all modes with indices  $\mu$  and  $\nu$  giving the same value of  $m = 2\mu + \nu + 1$  are degenerate. This equation can be shown to be equivalent to the unnormalized mode dispersion equation derived in Reference 11 for parabolic index fibers. A universal chart of  $b$  versus  $V$  describing the modes of all parabolic index fibers can easily be plotted and is shown as Figure 15.

For a parabolic index fiber the total number of modes  $M$  can be written in normalized form using (17) as:

$$M = \frac{1}{4} V^2 \quad (20)$$

$M$  includes both the two-fold degeneracy in polarization ( $x$  or  $y$ ) and the two-fold degeneracy in orientation (azimuthal variation of  $\sin(\nu\theta/r)$  or  $\cos(\nu\theta/r)$ ).

The above results may be used to describe parabolic index profile fibers. These fibers are of great importance because of the small variations in group velocity for the various modes, leading to a narrow impulse response and the capability for transmitting information at high data rates.

To apply the results given by Eq. (15) and (17) for the general graded-index fiber to the semicircular model of LHSI guides, we note that a semicircular guide is one which looks like half of a circularly symmetric fiber which has been sliced along its axis. Denoting the plane of this cut as  $y = 0$  and assuming the guide is bounded above by air, the index profile in rectangular coordinates is:

$$n(x, y)^2 = \begin{cases} n_b^2 + (n_a^2 - n_b^2) f((x^2 + y^2)/D^2) & \text{for } y > 0 \\ 1 & \text{for } y < 0 \end{cases} \quad (21)$$

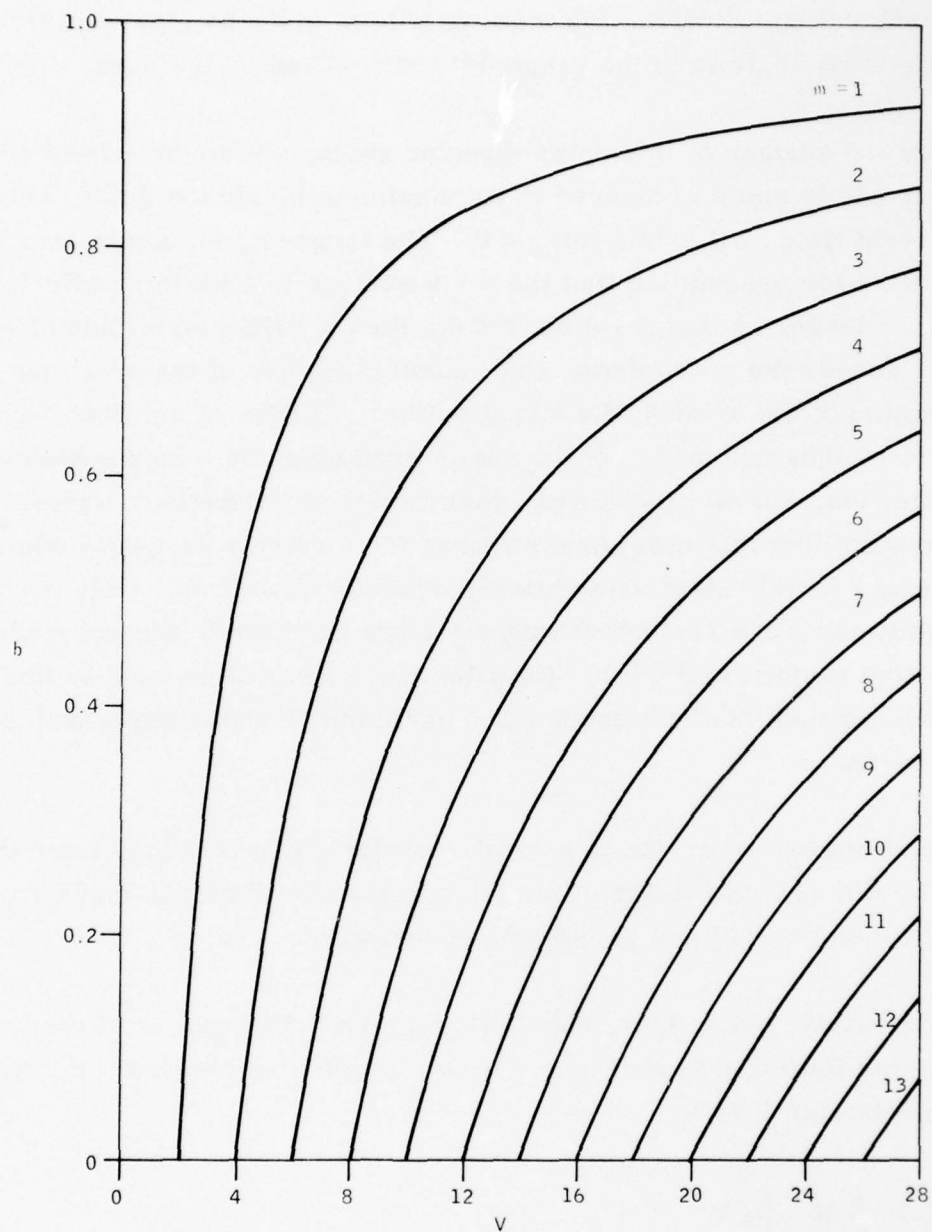


Figure 15. The normalized mode effective index  $b$  as a function of the normalized guide radius  $V$  for various mode number  $m$ , calculated for parabolic index fibers.



In cylindrical coordinates, the index profile is given by (12) and (21) when the azimuthal angle is in the range  $0 < \theta < \pi$ . Outside the range of  $\theta$ ,  $n(r) = 1$ .

At the  $y = 0$  surface of this semi-circular guide, the electric field amplitude of any mode is small compared to its maximum inside the guide, but a weak evanescent field still exists for  $y < 0$ . The larger  $n_s$  is, the weaker this field. If we make the assumption that the  $y = 0$  surface is a perfect reflector (or that  $n_s$  is large, or that  $n = 0$  for  $y < 0$ ), then the field amplitude of each mode is zero across the  $y = 0$  plane, and we can make use of the previous description of the modes of a circular fiber. Modes of the fiber having a null along  $y = 0$  thus are modes of the semi-circular guide. Modes with  $\nu = 0$  are ruled out, but all modes with other values of  $\nu$  have null planes. The requirement that this null plane be along  $y = 0$  merely serves to remove the degeneracy in azimuthal orientation previously described. Only modes with azimuthally variation  $\sin(\nu \theta/r)$  with  $\nu \geq 1$  are permitted, and not modes with  $\cos(\nu \theta/r)$  variation or  $\nu = 0$ . Equation (15) may still be used to find the allowed combinations of  $b$  and  $V$  for a particular  $f(u)$  and mode indices  $\nu \geq 1, \mu \geq 0$ .

The total number of modes in a semi-circular guide is halved from that given by Eq. (12) due to the elimination of the orientational degeneracy, and is further reduced by not permitting modes with  $\nu = 0$ .

For a parabolic index fiber, Eq. (20) gives the total number of modes, including the four-fold degeneracy. A number of possible pairs of  $\mu$  and for a particular  $V$  is

$$N = \frac{1}{4} M = \frac{1}{16} V^2 \quad (22)$$

For a semi-circular guide, we subtract the number of pairs with  $\nu = 0$ . For each value of  $m$  there is one such pair, so the number of pairs eliminated equals the maximum value at  $m$  which is  $V$ . Multiplying by the two-fold

degeneracy in polarization, we obtain the total number of modes for a parabolic semi-circular guide as

$$M = \frac{1}{8} V^2 - 2V \quad (23)$$

For a typical LHSI guide,  $R_o = 80\mu\text{m}$ ,  $n_b = 1.51$ , and  $(n_a - n_b) = 1.0 \times 10^{-3}$ , so  $V \approx 44$  for operation at  $\lambda_o = 6328\text{\AA}$ . This leads to a total number of modes  $M \approx 151$ .

#### Losses Due to Index Reversal in LHSI Guides

The LHSI optical waveguides have a higher-index central region with the index decreasing with distance from the axis of symmetry. However, outside a certain radius the index profile reverses and begins to increase, reaching a value in the bulk material which is often higher than in the central guiding region. Energy in the waveguide would be expected to tunnel through the low index region and leak into the higher-index bulk material. We present here calculations which show that the losses due to this leakage should be very small for the LHSI guides.

We again model the guides as having semi-circular symmetry and a parabolic profile, so that we can adapt results obtained for parabolic-index fibers. Marcuse<sup>11</sup> shows that a parabolic-index fiber defined by:

$$n(r)^2 = n_o^2 (1 - 2\Delta r^2/a^2) \quad (24)$$

has modes with transverse electric field amplitudes in Cartesian coordinates of

$$E_{mn}(x, y) = AH_m(\sqrt{2}x/W)H_n(\sqrt{2}y/W)\exp\left[-(x^2 + y^2)/W^2\right] \quad (25)$$

where  $m$  and  $n$  are the mode indices,  $A$  is a constant,  $H_i$  denotes a Hermite polynomial, and  $W$  can be considered the mode radius given by

$$W = (2/\Delta)^{1/4} (a/n_o k)^{1/2} \quad (26)$$

These modes have the same form as the modes of a laser resonator, except that in the latter case  $W$  is a function of axial position as well. The electric fields of the modes can also be written in cylindrical coordinates as<sup>13</sup>:

$$E_{pq} = E_o (\sqrt{2}r/W)^q \underset{p}{L}^q (2r^2/W^2) \exp(-r^2/W^2) [(\frac{\sin}{\cos})^q q\phi] \quad (27)$$

where  $p$  and  $q$  are the radial and azimuthal mode indices, respectively,  $E_o$  is a constant, and  $\underset{p}{L}^q$  is the generalized Laguerre polynomial.

Using the typical LHSI profile of Figure 7, we find it is approximately parabolic, and with  $n_o = 1.51$  we calculate that  $W \approx 17\mu\text{m}$ . Thus the fields at the index reversal radius of about  $R_o = 80\mu\text{m}$  are expected to be small and the leakage into the higher-index bulk material should be very slow.

We can make an approximate calculation of this loss rate by modifying the theory of Marcatili and Miller<sup>14</sup>, used to calculate the radiation loss from curved guides. They approximate the attenuation coefficient  $\alpha$  as:

$$\alpha = \frac{1}{2Z_c} \frac{\epsilon_1}{\epsilon_T} \quad (28)$$

where  $2Z_c$  is the colimated-beam length associated with the transverse field distribution, i. e., it is the length in which the beam radius would double due to diffraction in material of index  $n_o$ . For the case considered here

$$2Z_c \approx n_o (2W)^2 / \lambda \quad (29)$$

and for the profile of Figure 7,  $2Z_c \cong 2.8\text{mm}$ . The ratio  $\epsilon_1/\epsilon_T$  is the fraction of the mode energy in the region where loss occurs. For loss due to index reversal, we can consider all energy is lost for  $r > R_0$ .  $\epsilon_1/\epsilon_T$  are then given by:

$$\epsilon_1 = \int_{R_0}^{\infty} r dr \int_0^{2\pi} E(r, \phi)^2 d\phi \quad (30)$$

$$\epsilon_T = \int_0^{\infty} r dr \int_0^{2\pi} E(r, \phi)^2 d\phi \quad (31)$$

where  $E(r, \phi)$  is given by Eq. (27).

By approximating the Laguerre polynomial in Eq. (27) for large values of  $x/W$  and/or small values of  $q$ , we find that approximately:

$$\frac{\epsilon_1}{\epsilon_T} \cong e^{-u_0} \sum_{i=0}^m \frac{u_0^{m-i}}{(m-i)!} \quad (32)$$

where  $u_0 = 2R_0^2/W^2$  and  $m = 2p+q$ .

We have calculated  $\alpha$  from Eq. (32) using  $W = 17\mu\text{m}$ ,  $n_0 = 1.51$ ,  $\lambda = 0.6328\mu\text{m}$ , and  $R_0 = 80\mu\text{m}$  as in Figure 7. The results are shown in Table 1 for values of  $m$  from 0 to 28. While these calculations are very approximate, they do show that the loss rate should be very low for most waveguide modes. This is expected for the small value of  $W$  compared to  $R_0$ .



Table 1. Approximate Values of Loss Coefficient  $\alpha$  for Various Mode Indices [ $m = 2p+1$  due to index reversal in the guide of Figure 7 using Eq. (32)].

<u><math>m = 2p+1</math></u>	<u>Approximate <math>\alpha</math></u>
0	$6 \times 10^{-20} \text{ cm}^{-1}$
2	$6 \times 10^{-17}$
4	$1 \times 10^{-14}$
6	$7 \times 10^{-13}$
8	$3 \times 10^{-11}$
10	$6 \times 10^{-10}$
12	$9 \times 10^{-9}$
14	$1 \times 10^{-7}$
16	$9 \times 10^{-7}$
18	$6 \times 10^{-6}$
20	$4 \times 10^{-5}$
22	$2 \times 10^{-4}$
24	$6 \times 10^{-4}$
26	$2 \times 10^{-3}$
28	$6 \times 10^{-3}$

#### Properties of LHSI Waveguide

The waveguiding properties of the LHSI glass waveguide has been measured using a glass prism coupler with a base angle  $\theta_p = 45^\circ$  and a refractive index of  $n_p = 1.8$ . The parameters measured are the waveguide acceptance angle and the waveguide losses.

The effective index of refraction of the waveguide  $n_{\text{eff}}$  is related to the prism input coupling angle  $\theta_1$  by the Snell's law.

$$n_{\text{eff}} = n_p \sin(\theta_p + \theta_2) \quad (33)$$

where  $n_p \sin \theta_2 = \sin \theta_1$

From this, we have

$$\frac{dn_{\text{eff}}}{d\theta_1} = \frac{\cos \theta_1}{\cos \theta_2} \cos(\theta_p + \theta_2) \quad (34)$$

For  $\theta_p = 45^\circ$ ,  $n_p = 1.8$  and in the region where  $\theta_1 = 22^\circ$ , we have

$$\frac{dn_{\text{eff}}}{d\theta_1} = 0.516 \quad (35)$$

The measurement of the acceptance angle is indirectly obtained by plotting the laser beam intensity from an output prism as the incident angle  $\theta_1$  is varied. The result for both the TE and TM modes is shown in Figure 16.

The acceptance angle at half intensity point for both cases is 8 minutes or 0.0023 radian. Therefore

$$\Delta n_{\text{eff}} = 0.0023 \cdot 0.516 = 0.0012 \quad (36)$$

Using the relation of numerical aperture N. A. for optical fiber<sup>16</sup> with a step index  $\Delta n$  of core index  $n$ ,

$$\text{N. A.} = \sqrt{2n\Delta n} \quad (37)$$

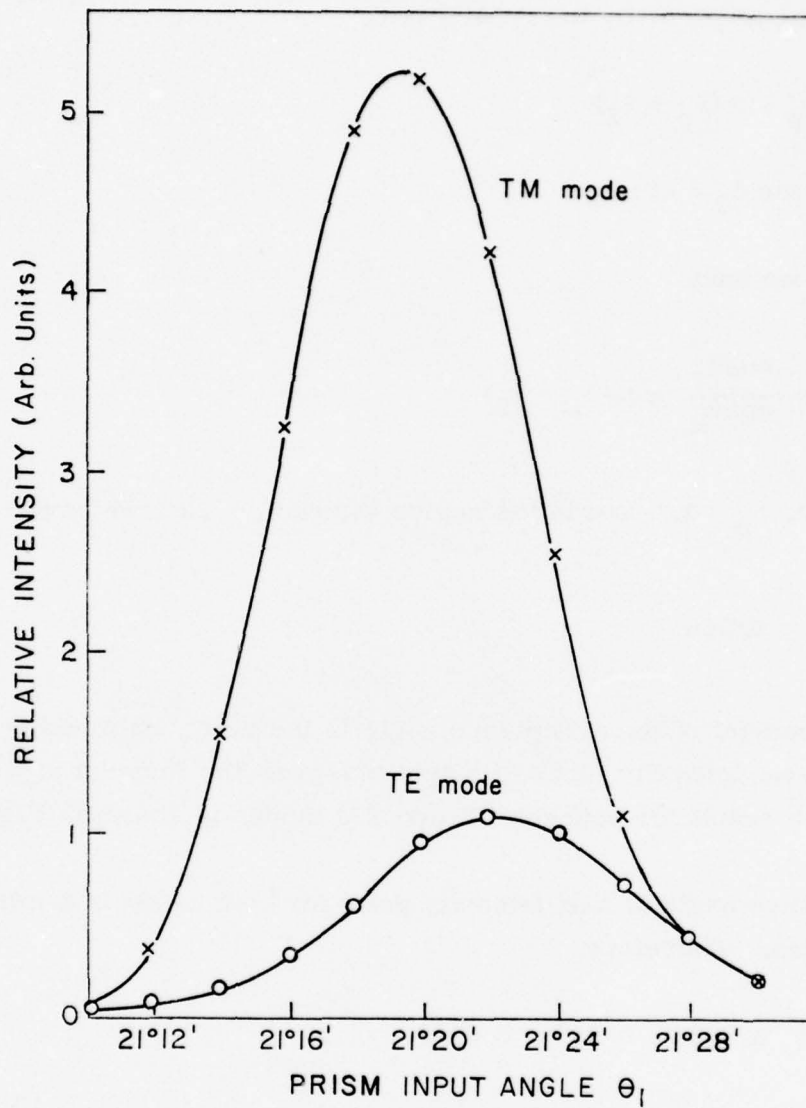


Figure 16. Relative beam intensity at a fixed point in the LHSI waveguide as a function of the incident angle  $\theta_1$  to a 45-degree glass prism ( $n = 1.8$ ) coupler for both TM and TE modes.

we can estimate the N. A. of the LHSI waveguide. We obtain

$$\text{N. A.} = \sqrt{2 \cdot 1.5 \cdot 1.2 \times 10^{-3}} = 0.06 \quad (38)$$

The  $\Delta n_{\text{eff}}$  values calculated from the acceptance angle is in agreement with the  $\Delta n$  value observed from the interference microscope measurement of  $10^{-3}$ .

It is important to note that the LHSI waveguide should be relatively easy to couple to typical multimode optical fiber which possess a N. A. value of 0.1-0.2 and a fiber diameter comparable to the LHSI waveguide dimension.

The attenuation of the LHSI waveguide was also measured using a sliding output prism coupler. The measured relative beam intensity as a function of waveguide length for both the TE and TM waves is shown in Figure 17. The data were least-squares fitted with an exponential curve and the result is also shown in the same figure. From these curves, we obtain the optical losses as follows:

Optical losses for TM waves = 1.66db/cm

Optical losses for TE waves = 3.1db/cm

These results as well as the LHSI refractive index profile has been reported in a recent publication<sup>12</sup>.

Based on the understanding of the fictive temperature change for the formations of the waveguiding region, we could expect an increased  $n$  and therefore N. A. if the glass wafer were preannealed for a longer time duration. This approach was experimentally investigated. We learn that the annealing schedule for the CS-2-60 glass as prepared at Corning was as follows:<sup>3</sup>

- Heating from room temperature to annealing temperature within 15-20 minutes.



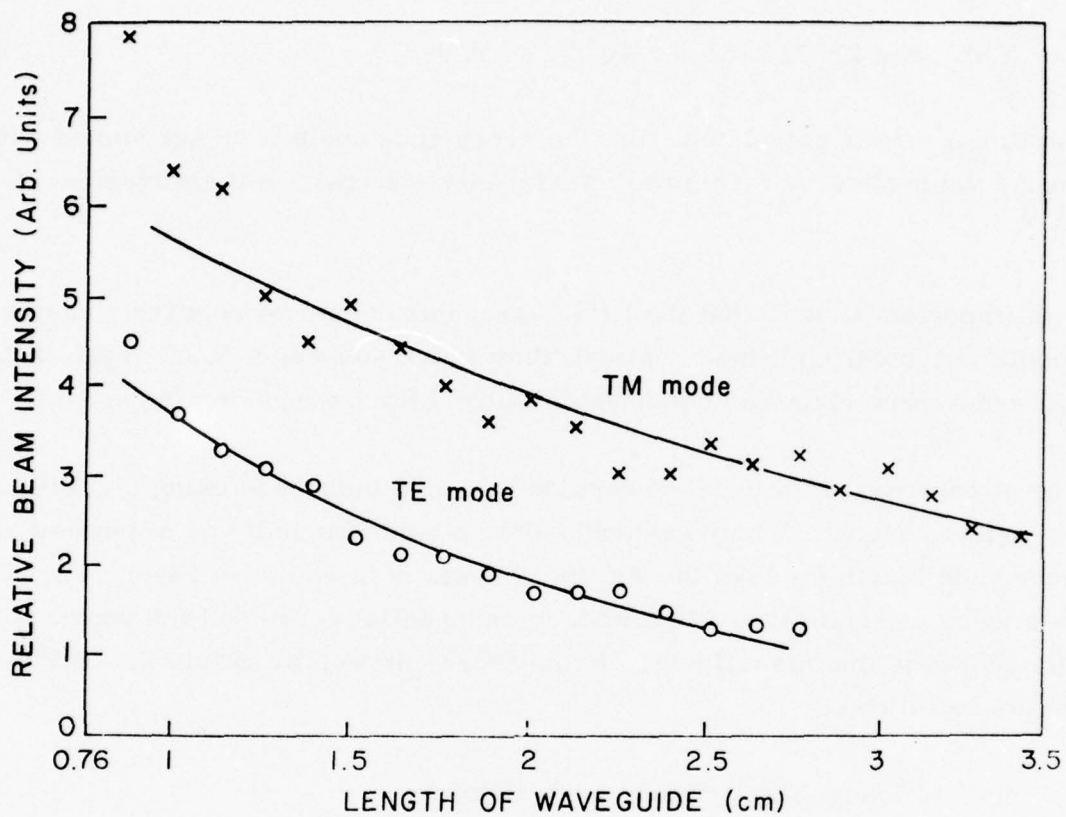


Figure 17. Relative beam intensity as a function of the LHSI waveguide path length for both the TM and TE modes.

- Stay at this temperature for about 1/2 or 1 hour.
- Cool back to strain point 501°C at a rate of 10°/minute.
- Cool to room temperature rapidly with furnace off.

To attempt to decrease the fictive temperature, we have chosen a slower cooling rate. The schedule adapted was as follows:

- Heating from room temperature to 600°C in 1/2 hour.
- Stay at this temperature for 2 hours.
- Cool back to 500°C at 6°/hour or 0.1°/minute.
- Cool to room temperature with furnace off.

Using two glass wafers cut from the same plate from Corning, we prepared one according to our new preannealing schedule and leaving the other untreated. LHSI waveguides were then made on both wafers under identical conditions. The measured waveguide acceptance angle for the preannealed sample is shown in Figure 18. It is seen that the half power aperture for the TE and TM modes are 9.5 and 10.5 minutes respectively, as compared to the as-received sample which gives an half power aperture of 8.5 minutes for both the TE and TM wave. This indicates that preannealing is effective for increasing the numerical aperture of the LHSI waveguide.

This result is a further indication that the fictive temperature of the glass plays an important role in the refractive index of the glass as was previously expected. However, our result shows the range of modification in  $\Delta n$  by slow preannealing is not very large.

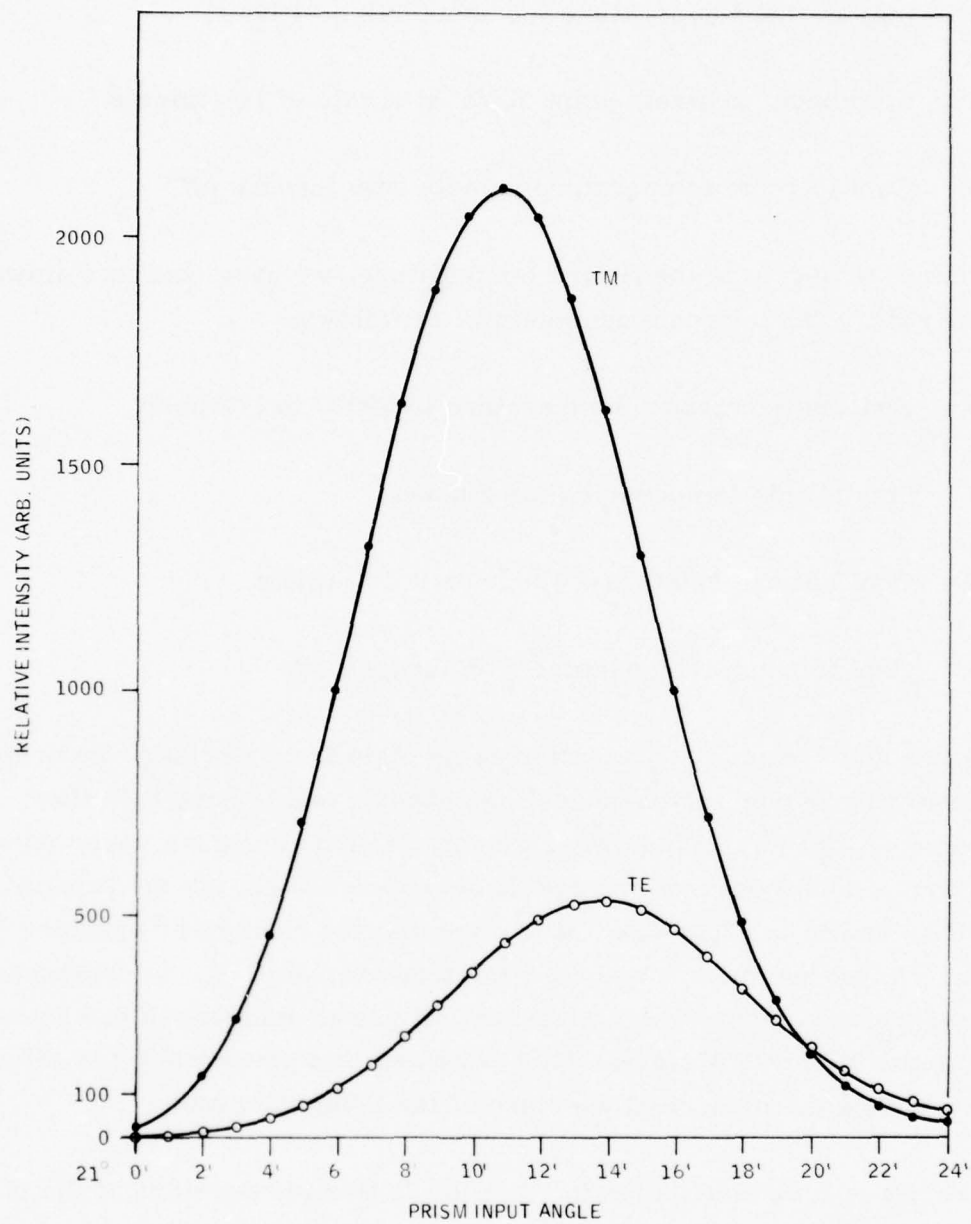


Figure 18. Relative beam intensity at a fixed point in the LHSI waveguides as a function of prism input angle for a preannealed sample.

### SECTION III

## FABRICATION OF LHSI WAVEGUIDE CIRCUIT ELEMENTS

### FABRICATION TECHNIQUE

#### The Laser Beam Exposure System

The use of a laser beam for LHSI waveguide fabrication offers a unique capability in the realization of complex optical waveguide devices. To implement this capability, a laser beam exposure system (LBES) was designed, constructed and tested. In this system the focused laser beam is stationary and the sample receiving the exposure is mounted on an x-y micropositioning stage, controlled by a microcomputer. An electronic shutter is also incorporated to control the beam on-off duration. This system has been used for the fabrication of channeled waveguide bends, mode selectors, and couplers. It should be applicable for multimode optical waveguide device fabrication where the waveguiding region is produced by the photon energy in the laser beam.

The schematic diagram of the LBES is shown in Figure 19. The laser employed for this system is a Coherent Radiation Model 52G Ar laser with an maximum all-line power output of about 1 watt. The laser beam is filtered by a spatial filter, controlled by an electronic shutter and is focused by a 30mm f. 1. lens operating at an F number of 2 to 3. The x-y micropositioning stage consists of two Aerotech model ATS-302M linear translators with stepping motor drive, driven by Aerotech model 200 drivers. A Motorola M6800 microprocessor ( $\mu$ P) was used to control the drivers of the microposition stages. The schematic diagram of the electronic circuits is shown in Figure 20, where the mnemonics are given in Table 2.



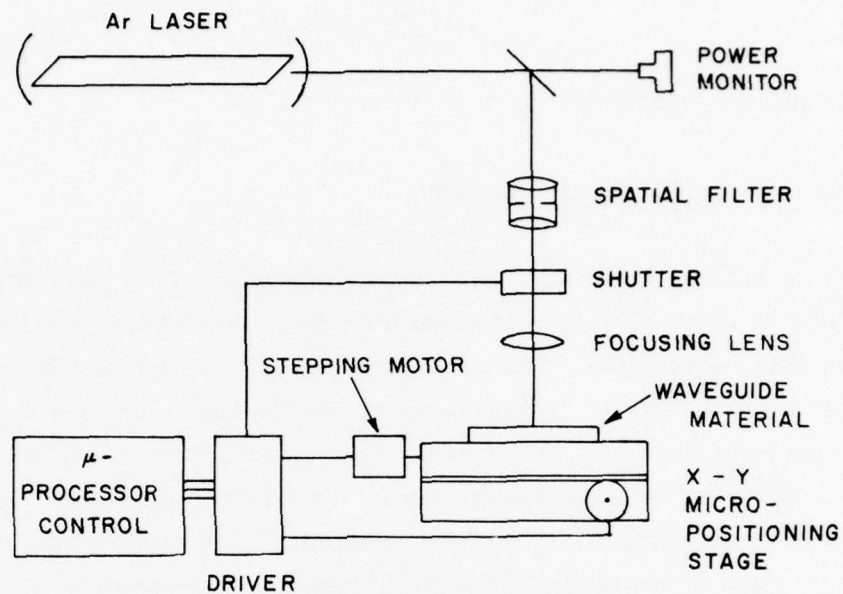


Figure 19. Schematic diagram of the laser beam exposure system (LBES).

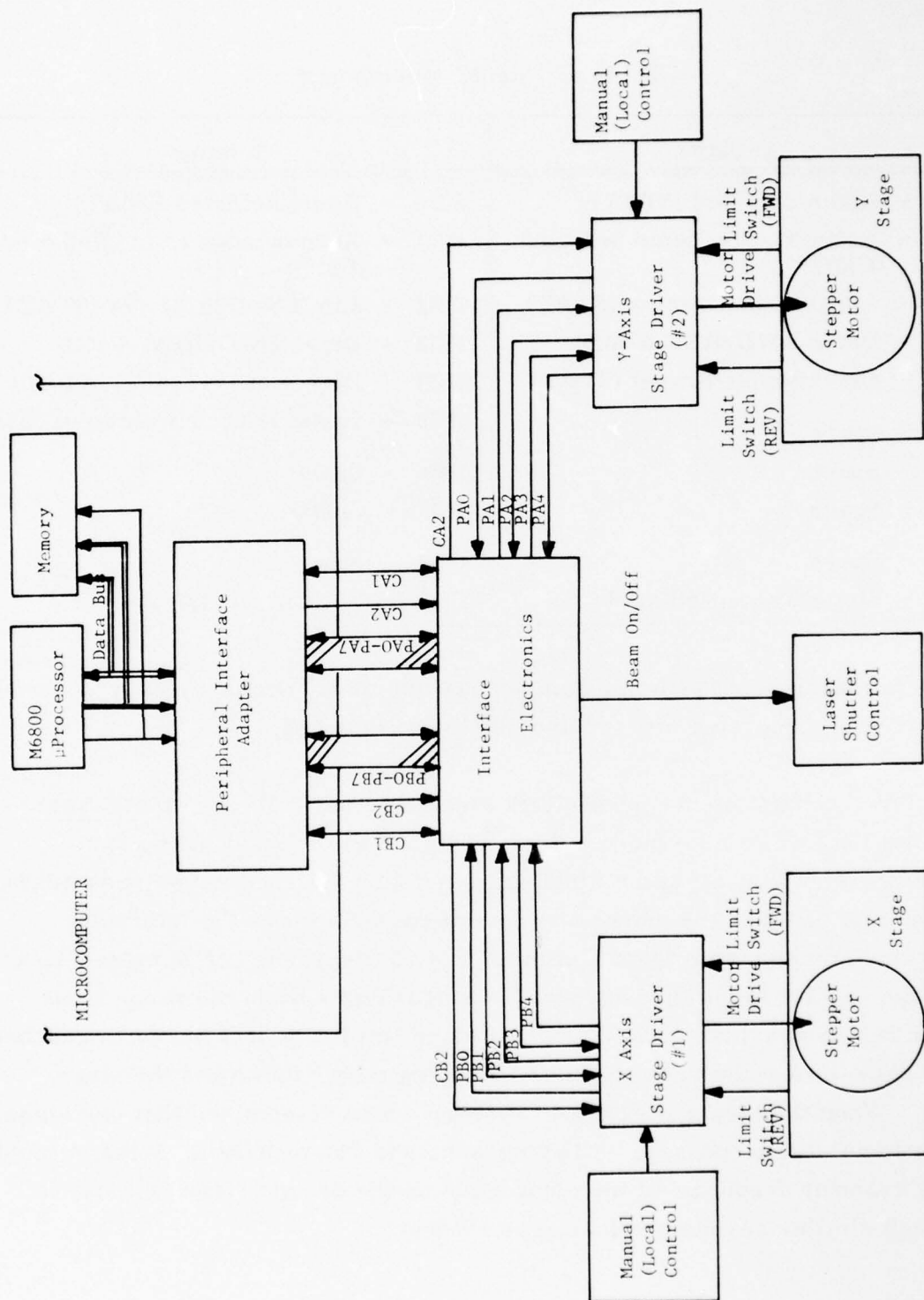


Figure 20. Block diagram of translation stage - Microprocessor Interface (see Table 3-1 for signal mnemonics).

Table 2. Signal Mnemonics

Y-Stage	X-Stage
PA0 - Home Selected (STAT)	PB0 - Home Selected (STAT)
PA1 - Acknowledge Home Selected (CMD)	PB1 - Acknowledge Home Selected (CMD)
PA2 - Limit Switch Active (STAT)	PB2 - Limit Switch Active (STAT)
PA3 - Drive FWD/REV (CMD)	PB3 - Drive FWD/REV (CMD)
PA4 - Direction of Travel (STAT)	PB4 - Direction of Travel (STAT)
PA5 - Spare	PB5 - Laser Shutter Control (CMD)
PA6 - Spare	PB6 - Spare
PA7 - Spare	PB7 - Spare
CA1 - Spare	CB1 - Spare
CA2 - Step Strobe (Y-Stage)	CB2 - Step Strobe (X-Stage)

In the following, the hardware components and their functions, as well as the software and programs utilized are discussed in detail.

The drives consist of two independent electronic packages capable of operation in a local or remote mode. When operated in the local mode, the direction, slew, on/off and a single step function are controlled by switches on the front panel of the drives. A potentiometer adjusts the internally generated stepping rate from a minimum of 55 steps/sec ( $27.5\mu\text{m}/\text{sec}$ ) to a maximum of 500 steps ( $250\mu\text{m}/\text{sec}$ ). An LED lights when the range limit switch has been actuated indicating the stage limit of travel has been reached. The range limit switch also removes stepping motor drive and the stage stops. When the stepping rate was varied, it was determined that one stage resonated at 192 steps/sec, 110 steps/sec, and 71 steps/sec. Measurements of the resonant frequencies were not made on the second stage (Y axis) although similar resonant points were evident.

When the stages are switched to the remote mode of operation, the M6800 microprocessor ( $\mu$ P) provides a 7 $\mu$ sec stepping trigger pulse to the stage driver. The stepping pulse triggers a one-shot multivibrator which stretches the pulse to the 30 $\mu$ sec width required by the driver circuitry. The stepping rate in the remote mode is entirely dependent on the rate at which the  $\mu$ P supplies the trigger pulses. The maximum pulse rate in the remote mode is approximately the same as in local mode, although the  $\mu$ P is capable of supplying step pulses at a rate much higher than the stepper motor is capable of stepping.

The  $\mu$ P interface also provides the exchange of status signals which will indicate whether the "home select" (initializes origin point) switch has been actuated, the travel limit switches have been actuated, and the direction the stage is stepping. Command signals sent to the driver stage consist of the step strobe, the "acknowledge home selected" command which will reset the home select F/F, the drive forward/reverse signal, and a command which will open or close the laser shutter.

The microcomputer consists of an M6800 microprocessor situated on a Motorola MEK6800D1 evaluation PCB along with a ROM (MCM6830L7, MIKBUG) and associated RAM (MCM6810), a peripheral interface adapter (PIA, MCM6820) for communication with a Teletype (TTY) or other RS232 compatible communication device, and a PIA for communication with the translation stages.

A separate memory card was constructed which expanded the basic evaluation PCB memory capacity from 640 words to 1536 words. This card is isolated from the evaluation PCB bus by a bus expander card (using National 8833 party line transceivers) which will allow up to 100 MOS devices to be placed on the buffered bus.



The PIA used for translation stage interfacing has 16 parallel programmable I/O lines and 4 control lines. Two control lines are strictly input and can be programmed by the  $\mu$ P to generate an interrupt request on the rising or falling edge of the input applied by the peripheral device. The other two control lines may be programmed to act as either input or output. In the present program configuration, they are both used as outputs to strobe the two translation stage drivers. Presently, the interrupt request feature of the PIA is not utilized. The microcomputer operates at a basic cycle time of 2 microseconds.

#### Microprocessor Controlled Program

The goal was to develop a program which would control the stepping velocity and number of steps of both the X-axis and Y-axis stepping motors on the Aerotech translation stages. This would provide the control needed to provide laser beam exposure such as the LHSI optical waveguide using the argon laser.

The approach taken in designing the software program involved building a set of short subroutines which control the functions in the translation stages, configure the PIA control registers, perform double word arithmetic, determine time delays for pulsing the axis, count the number of pulses, input initial parameters from the TTY, convert decimal input to binary, control the laser shutter, and supply a debug subroutine which will output the contents of the program counter, X-register, A-register and B-register.

The program in it's present form contains subroutines which are not utilized but available for future improvements in the program. The program has not been optimized with respect to execution time and also contains many "no operation (NOP)" commands which serve as break points for insertion of a "jump to debug" subroutine. The NOP command also allow temporary modification of the program without the necessity of generating a new object

tape on the Honeywell computer network (HCN) which is a very time consuming process. As the number of modifications accumulate, it eventually becomes necessary to return to the HCN system to update the source file program and generate a new assembly listing and object tape.

Figure 21 shows the main program flow chart and Figure 22 shows the Pulse Command word modification subroutine flow chart. The present program begins by allowing entry of initial decimal parameters. The parameters are converted to binary form and scored in constant locations. They consist of a step count along the X-axis (used to write horizontal line), a step count which is used in the curve subroutine (counts X-axis pulses only) and a step count which is used in the diagonal subroutine (again only X-axis pulses are counted). Multiplier constants are entered for use in the curve subroutine. These multipliers determine the number of pulses issued at any particular rate before the rates are changed by fixed delta constants previously entered for the X and Y axes. The multipliers essentially determine the radius of the curve. The X and Y axes stepping rate will also be a factor in radius determination.

When the X count for the horizontal line, curves line, and diagonal have been entered and converted to binary form, the program allows entry of the X and Y axes multipliers, the initial X and Y axes velocities in the form of words to be counted down and the fixed delta counts which will be added to the X count thus decreasing the X velocity by the fixed delta, and subtracted from the Y count thus increasing the Y velocity by the fixed delta. These decimal entries are also converted to binary.

After the parameters are entered, the program proceeds to configure the PIA. One eight bit port interfaces the X-axis driver and the second eight-bit port interfaces the Y-axis driver. The data direction mask for each port is written in the appropriate data direction register in the PIA then the I/O capability becomes active upon the command to open the peripheral data registers.

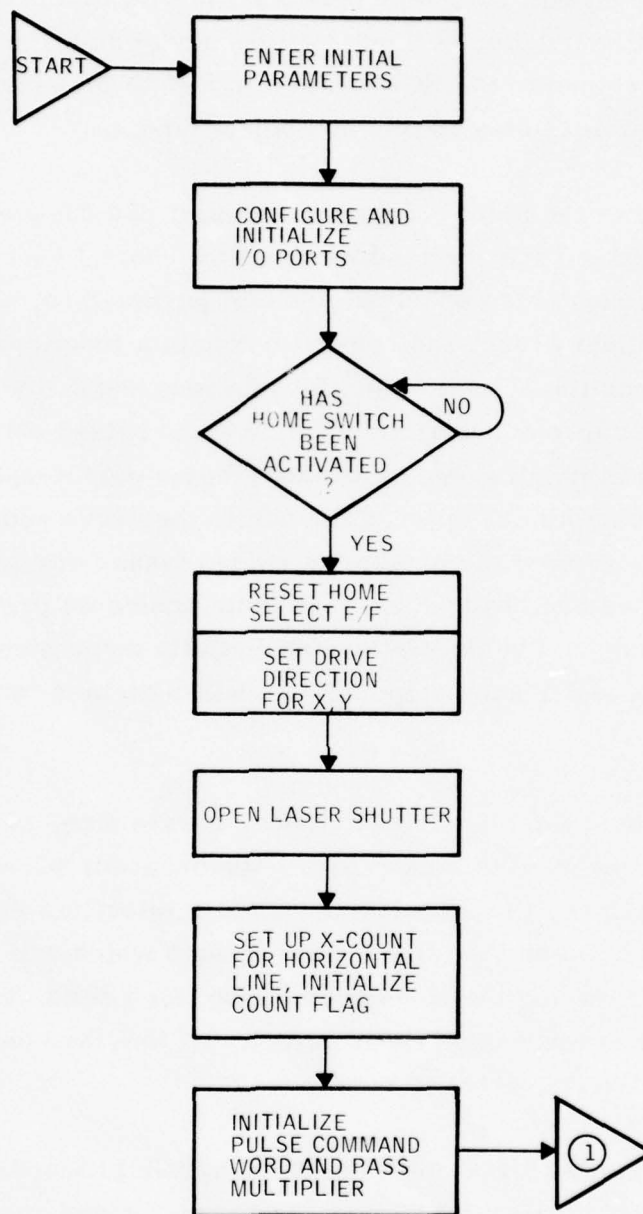


Figure 21. LBES Control Main Program flow chart. (1 of 5)

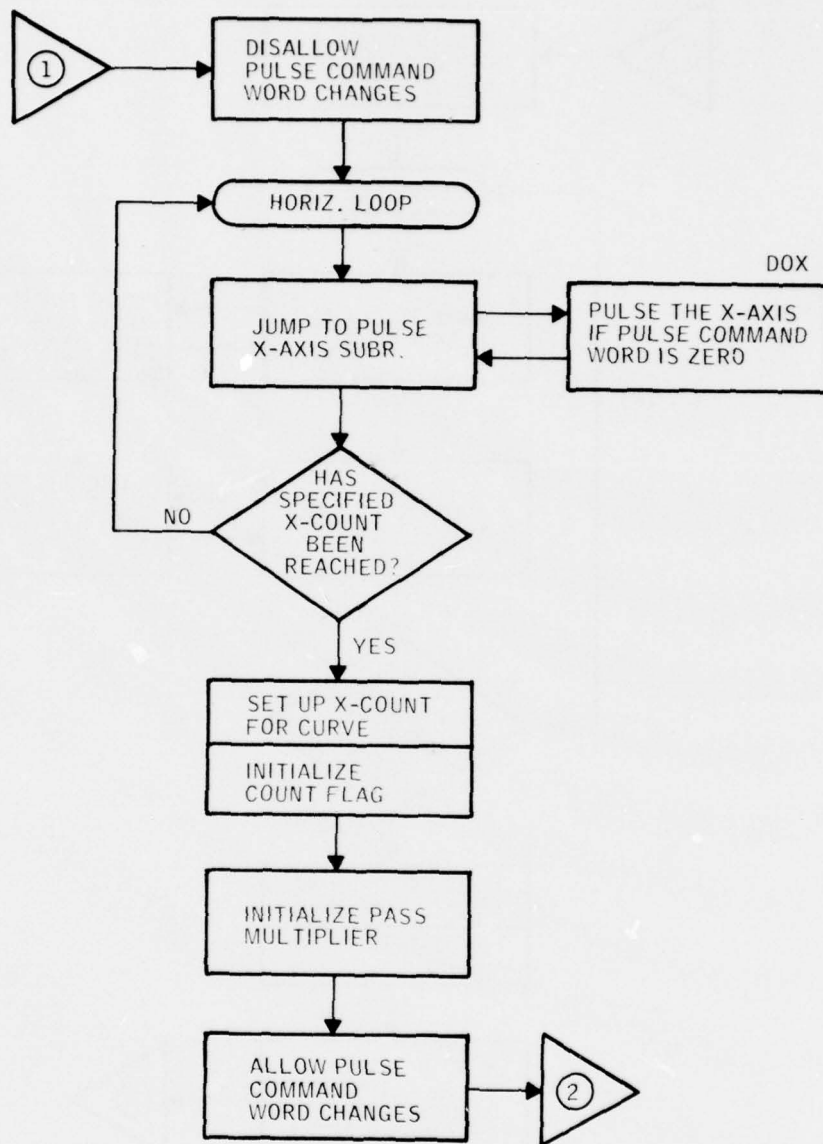


Figure 21. LBES Control Main Program flow chart. (2 of 5)



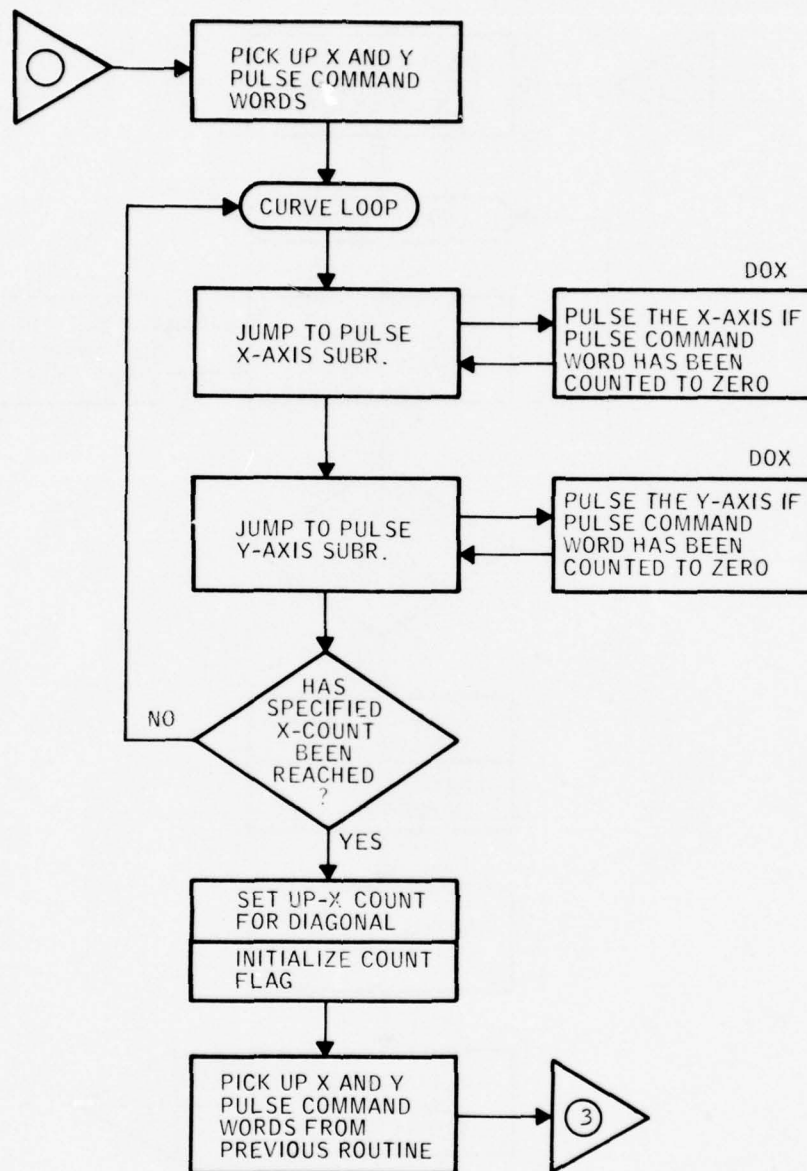


Figure 21. LBES Control Main Program flow chart. (3 of 5)

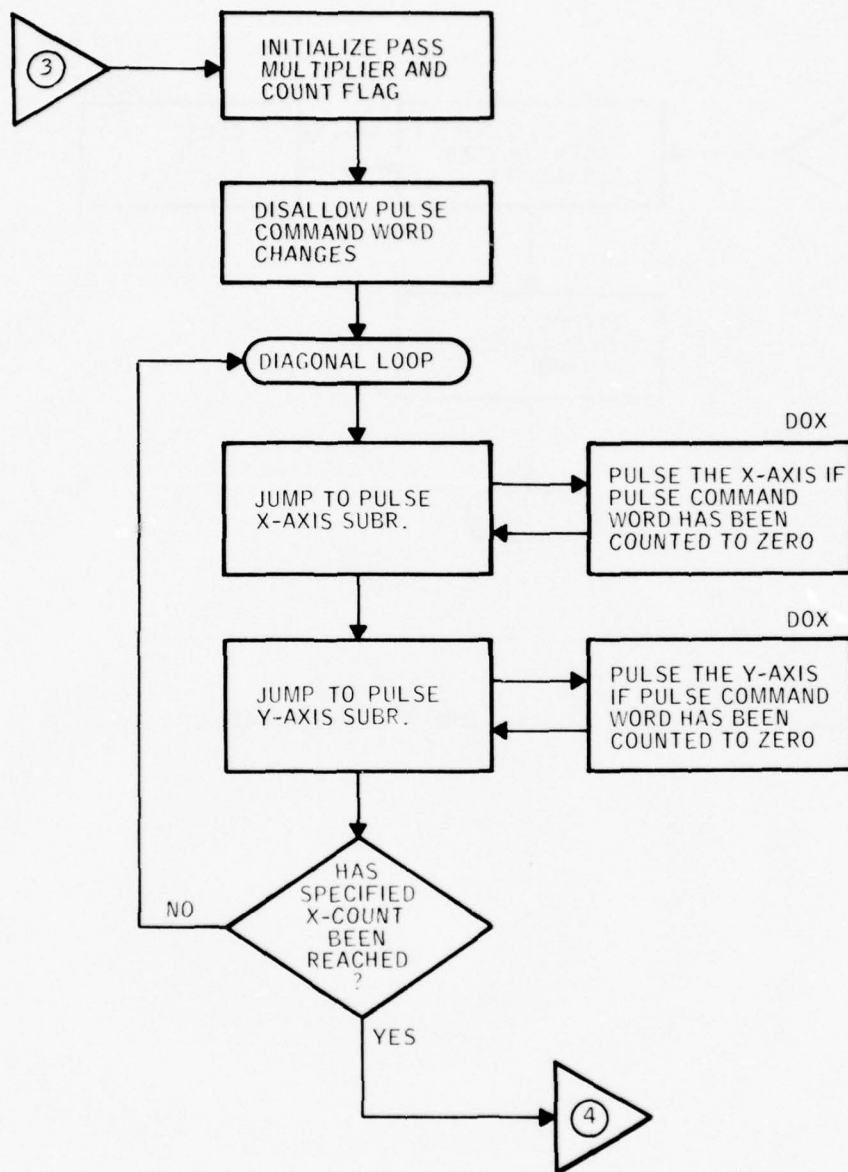


Figure 21. LBES Control Main Program flow chart. (4 of 5)

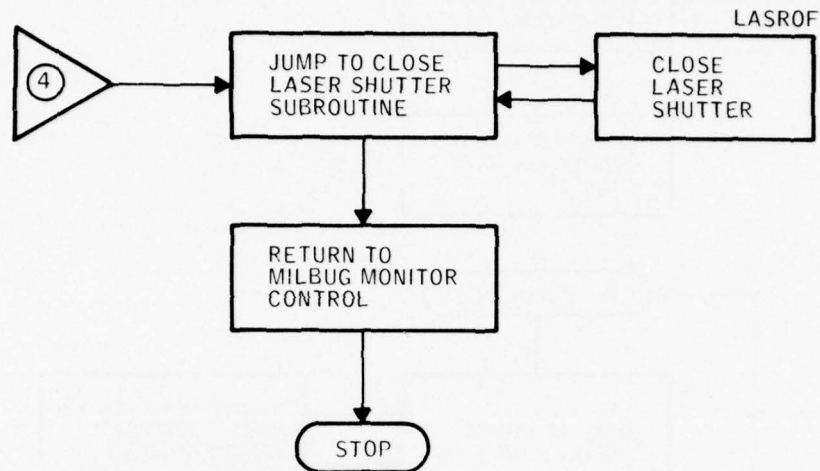


Figure 21. LBES Control Main Program flow chart. (5 of 5)

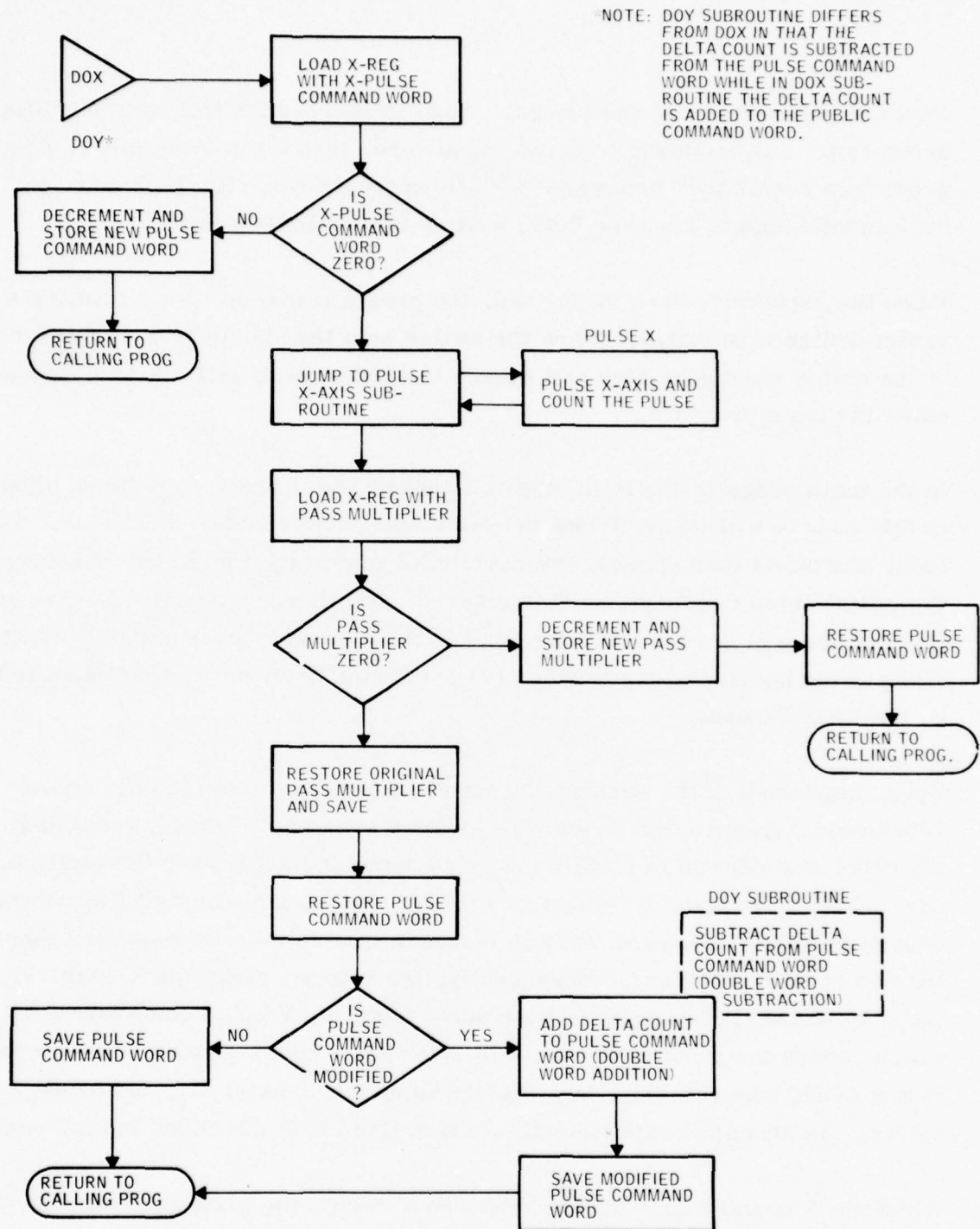


Figure 22. LBES control pulse command word modification flow chart.



Next the port words are initialized. When initialized the following conditions are set up. All command bits are set to zero, then bit 1 is set high. This procedure resets the "home select" F/F in the driver. On the X-axis port, bit 5 is held high to keep the laser shutter in the closed position.

When the ports have been initialized, the program will now loop until the home select switch is actuated. When the switch sets the "home select" F/F, bit 0 of the status word goes high and causes the program to exit the wait loop and enter the main program.

In the main program the first step is to set up the X and Y axes drive direction. In this case X will drive clockwise and Y will drive counter-clockwise. The laser shutter is then opened, the horizontal count is set up in the counter and the initial pulse command word is entered. The horizontal pulse loop is now entered and will not exit until the total X count equals the required X count. When in the horizontal pulse loop, the pulse command word is not modified by the delta X count.

Upon completion of the horizontal count, the program jumps to the curve subroutine. A new count is entered in the X counter. Both  $\Delta X$  count and  $\Delta Y$  count are allowed to modify the pulse command word when the multipliers have counted to zero.  $\Delta X$  count is added to the X pulse command word which causes the pulse command word to increase in size thereby requiring more time to count to zero and, consequently, the velocity along the X-axis,  $V_X$ , becomes slower.  $\Delta Y$  count is subtracted from the Y pulse command word which causes the word to decrease in size thus requiring less time to count to zero and, consequently, the velocity along the Y-axis,  $V_Y$ , becomes faster. As an initial experiment, we have fixed both  $\Delta X$  count and  $\Delta Y$  count.

When the X counter reaches the required X count, the program branches to the diagonal subroutine which essentially freezes the X and Y pulse command words thus fixing the  $V_X$  and  $V_Y$ . The resulting diagonal continues until the

diagonal X count reaches the required X count entered in the initial parameters. The program exits the diagonal loop, the laser shutter is closed, and the computer is returned to MIKBUG control.

A number of channel waveguides based on the laser heating strain induced (LHSI) technique was made using the LBES facility. The results are discussed in the following subsection.

#### PROPERTIES OF WAVEGUIDE CIRCUIT ELEMENTS

Demonstration of some of the simple waveguide circuits that can be made using the LHSI technique were performed. In the following we discuss the results of the properties of these waveguide devices.

##### LHSI Waveguide Constriction

A continuous straight LHSI waveguide consisting of a wide part and a narrow part joined together was made by power reduction to 80% of the initial value in the middle of a scanning. The resultant waveguide has a cross-sectional dimension of  $70\mu\text{m}$  radius in the wide part and a  $15\mu\text{m}$  radius in the narrow part. The waveguide acceptance angle were then measured for both the narrow and the wide part of the constriction with beam input coupled from the wide waveguide. The result is shown in Figure 23. It is most unexpected to observe that the acceptance angle for the TM and TE modes for both parts of the constricted waveguide to be about the same ( $\sim 9$  minutes). This result may be due to the efficient coupling from the wide guide to the narrow guide by the tapered constriction.

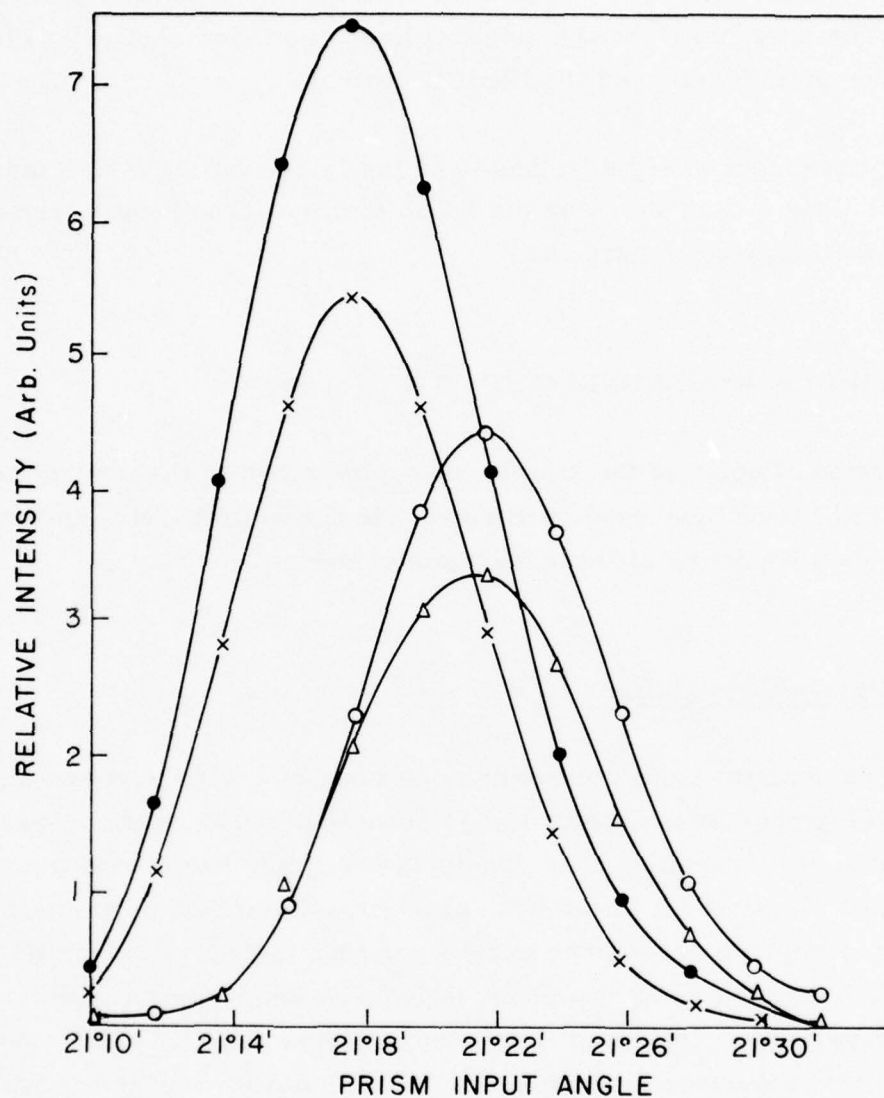


Figure 23. Relative beam intensity measured at narrow and wide part of a constructed LHSI waveguide, as a function of prism input angle. The data for the wide part are  $\bullet$  - TM and  $\circ$  - TE mode and those for the narrow part are  $\times$  - TM and  $\Delta$  - TE modes.

### LHSI Waveguide Bends

The waveguide bending loss could be treated by an analysis given by Gloge<sup>15</sup>. To be useful in constructing integrated optical circuits, LHSI guides will have to possess acceptably low losses in the bends used to distribute the light along the various branches. We consider these losses here, again using the parabolic-index fiber as our model.

The major losses in multi-mode fibers are caused by higher-order modes striking the interface at less than the critical angle. These modes become leaky rather than bounded and after some distance have lost their energy. The fraction of modes lost in a bend of radius  $R$  in a parabolic-index fiber is<sup>15</sup>

$$y = \frac{2a}{R\Delta} \quad (39)$$

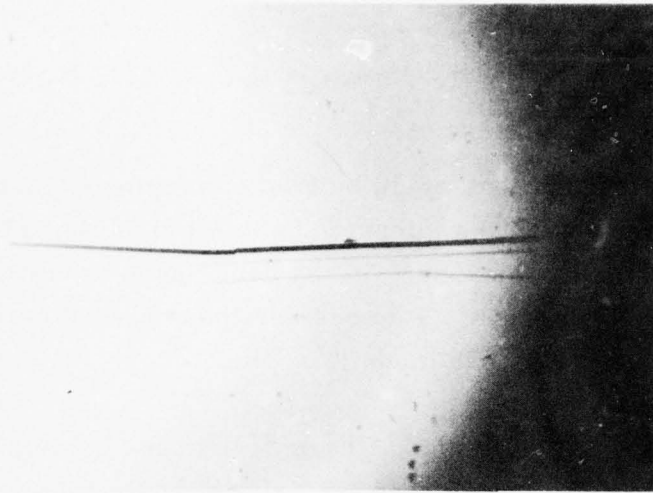
where  $a$  is the fiber radius,  $\Delta = (n_a^2 - n_b^2) / n_b^2 = 2\Delta n / n_b$  and  $\Delta n = n_a - n_b$ . This is independent of the angle of the bend, and is actually an upper limit on loss assuming all energy in a leaky mode is immediately lost.

Typical LHSI guides have  $a = 50\mu\text{m}$ ,  $\Delta n = 10^{-3}$ , and  $n_b = 1.5$ , which gives  $\Delta = 1.33 \times 10^{-3}$  and the product  $yR = 7.5\text{cm}$ . So to limit the fraction of modes becoming leaky to  $y = 0.1$  (0.5dB) requires a bend of 75cm.

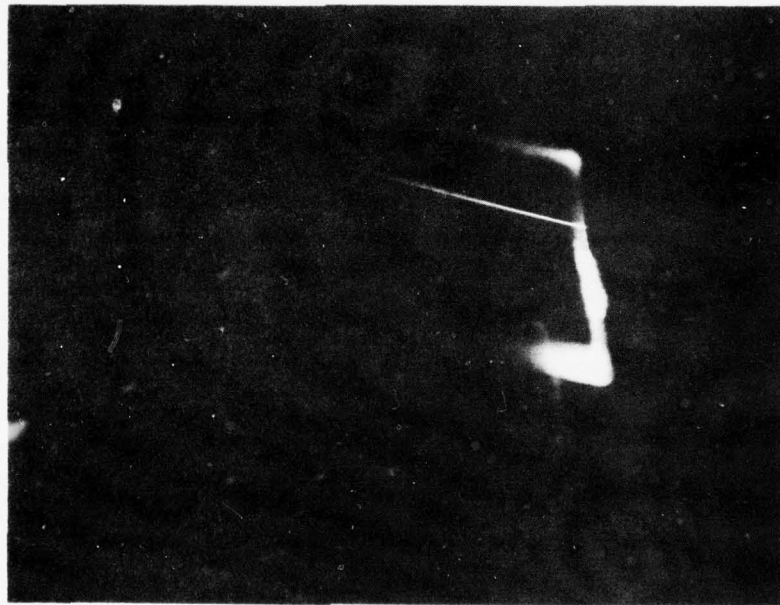
Those bending losses and minimum bend radii are probably acceptable for the construction of integrated optical circuits, although it may be desirable to obtain guides with tighter confinement (larger  $\Delta n/n$ ) to lower these losses.

Experimentally, we have made waveguide bends by the LBES, with a bending radius approaching 10cm. Figure 24(a) shows such a waveguide bend. Figure 24(b) depicts a HeNe laser beam propagating through such a bend. The beam intensity measured along the bend gives the bending loss of 5db/cm.





(a)



(b)

Figure 24. Photograph of a LHSI waveguide bend produced by LBES:  
(a) dark-field photograph of waveguide; (b) photograph  
of laser beam propagating through the bend.

### LHSI Waveguide Gaps

We have also made straight waveguides with a gap of various length. The gap should serve as a mode selector since higher order modes leaving the end of a straight waveguide will not be able to couple into another section of the waveguide at a distance away. This will result in a reduction of the beam intensity in the LHSI waveguide as the gap width increases. We have observed this effect by measuring the intensity of the beam at the output prism coupler with the input prism at a fixed distance (2.3cm) away from it. This 2.3cm waveguide path includes a gap of varying width. An example of the measured output is shown in the following tabulation (arbitrary units of intensity):

<u>Distance Measured from Input Prism</u>	<u>Gap Spacing Beginning 2cm from Input Prism</u>		
	<u>0</u>	<u>0.5mm</u>	<u>2.5mm</u>
1.5cm	5.42	3.92	3.29
2.3cm	3.13	1.52	0.163

It is seen that the additional loss is 1.7db for the 0.5mm gap and 11db for the 2.5mm gap. Giving an average loss of 4db/mm of gap spacing.

### LHSI Waveguide Coupler

A waveguide directional coupler was designed based on the fact that optical wave can propagate through a gap and a bend in the LHSI waveguide as discussed previously. A schematic diagram of such a coupler is shown in Figure 25. The wave propagating from port A will exist at B through a bend and at C through a gap. But there is very little coupling to port D if coupling between adjacent waveguides is small. Similar result is obtained for input from C.

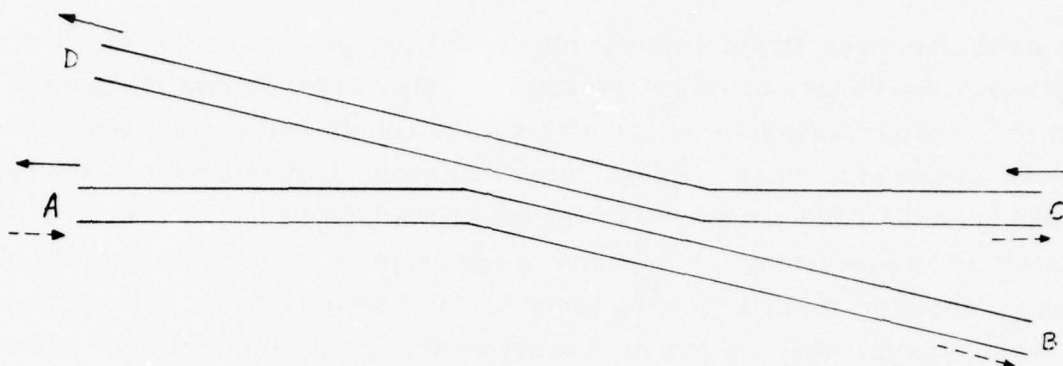


Figure 25. Schematic of a LHSI waveguide directional coupler.

To assure that coupling between adjacent waveguides are small, we have made an analysis of the coupling between modes of adjacent multimode parabolic-index fibers which can be applied to LHSI guides. The mathematics are involved and follow the method of Marcuse<sup>16</sup>. We consider the modes of each guide to be unaffected by the presence of the other with the electric field amplitudes given by the same expressions used in the preceeding section. Some integrals must be evaluated numerically.

The results of those calculations are best expressed qualitatively as follows:

- For a mode described by mode indices  $m, n$  in Cartesian coordinates, coupling is limited to modes in the other guide with indices  $m', n'$  satisfying:

$$m', n' = \begin{matrix} m, n \\ m+2, n-2 \\ m-2, n+2 \end{matrix} \quad (40)$$

Since mode effective index depends only on the sum  $(m+n+1)$ , we see that the modes which are coupled propagate with the same phase velocity.

- For a fixed spacing between adjacent guides, only the highest-order modes (lowest effective index) which can still be identified as belonging to a single fiber are significantly coupled. Lower-order modes are much more tightly confined by the graded index profile, overlap very little, and are coupled more weakly by several orders of magnitude.
- For a given pair of coupled modes, the strength of the coupling decreases very quickly with increasing guide separation, typically several orders of magnitude for a change in separation of one diameter.

In summary, appreciable coupling occurs only between a few modes at a time in adjacent multimode parabolic-index guides. This renders unsuitable the coupled-adjacent-waveguide approach used with single-mode step-index guides for designing directional couplers, etc. We are therefore assured that as long as the parallel section of the directional coupler is more than one radius of the waveguide diameter apart, cross talk will be negligible.

We have made one such directional coupler with a gap spacing of 1.0mm and a bending of 5 degrees. The directionality of the coupler was easily observed. However, the losses of the coupler is about 10db to each forward branch. Further improvement is needed to reduce this loss.



#### SECTION IV

### RESIDUAL AND INDUCED STRAIN IN WAVEGUIDE MATERIALS

#### POLISHING-INDUCED RESIDUAL STRAIN

When a surface is abrasively machined by finish grinding, lapping and polishing, a highly deformed layer adjacent to the surface is produced<sup>17-20</sup>. In non-metallic crystalline solids with high yield points the deformed layer is fairly shallow and the boundary between the deformed zone and the underlying bulk material can be very sharp<sup>17-20</sup>. The residual stresses (and strains) in these machined layers are compressive if extensive heating does not occur during machining<sup>20</sup>. In polishing operations heating is minimal. The residual compressive stresses arise from the fact that the deformation taking place during polishing is, in essence, a type of "smearing" that tends to increase the lateral dimensions of the polished surface. The increase in surface area is resisted by the underlying bulk and the deformed layer is put in a state of biaxial compression. If the strain optic coefficient  $\frac{dn}{dS}$ , where  $n$  is the index of refraction and  $S$  is the strain, is negative, the index in the deformed layer will increase as a result of polishing and the layer could act as a waveguide. This is the situation found by Chen et al in polished PLZT<sup>1</sup>. In this study we have extended their observations on PLZT and have systematically attempted to introduce a waveguiding surface layer in a material with a negative strain optic coefficient and a much simpler microstructure than PLZT, namely single crystal lithium niobate ( $\text{LiNbO}_3$ ). In what follows, the results of the study of PLZT waveguides are presented first followed by the discussion of waveguiding in  $\text{LiNbO}_3$  (LN) crystals.

### Waveguiding in PLZT

In a material such as PLZT ceramic, the magnitude of the photoelastic coefficient  $p$  is expected to be about  $0.2^{25}$ . The polishing-induced strain  $S$  for this case could be in the range of<sup>17</sup>  $10^{-3} < S < 10^{-2}$ . Since the refractive index is 2.5, if we assume  $S = 10^{-2}$ , the polishing-induced refractive index could be as high as  $10^{-2}$ . If the layer thickness  $W$  is a few  $\mu\text{m}$ , as expected<sup>18</sup> there will be a few TE and TM modes that could propagate in the polished layer of PLZT wafer. Experimentally, we have achieved optical waveguiding in polished PLZT wafer. The measured waveguide effective refractive index for the two lowest-order TE modes gives a best fit value of

$$\Delta n \approx 0.018 \text{ and } W \approx 2.33\mu\text{m}$$

This result was obtained in an earlier research work entitled "An Investigation of PLZT for Interpreted Optics" supported by the Office of Naval Research. Further details could be found in the final report<sup>1</sup> of that research work.

### Polishing-Induced Strain in LN Crystals

Our choice of studying strain-induced waveguiding in a single crystal as opposed to a polycrystalline material such as PLZT is based on the idea that, first, characterization of the waveguiding layer is easier in the crystal and, second, that the anisotropic properties of the crystal could be used to our advantage. Briefly, the study consisted of first giving different crystallographic faces a number of different polishing treatments. The nature and extent of deformation and damage in the polished layers were then characterized by x-ray techniques and by direct observation in an optical and a scanning electron microscope. Finally, the polished surfaces were then checked to determine if they guided a wave from a HeNe laser.

Experimental Procedure -- The experimental procedure employed is described in the following paragraphs.

Polishing Technique -- The samples were polished in a five-step operation similar to that used to prepare surfaces for microscopic examination. For lapping and polishing the samples were mounted on metal discs with a hot melting wax. Cylindrical conditioning rings were used to maintain flatness during lapping and lithium niobate "feet" were cemented to the outside of the specimen holder to maintain flatness during polishing. The five stages of surface preparation were:

- Stage 1 -- Lapped with a  $12\mu\text{m}$  SiC slurry on cast iron using a Gyromatic 12 precision lapping machine. An abrasive concentration of 20gm/liter of distilled water was used at a rotation rate of 60 rpm. When the downward stress on the sample was 3 psi the material removal rate was approximately  $12\mu\text{m}/\text{min}$ .
- Stage 2 -- Lapped with a  $3\mu\text{m}$   $\text{Al}_2\text{O}_3$  slurry on cast iron using a Frantz "unipol" lapping machine. An abrasive concentration of 10gm/liter of distilled water was used at a rotation rate of 90 rpm. The removal rate was approximately  $6\mu\text{m}/\text{min}$ .
- Stage 3 -- Lapped for 15 minutes with the same  $\text{Al}_2\text{O}_3$  slurry on the same machine using a lead lap. The removal rate was approximately  $1\mu\text{m}/\text{min}$ .
- Stage 4 -- Hand polished for several minutes with  $3\mu\text{m}$  diamond abrasive on Metcloth\* rotating at 550 rpm. Kerosene was used as a carrier for the abrasive.

---

\*A. B. Buhler Co.

- Stage 5 -- Polished for one to two hours with cerium oxide on a Pellon PANW lap using a Strasbough RGY Precision Polishmaster machine operating at 80 rpm.

Examination of Lapped and Polished Surfaces -- The  $\text{LiNbO}_3$  samples were examined at all stages of preparation optically and with a Cambridge Instruments Model S4-10 scanning electron microscope. To prevent charging while in the SEM the samples were coated with carbon.

Characterization of Surfaces by X-Ray Techniques -- One of the ways to characterize the highly deformed subsurface layer introduced by lapping and polishing is by x-ray techniques. The residual stresses in the layer cause changes in the lattice parameters which may be detected by x-rays. The changes may be subtle so precision techniques are necessary. In this study we used Bond's technique<sup>21</sup> to measure the changes in lattice parameter perpendicular to the surface resulting from the biaxial stresses in the layer parallel to the surface. The two are related by Poisson's ratio with the changes perpendicular to the stresses being about three times the changes parallel to the surface.

The Bond technique uses a symmetrical diffractometer such as shown in Figure 26. The crystal is rotated till a reflection is detected in the upper detector. It is then rotated till the same reflection is detected in the lower detector. By accurately measuring the angle between the two reflecting positions the lattice parameters can be measured to a few ppm.

The necessary sensitivity can be discussed in terms of the angular changes that need to be measured to detect strains in the deformed layer on the order of 1 to 10 ppm. The sensitivity requirements for x-ray measurements of lattice parameters are found from Bragg's Law,  $n\lambda = 2d \sin \theta$  where  $n$  is an integer,  $\lambda$  the wavelength,  $d$  the interplanar spacing and  $\theta$  the diffraction



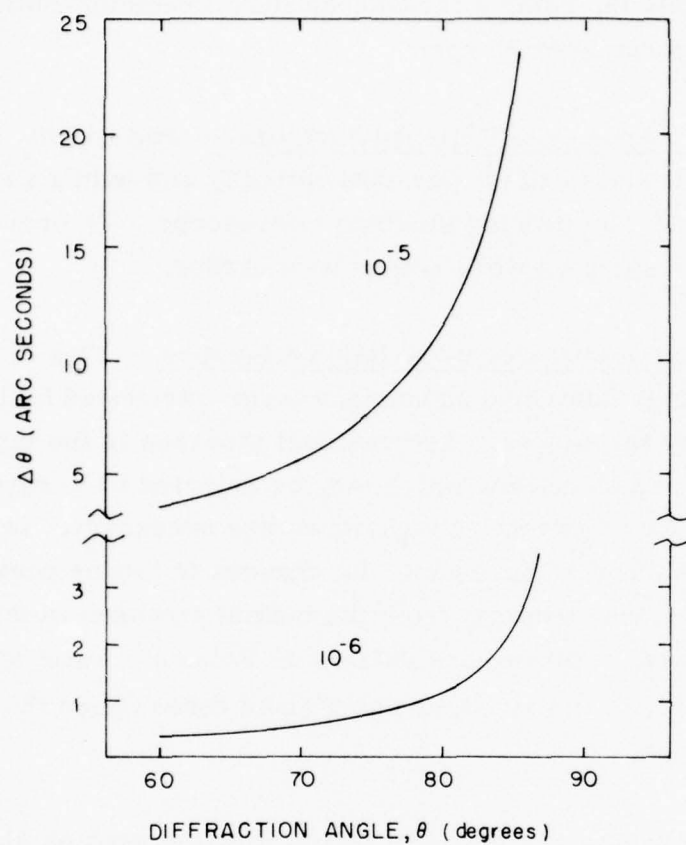


Figure 26. Schematic showing the Bond symmetrical diffractometer.

angle. Straining the lattice causes a change in  $d$ . Thus, from the first derivative of Bragg's Law

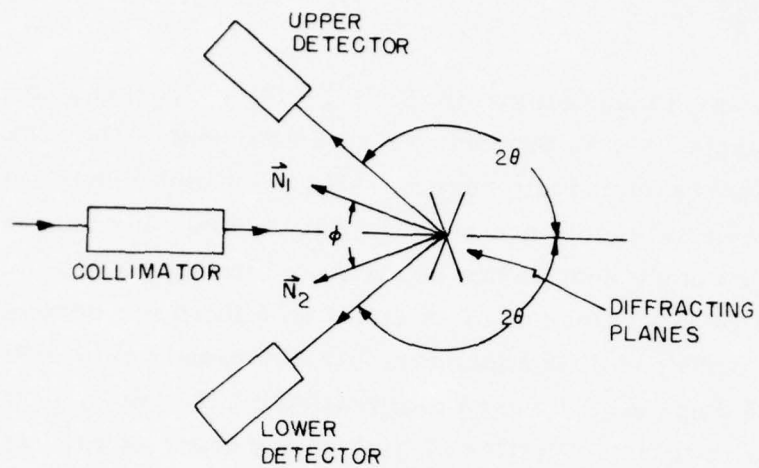
$$\Delta\theta = - \frac{\Delta d}{d} \tan \theta \quad (41)$$

we see that, for a constant strain ( $S = \frac{\Delta d}{d}$ ) the corresponding change in diffraction angle,  $\Delta\theta$ , is proportional to the tangent of the diffraction angle. Since  $\tan \theta$  increases rapidly near  $\theta = 90^\circ$ , most high-sensitivity lattice parameter measurements are made in this region. The increase in  $\Delta\theta$  as the diffraction angle approaches  $90^\circ$  is shown in Figure 27 for lattice strains of  $10^{-5}$  and  $10^{-6}$ . Values of  $\Delta\theta$  as small as 5 to 10 arc seconds can be detected by our Bond diffractometer. As discussed below diffraction angles of around 75 degrees were used to investigate LN. As seen from Figure 27 this enabled us to detect lattice strains on the order of  $10^{-5}$  with the diffractometer. A brief description of the diffractometer is given next followed by a discussion of the accuracy and errors inherent in the device.

The Bond symmetrical diffractometer, as shown in Figure 26, consists of three main components:

- An x-ray source and collimator
- A specimen holder attached to a sensitive angle measuring device
- Dual x-ray detectors

The diffraction angle  $\theta$  is obtained from  $\theta^\circ(\text{deg}) = 90^\circ - (N_1 - N_2)/2$  where  $N_1$  and  $N_2$  are the angular positions of the diffracting plane normals in the upper and lower diffracting positions respectively. Since the highest resolution is obtained at diffraction angles near 90 degrees the x-ray source must be properly selected.



DIFFRACTION ANGLE  $\theta = 90 - \phi/2$   
 $\vec{N}_1$  AND  $\vec{N}_2$  ARE DIFFRACTION PLANE  
 NORMALS AT UPPER AND LOWER  
 DIFFRACTING POSITIONS RESPECTIVELY

Figure 27. Change in diffraction angle  $\Delta \theta$  caused by strain plotted as a function of diffraction angle,  $\theta$ . Curves for strains of  $10^{-5}$  and  $10^{-6}$  are plotted.

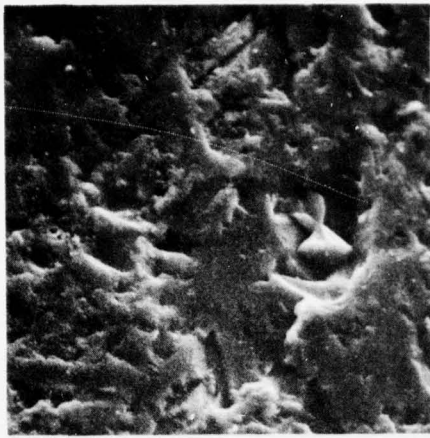
The symmetrical configuration eliminates many errors. However, some errors such as incident beam axial divergence, refraction and the Lorentz Polarization Factor error are still present. These errors can be readily treated mathematically and, in fact, are small at large values of  $\theta$ .

The x-rays are produced by a standard x-ray tube with a 1mm x 10mm line source. Slits positioned between the source and the sample allow a  $150\mu\text{m}$  x 1mm beam to impinge on the sample. The crystals were mounted on the rotating sample holder of a Phillips powder diffractometer. Beu has shown<sup>22</sup> the angular sensitivity of this type of support is insufficient to measure the  $\Delta\theta$  of 5 to 10 seconds needed to detect  $10^{-5}$  strain (see Figure 27). For this reason an autocollimator and high quality optical angle standards were used to make the measurements. This is a standard technique for making angle measurements<sup>23</sup>. With this setup we were able to measure  $\Delta\theta$  to 4 seconds.

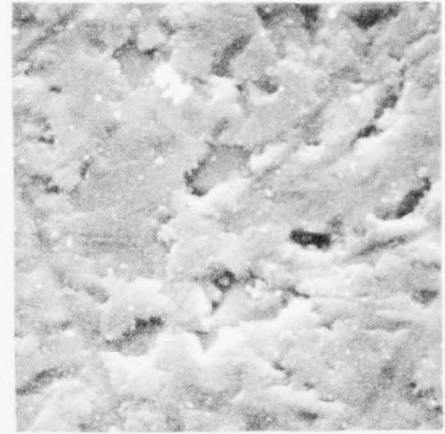
Results and Discussion -- Experimental results are discussed in the following paragraphs.

SEM Characterization of Lapped and Polished LN Crystal Faces -- Our goal in this portion of the study was to introduce plastically deformed layers on LN crystal faces by lapping and polishing. Based on previous experience<sup>24</sup> the plastic deformation resulting from an abrasive machining operation can be revealed by electron microscopy. In the present work, scanning electron micrographs were made of the LN crystal faces after each lapping and polishing step to follow the development of the deformed layer. Figures 28 through 31 are scanning electron micrographs at 2000X which illustrate the nature of the four crystal faces after each of the five lapping and polishing steps. Figure 28 shows the effects of machining on the (0001) face. The rough regions on the lapped surfaces are where material has been removed by brittle fracture. The smooth patches are where material was removed by plastic deformation, i. e., the regions are "smeared". As finer lapping conditions are used, the extent of brittle fracture on the surfaces decreases.

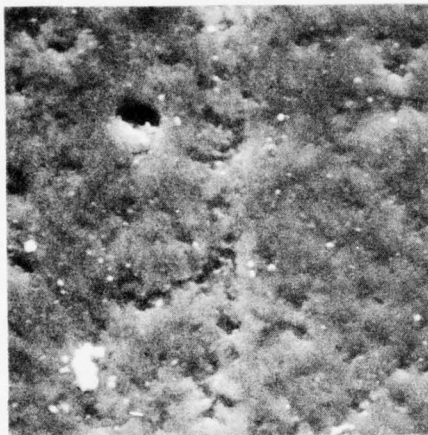




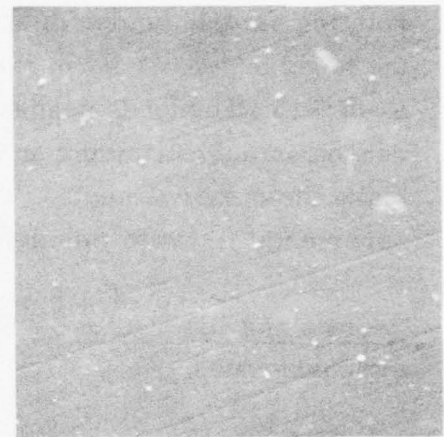
A 12μ SiC



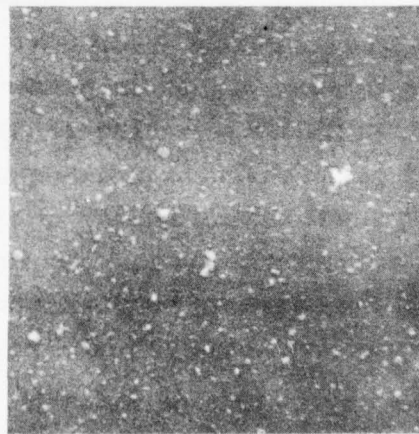
B 3μ Al<sub>2</sub>O<sub>3</sub> (C.I.)



C 3μ Al<sub>2</sub>O<sub>3</sub> (Pb)

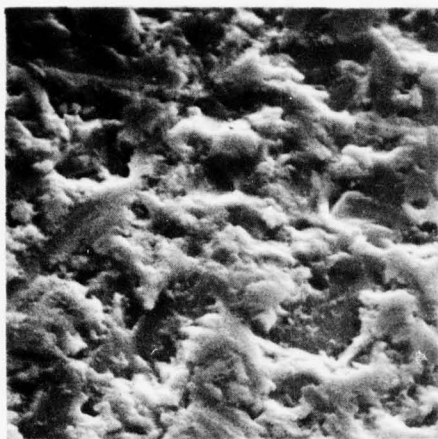


D 3μ Diamond

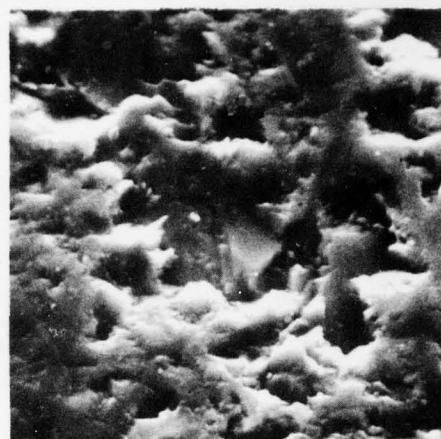


E CeO

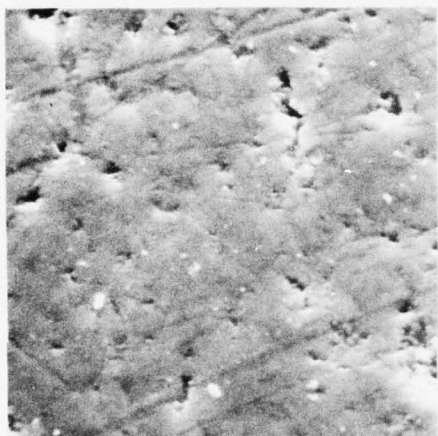
Figure 28. Scanning electron micrographs showing surface structure of (0001) LN face following successive lapping and polishing operations.



A 12μ SiC



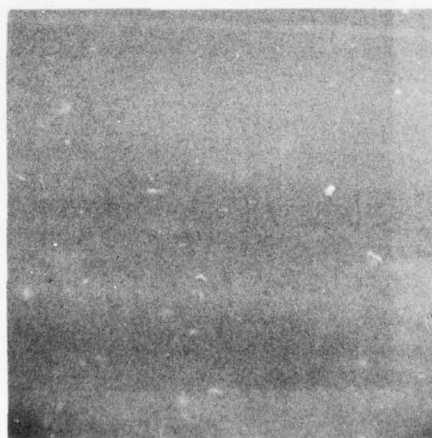
B 3μ  $\text{Al}_2\text{O}_3$  (C.I.)



C 3μ  $\text{Al}_2\text{O}_3$  (Pb)

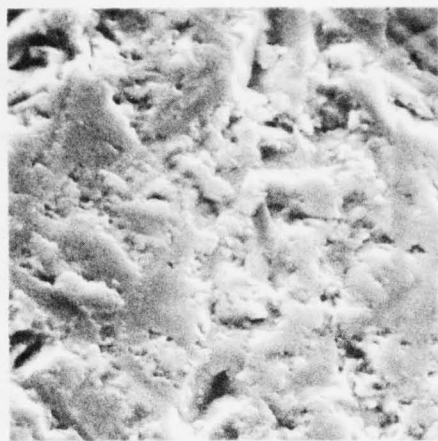


D 3μ Diamond



E CeO

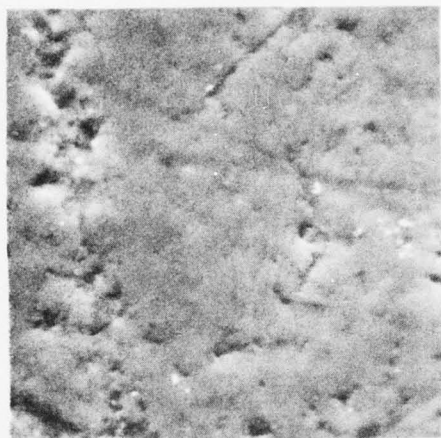
Figure 29. Scanning electron micrographs showing surface structure of (10 $\bar{1}$ 0) LN face following successive lapping and polishing operations.



A 12μ SiC



B 3μ Al<sub>2</sub>O<sub>3</sub> (C.I.)



C 3μ Al<sub>2</sub>O<sub>3</sub> (Pb)



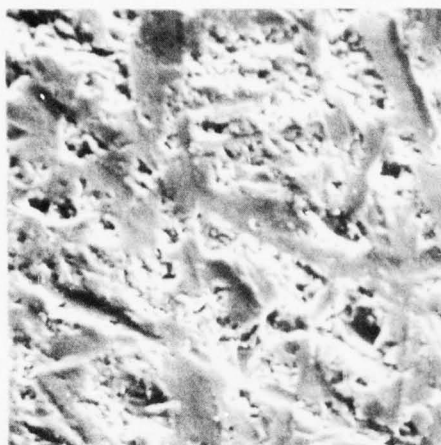
D 3μ Diamond



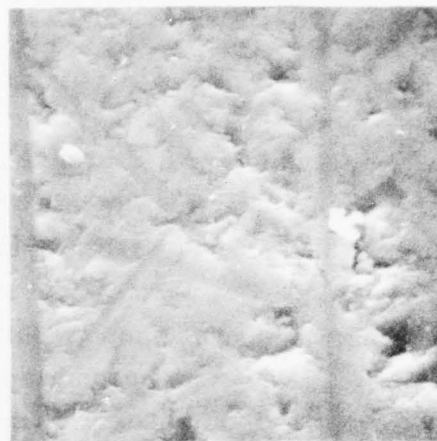
E CeO

Figure 30. Scanning electron micrographs showing surface structure of (10 $\bar{1}1$ ) LN face following successive lapping and polishing operations.





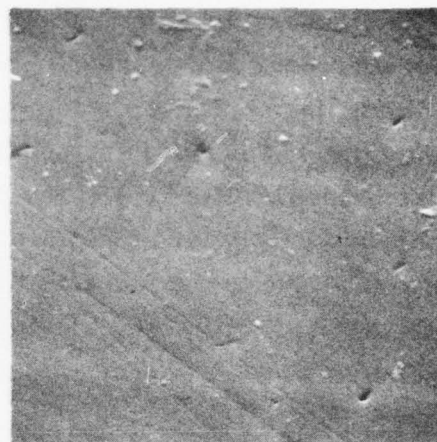
A 12μ SiC



B 3μ  $\text{Al}_2\text{O}_3$  (C.I.)



C 3μ  $\text{Al}_2\text{O}_3$  (Pb)



D 3μ Diamond



E CeO

Figure 31. Scanning electron micrographs showing surface structure of (11 $\bar{2}$ 0) LN face following successive lapping and polishing operations.



After polishing with  $3\mu\text{m}$  diamond all indications of fractured regions are gone, the surface is smooth and contains fine scratches left by the abrasive. After a final CeO polish on Pellon the scratches are gone and the surface is smooth. The surface features on the micrograph of the polished surface presumably are polishing debris and imbedded abrasive particles. Material removal during the production of the last two surfaces was clearly by plastic deformation. The extent of the plastically deformed zone and the residual stress state will be discussed later.

The stepwise development of the polished surface on a  $(10\bar{1}0)$  LN crystal face is shown in Figure 29. The increasing amount of plastic deformation as the lapping treatment becomes finer is again obvious. No differences between the  $(0001)$  and  $(10\bar{1}0)$  surface polished with  $3\mu\text{m}$  diamond and with CeO are evident. The size of the fractured zones on the lapped  $(10\bar{1}0)$  faces appear slightly larger than those on the lapped  $(0001)$  faces. This could, in part, be due to the fact that the  $(10\bar{1}2)$  cleavage plane makes a 16-degree angle with  $(10\bar{1}0)$  while the angle between the cleavage plane and the basal plane is about 60 degrees.

A similar series of scanning electron micrographs after lapping and polishing operations have been performed on  $(10\bar{1}1)$  faces is shown in Figure 30. The  $3\mu\text{m}$  diamond polished surface showed features that appear to be pits. The last micrograph in the series shows the depressions were not totally removed by final polishing in this case. The  $(10\bar{1}2)$  cleavage plane makes an angle of 16 degrees with the  $(10\bar{1}1)$  face which may again account for the larger patches on the lapped surfaces where material was removed by brittle fracture.

Figure 31 shows the  $(11\bar{2}0)$  crystal face after various treatments. The straight, flat regions in the first micrograph show where material was "smeared" by the large abrasive particles. The regions where material has been removed by brittle fracture appear smaller in this case as expected

since the cleavage plane makes an angle of 55 degrees with the machined surface. Some pits are present after  $3\mu\text{m}$  diamond polishing which persist after polishing with  $\text{CeO}$ . The surfaces with pits and scratches are clearly not acceptable to use as waveguides because the imperfections would scatter the beam. The polishing techniques used on these surfaces would have to be refined. It is interesting that the residual damage in the  $(10\bar{1}1)$  and  $(11\bar{2}0)$  polished surfaces is higher than in the  $(0001)$  and  $(10\bar{1}0)$  surfaces since all were polished simultaneously.

Precision Lattice Parameter Measurements -- The lattice parameters measured on the LN crystal faces lapped and polished in this study are listed in Table 3. As noted from the table, measurements were made after each surface finishing operation. Also included on the table are lattice parameter measurements made on commercially polished  $(0001)$  and  $(10\bar{1}0)$  faces and on a  $(10\bar{1}0)$  face with a Ti in-diffused layer on it. The precisions indicated on the table are estimates based on a measurement capability of  $\pm 4$  arc seconds with our autocollimator and the following diffraction angles:

<u>Crystal Face</u>	<u>Diffraction Plane</u>	<u><math>\theta</math> (deg)</u>	<u>Tube</u>
$(0001)$	$(00018)$	74.5	$\text{WLa}_1$
$(10\bar{1}0)$	$(60\bar{6}0)$	82.5	$\text{WLa}_1$
$(11\bar{2}0)$	$(33\bar{6}0)$	70.4	$\text{CoK}_\beta$
$(10\bar{1}1)$	$(60\bar{6}6)$	80.1	$\text{CuK}_\beta$

In every case the surface treatment caused an increase in the lattice spacing. It is the Poisson expansion due to the compressive stresses in the deformed surface layer introduced by the machining treatment. A better indication of the magnitudes of the changes in lattice spacing is given in Table 3 which lists the percentage change in spacing, i. e., the strain. The lowest strain was observed on the Z-cut  $(0001)$  face. The strain on the x-cut  $(10\bar{1}0)$  face did not change systematically with treatment. The strain on the  $(10\bar{1}0)$  face

Table 3. Effect of Surface Treatment on Interplanar Spacing\* of Lithium Niobate Crystals

Surface Treatment	Machined Crystal Face			
	c (0001) ±.0001	a <sub>-</sub> (1010) ±.00002	b <sub>-</sub> (1120) ±.00002	(1011) ±.00005
Annealed**	13.863	5.1483	5.1483	4.2444
12μ SiC on cast iron lap	13.8647	5.1498	5.1501	4.2459
3μ Al <sub>2</sub> O <sub>3</sub> on cast iron lap	13.8645	5.1499	5.1508	4.2456
3μ Al <sub>2</sub> O <sub>3</sub> on lead lap	13.8647	5.1499	5.1501	4.2458
3μ diamond on Metcloth	13.8647	5.1500	5.1491	4.2459
CeO on Pellon	13.8649	5.1501	5.1499	4.2458
Commercially polished	13.8647	5.1500	5.1499	
Ti diffused		5.1499		

\*These values are not corrected for refraction Lorentz polarization factor or for axial divergence of the incident beam.

\*\*W. L. Bond referenced by S.C. Abrahams, et. al., J. Phys. Chem. Solids, 27, 997 (1966).

Table 4. Percentage Change in Lattice Parameter (i.e., strain)  
as a Function of Surface Treatment of LN Crystals

Surface Treatment	Z Cut (0001)	X Cut (10 $\bar{1}$ 0)	Y Cut (11 $\bar{2}$ 0)	(10 $\bar{1}$ 1)
12 $\mu$ SiC on cast iron lap	.0123	.0291	.0350	.0353
3 $\mu$ Al <sub>2</sub> O <sub>3</sub> on cast iron lap	.0108	.0311	.0486	.0283
3 $\mu$ Al <sub>2</sub> O <sub>3</sub> on Pb lap	.0108	.0311	.0350	.0330
3 $\mu$ diamond on Metcloth	.0123	.0330	.0155	.0353
CeO on Pellon	.0137	.0350	.0311	.0330
Commercially polished	.0123	.0330	.0311	
Ti diffused		.0311		



was somewhat higher and did not appear to increase as the surface treatment produced a finer surface. Results obtained on the Y-cut  $(11\bar{2}0)$  and  $(10\bar{1}1)$  faces showed strains about as large as those observed on the  $(10\bar{1}0)$  face. No systematic change with treatment was observed. Results on the commercially polished samples showed the strains to be the same as those produced by us with  $3\mu\text{m}$  diamond or with  $\text{CeO}$ . The strain in the Ti diffused  $(10\bar{1}0)$  face is slightly less than that produced by polishing.

Optical Waveguiding in Polished Samples -- After fabrication the polished crystal surfaces were evaluated as optical waveguides.

The crystal was mounted on a rotating head fixture. A 60-degree rutile prism was used to couple the beam into the polished surface. For beam polarized perpendicular to the LN wafer, (TM case) the coupling angles are around  $-4$  and  $+7$  degrees for Z-cut and Y-cut wafers respectively. For beam polarized parallel to the wafer plane, the coupling angles are around  $-30$  and  $-22$  degrees for coupling into  $n_e$  and  $n_o$  respectively. The crystals are also rotated 90 degrees in the plane so that the beam propagation directions were changed.

To the best of our ability we did not detect any waveguiding in any of the surfaces polished in our lab or in the commercially polished samples. We conclude from these results that the residual stresses introduced by the lapping and polishing operations were insufficient to increase the index of refraction in the deformed layer adjacent to the polished surface. This will be discussed further in the following.

Discussion of Results -- Our results to date have shown first that lapping and polishing introduces a measurable amount of strain into the surface of a lithium niobate crystal and secondly that the strained surface, contrary to our expectations, does not guide a laser beam. We can calculate the change in the index of refraction in the deformed layer from the measurement

of strain made by the Bond x-ray technique. A change in index on the order of  $10^{-3}$  to  $10^{-4}$  should be sufficient. The change of refraction in the strained layer is related to the strain by the fourth-rank strain optic-tensor  $P_{ijkl}$  which couples the dielectric impermeability tensor  $(\frac{1}{n^2})_{ij} = \beta_{ij}$  to the strain,  $S_{kl}$  as follows:

$$\Delta\beta_{ij} = P_{ijkl} S_{kl} \quad (42)$$

Since  $\beta_{ij} = (\frac{1}{n^2})_{ij}$ ,  $d\beta_{ij} = \frac{2}{n^3} d_{ij}$ .

The strain-induced change in index is then

$$\Delta n_{ij} = -(1/2)n^3 \Delta\beta_{ij} \quad (43)$$

where the direction of propagation is perpendicular to  $X_i$  and  $X_j$ .  $n^0$  is the index of the unstrained material. The strain optic tensor and the strain tensor are written with respect to the rhombohedral  $\text{LiNbO}_3$  axes. The strain optic-tensor for  $\text{LiNbO}_3$  is, in the contracted notation:

$P_{11}$	$P_{12}$	$P_{13}$	$P_{14}$	0	0
$P_{21}$	$P_{22}$	$P_{23}$	$P_{24}$	0	0
$P_{31}$	$P_{32}$	$P_{33}$	0	0	0
$P_{41}$	$P_{42}$	0	$P_{44}$	0	0
0	0	0	0	$P_{55}$	$P_{56}$
0	0	0	0	$P_{65}$	$P_{66}$

where

$$P_{11} = P_{22} = -0.02$$

$$P_{12} = P_{21} = +0.08$$

$$P_{33} = +0.07$$

$$P_{31} = P_{32} = +0.17$$

$$P_{13} = P_{23} = +0.13$$

$$P_{14} = -P_{24} = -P_{65} = -0.08$$

$$P_{41} = -P_{42} = P_{56} = -0.15$$

$$P_{44} = P_{55} = +0.12$$

$$P_{66} = 1/2 (P_{11} - P_{12}) = -0.05$$

The principal axes of the strain-tensor lie perpendicular to and parallel to the polished surface.

The values of the measured strains perpendicular to the polished faces are (from Table 4):

Z-cut	$S_3 = 1.3 \times 10^{-4}$
X-cut	$S_1 = 3.3 \times 10^{-4}$
Y-cut	$S_2 = 3.1 \times 10^{-4}$

Consider the strain-induced change in index of refraction with light propagating parallel to the polished surface of three  $\text{LiNbO}_3$  faces: (1) Z-cut face, i. e., (0001); (2) X-cut face, i. e., (10 $\bar{1}$ 0); and (3) Y-cut face, i. e., (11 $\bar{2}$ 0).

(1) Z-Cut Face -- In this case the strain,  $S_3$ , perpendicular to the polished surface is the component measured by the Bond x-ray technique:

$$S = S_1 = S_2 = -\nu S_3$$

$$\nu = \text{Poisson's ratio} = .3$$

$$\Delta\epsilon_1 = \Delta\epsilon_2 = (p_{11} + p_{12} - \frac{1}{\nu} p_{13}) S = + 1.45 \times 10^{-5} \quad (42)$$

$$\Delta\epsilon_3 = (2p_{31} - \frac{1}{\nu} p_{33}) S = - .416 \times 10^{-5}$$

$$\Delta\epsilon_4 = \Delta\epsilon_5 = \Delta\epsilon_6 = 0$$

(2) X-Cut Face -- In this case the strain,  $S_1$ , perpendicular to the polished surface is the component measured:

$$S = S_2 = S_3 = \nu S_1$$

$$\Delta\epsilon_1 = (-\frac{1}{\nu} p_{11} + p_{12} + p_{13}) S = -2.77 \times 10^{-5}$$

$$\Delta\epsilon_2 = (-\frac{1}{\nu} p_{12} + p_{11} + p_{13}) S = + 1.57 \times 10^{-5} \quad (43)$$

$$\Delta\epsilon_3 = (1 - \frac{1}{\nu}) p_{31} + p_{33} \quad S = +3.26 \times 10^{-5}$$

$$\Delta\epsilon_4 = (-\frac{1}{\nu} - 1) p_{41} S = -6.49 \times 10^{-5}$$



(3) Y-Cut Face -- In this case the strain,  $S_2$ , perpendicular to the polished surface is measured:

$$\begin{aligned}
 S &= S_1 = S_3, \quad S_2 = -\frac{S}{\nu} \\
 \Delta\epsilon_1 &= (p_{11} - \frac{1}{\nu} p_{12} + p_{13})S = + 1.45 \times 10^{-5} \\
 \Delta\epsilon_2 &= (p_{12} - \frac{1}{\nu} p_{11} + p_{13})S = -2.57 \times 10^{-5} \\
 \Delta\epsilon_3 &= (1 - \frac{1}{\nu})p_{31} + p_{33} \quad S = -3.03 \times 10^{-5} \\
 \Delta\epsilon_4 &= (1 + \frac{1}{\nu})p_{41}S = 6.04 \times 10^{-5}
 \end{aligned} \tag{44}$$

We can now calculate the index change for light beams propagating in the strained surfaces. There are 12 possibilities that exist depending on the propagation direction and polarization. These are listed in Table 5. For simplicity we will substitute the  $X_1$ ,  $X_2$  and  $X_3$  axes for the  $X$ ,  $Y$ ,  $Z$  axes. The  $Z$ -cut face is then perpendicular to the  $X_3$  axis, the  $X$ -cut face to the  $X_1$  axis and the  $Y$ -cut face to the  $X_2$  axis.

The ordinary refractive index in the unstrained crystal are  $n_o$  and  $n_e$  respectively.  $n_o$  is in the  $X_1$  and  $X_2$  directions and  $n_e$  is along the  $X_3$  direction;  $n_o = 2.20$ ,  $n_e = 2.297$ .

$$\begin{aligned}
 \text{(i) } \underline{X_3 \text{ face}}, \quad \underline{\vec{d} = X_1}, \quad \underline{\vec{p} = X_2} \\
 \Delta n = -\frac{1}{2} n_o^3 \Delta\epsilon_2 = -7.68 \times 10^{-5} \\
 \underline{\vec{d} = X_1} \quad \underline{\vec{p} = X_3}
 \end{aligned} \tag{45}$$

Table 5. Index Change Possibilities

Polished Crystal Face, $\vec{F}$	Propagation Direction, $\vec{d}$	Polarization Direction, $\vec{p}$
Z-cut	$X_1$	$X_2$
	$X_2$	$X_3$
X-cut	$X_2$	$X_1$
	$X_3$	$X_3$
Y-cut	$X_1$	$X_1$
	$X_3$	$X_2$

$$\Delta n = -1/2 n_e^3 \Delta \beta_3 = 2.52 \times 10^{-5}$$

$$\underline{\vec{d} = X_2} \quad \underline{\vec{p} = X_1}$$

$$\Delta n = -1/2 n_o^3 \Delta \beta_1 = -7.68 \times 10^{-5}$$

$$\underline{\vec{d} = X_2} \quad \underline{\vec{p} = X_3}$$

$$\Delta n = -1/2 n_e^3 \Delta \beta_3 = +2.52 \times 10^{-5}$$

$$(ii) \underline{X_1 \text{ face}} \quad \underline{\vec{d} = X_2} \quad \underline{\vec{p} = X_1} \quad (46)$$

$$\Delta n \sim -1/2 n_o^3 \Delta \beta_1 = +1.47 \times 10^{-4}$$

In this case the indicatrix ellipse is tilted slightly with respect to the  $X_2$  and  $X_3$  axes. The rotation, however, is small.

$$\underline{\vec{d} = X_2} \quad \underline{\vec{p} = X_3}$$

$$\Delta n \sim -1/2 n_e^3 \Delta \beta_3 = -1.97 \times 10^{-4}$$

$$\underline{\vec{d} = X_3} \quad \underline{\vec{p} = X_1}$$

$$\Delta n \sim -1/2 n_o^3 \Delta \beta_1 = +1.47 \times 10^{-4}$$

$$\underline{\vec{d} = X_3} \quad \underline{\vec{p} = X_2}$$

$$\Delta n = -1/2 n_o^3 \Delta \beta_2 = -8.32 \times 10^{-5}$$

$$(iii) \underline{X_2 \text{ face}} \quad \underline{d = X_1} \quad \underline{p = X_2} \quad (47)$$

$$\Delta n \sim -1/2 n_o^3 \Delta \beta_2 = + 1.36 \times 10^{-4}$$

$$\underline{\vec{d} = X_1} \quad \underline{\vec{p} = X_3}$$

$$\Delta n \sim -1/2 n_o^3 \Delta \beta_3 = - 1.81 \times 10^{-4}$$

$$\underline{\vec{d} = X_3} \quad \underline{\vec{p} = X_1}$$

$$\Delta n = - 1/2 n_o^3 \Delta \beta_1 = - 7.42 \times 10^{-5}$$

$$\vec{d} = X_3 \quad \vec{p} = X_2$$

$$\Delta n = - 1/2 n_o^3 \Delta \beta_2 = + 1.36 \times 10^{-4}$$

Note that in some cases the change in index is positive and the magnitude of the change  $\Delta n \sim 10^{-4}$ . This should be sufficient for waveguiding provided that the affect region is sufficiently thick. Calculations<sup>1</sup> show that the thickness of the layer necessary to guide a wave depends on  $\Delta n$ . Figure 32 shows the lowest order TE waveguide modes for a substrate of refractive index  $n = 2.5$  and the waveguide layer of refractive index of 2.5001, 2.501 and 2.51 (this result is applicable for  $n=2.2$  and 2.29 since the modification is negligible). The coordinate  $W$  in  $\mu m$  is the waveguide layer thickness. In order to observe a guided wave, for  $\Delta n \sim 10^{-4}$ , as we have shown to be the case for polished LN, the thickness of the layers must be on the order of 10 microns. The thickness of the deformed layer in LN has not been measured. However, the thickness of the deformed layer in polished sapphire crystals has been measured by Hockey<sup>17</sup> using transmission electron microscopy and has been found to be on the order of  $1\mu m$ . Presumably the deformed layers in LN are of the same dimensions, and are not thick enough to cause the strained region to act as a waveguide.



AD-A034 679

HONEYWELL CORPORATE RESEARCH CENTER BLOOMINGTON MINN  
F/G 20/6  
STRAIN INDUCED WAVEGUIDING IN OPTICAL MATERIALS FOR INTEGRATED --ETC(U)  
DEC 76 D CHEN, B KOEPKE, C KNUDSON  
N00014-75-C-1097

UNCLASSIFIED

HR-47024

NL

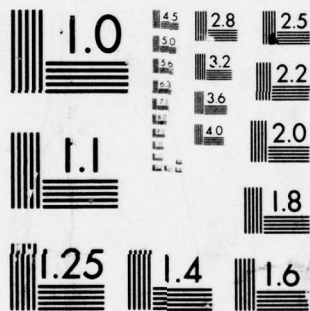
2 OF 2

AD  
A034679



END

DATE  
FILMED  
2-77



MICROCOPY RESOLUTION TEST CHART  
NATIONAL BUREAU OF STANDARDS-1963-A

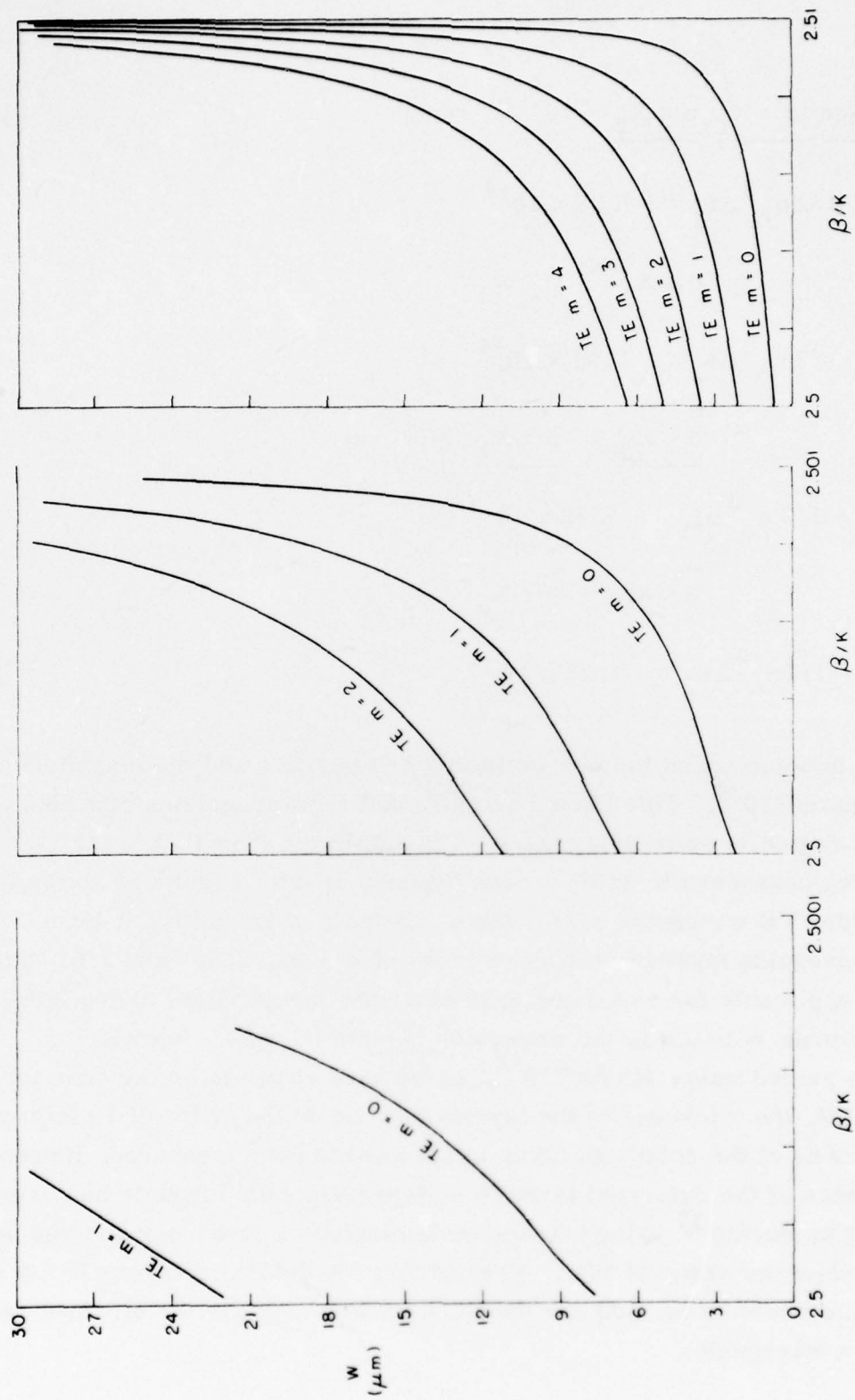


Figure 32. Waveguide effective refractive index  $\beta/k$  as a function of the thickness of the waveguide region  $W$  for substrate index of 2.5 and waveguide index of 2.5001, 2.501 and 2.51.

It is interesting to note that the measured lattice strain in the Ti diffused layer on a  $(10\bar{1}0)$  LN face is about the same as that of a polished  $(10\bar{1}0)$  face. The Ti diffused layer acts as a waveguide but the polished face doesn't. Most likely the thickness of the Ti in diffused layer is sufficient to case it to act as a waveguide.

## MEASUREMENT OF PHOTOELASTIC EFFECTS

An important part of the present research is to characterize the photoelastic effects in candidate materials for the determination of their usefulness in the integrated optics applications. A new interferrometric technique has been developed for the measurement of this effect. Results for the Corning CS-2-60 filter glass, lucite, and  $\text{LiNbO}_3$  wafers were obtained. These as well as the measurement techniques and theory are given in the following paragraphs.

### Measurement Technique and Theory

From symmetry argument, we can show that there are two nonzero coefficients in the photoelastic tensor  $p_{11}$  and  $p_{12}$  for isotropic material such as glass. In crystalline materials, symmetry considerations in the crystalline structure will result in certain reduction and relationship among the photoelastic tensor components. For instance, in  $\text{LiNbO}_3$ , as stated earlier, there are only eight independent nonzero components.

In this case the measurement of the p components will require crystals of different cuts. For our measurements, thin wafers of crystals of two given cuts (X cut means the surface of the wafer is perpendicular to the X-axis) were used, and strain is applied perpendicular to this axis. Table 6 gives examples of the orientation of crystal and beam for obtaining various p values in  $\text{LiNbO}_3$ .



Table 6. Crystal and Beam Orientation for Obtaining p Values in LN

Crystal Cut	p-values Measured	Light Beam Propagation Direction	Light Beam Polarization Direction	Direction of Strain
Z	$p_{11}$	Y	X	X
	$p_{31}$	Y	Z	X
X	$p_{12}$	Z	X	Y
	$p_{22}=p_{11}$	Z	Y	Y
Y	$p_{23}=p_{13}$	X	Y	Z
	$p_{33}$	X	Z	Z

The p's are indirectly measured by measuring the refractive index change  $\Delta n$ .  $\Delta n$  and p are related through  $\Delta n = -\frac{1}{2} n^3 p \cdot S$ .

To measure  $\Delta n$ , a Michelson interferometer arrangement was constructed. The experimental arrangement is shown in Figure 33. The laser beam was first expanded to a diameter comparable to the thickness of the sample. The final spatial filter contains a 39mm fl lens to expand the fringe pattern onto the film plane of a speedgraphic camera body.

All measurements were carried out using a 6328Å HeNe laser beam. Let the distance for the reference beam (between the beam splitter to mirror M2) and the main beam (between the beam splitter to M1) be  $\ell'$  and  $\ell$  respectively, and assuming the physical beam path length in the sample is b, the phase difference between the main beam and the reference beam is given by

$$\phi = \frac{2\pi}{\lambda} [2\ell' - 2(\ell-b) - 2bn] \quad (48)$$

where  $n$  is the refractive index of the sample and  $\lambda$  is the wavelength of the beam. If we now rotate M2 around its center in the interferometer plane (x-z plane) with a small angle  $\phi$ , then, depending on the beam position, we have

$$\ell' = \ell_0' + \phi x \quad (49)$$

This will cause a number of parallel interference lines parallel to the y-direction to appear at the film plane.

To apply the strain to the sample a four-point loading fixtured was used. The geometry of the loading on the sample is shown in Figure 34.

With this loading scheme the stress along the center line of the sample may be calculated from an elementary beam flexure formula<sup>26</sup>:

$$\sigma = \frac{My}{I}$$

where  $\sigma$  = stress along centerline

$M$  = total bending moment of sample

$I$  = moment of inertia of sample cross section

$y$  = vertical distance from neutral axis of sample

For a sample of thickness  $a$  and width  $b$  the moment of inertia is

$$I = \frac{ba^3}{12}$$

The total bending moment exerted on the sample by the four point loading scheme is  $M = fc$ .

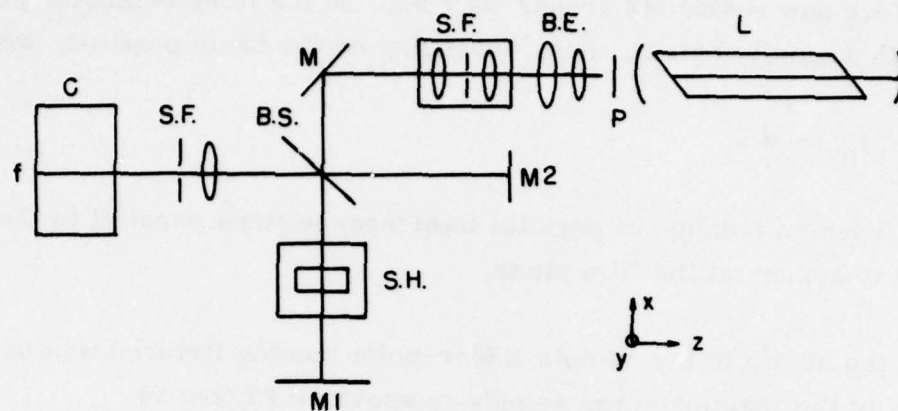


Figure 33. Schematic diagram of the Michelson interferometer for the measurement of photoelastic effect: f-film, C-camera, S.F.-spatial filter, B.S.-beam splitter, S.H.-sample holder, M1-main beam mirror, M2-reference beam mirror, M-corner reflector, B.E.-beam expander, P-polarizer, L-laser.

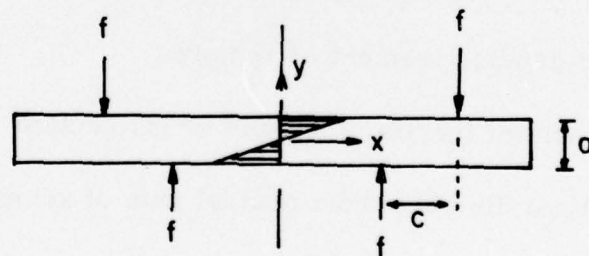


Figure 34. Geometry of four point loading on the sample of thickness  $a$ .

Therefore the stress along the centerline of the sample in the four point loading setup is

$$\sigma = \frac{12fcy}{ba^3}$$

The stress is directly proportional to the vertical distance from the neutral axis of the sample.

Therefore the change in refractive index along the centerline of the sample is

$$n(y) = \frac{-n^3}{2} p_{ij} \left( \frac{12fcy}{Eba^3} \right) \quad (50)$$

where  $E = \frac{\sigma}{\epsilon}$  is the Young's modulus.

With a tilted mirror M2 the interference pattern produced with an unstressed sample was a series of vertical fringes, the linear refractive index change when stress is applied tilts the fringes at an angle to the vertical. The phase shift produced by the stress induced  $\Delta n$  can be found by measuring the tilt angle  $\theta$  of the fringe pattern as shown in Figure 35.

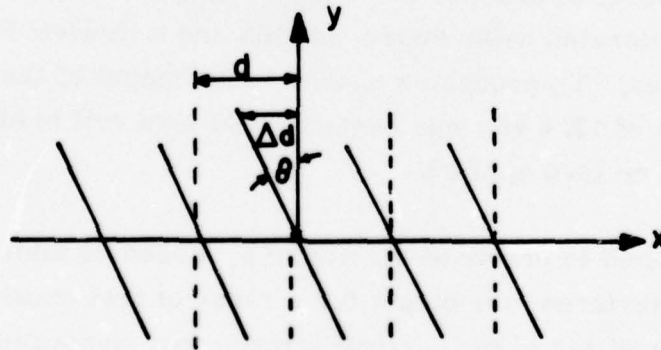


Figure 35. Tilting of fringe lines from original unloaded condition (dotted lines).



The phase shift for light beam pass through the sample at distance  $y$  from the center of the sample, along the central axis, due to stress is

$$\begin{aligned}\Delta\phi &= 2\pi \frac{\Delta d(y)}{d} \\ &= \frac{2\pi}{\lambda} 2b\Delta n(y)\end{aligned}\tag{51}$$

Therefore

$$\Delta n(y) = \frac{\lambda}{2b} \frac{\Delta d(y)}{d} = \frac{\lambda}{2db} \cdot y \tan \theta\tag{52}$$

Comparing expressions for  $\Delta n$

$$p_{ij} = \frac{\Delta d}{d} \frac{E\lambda a^3}{12fcyn^3} = \frac{E\lambda a^3}{12fcn^3} \left( \frac{\tan \theta}{d} \right)\tag{53}$$

The sample holder and loading apparatus is shown in Figure 36. It consisted of a spring-loaded plunger that could be screwed down on a Lebow 3397 25-pound load cell which in turn exerted pressure on the upper pressure bars on the sample. The Lebow 3397 Load Cell is a strain gage bridge that can be biased at a d-c level to produce a d-c signal output of 1mV (lb-force). The load cell was calibrated using known weights and a Hewlett Packard 3476B digital multimeter. To produce a change in the output of the load cell of 1mV (lb-force) a bias of 12.5 vdc was needed. The load cell bridge had an offset of 17.9 mV with no load applied.

The procedure used to arrive at a value of  $p_{ij}$  began by taking several photographs of the interferometer output for a range of test stand pressure levels. The angle of the tilting of the vertical fringes was measured on each photograph. From a measurement of horizontal spacing of the fringes on several photographs an average fringe spacing  $d'$  was found. Since this value of

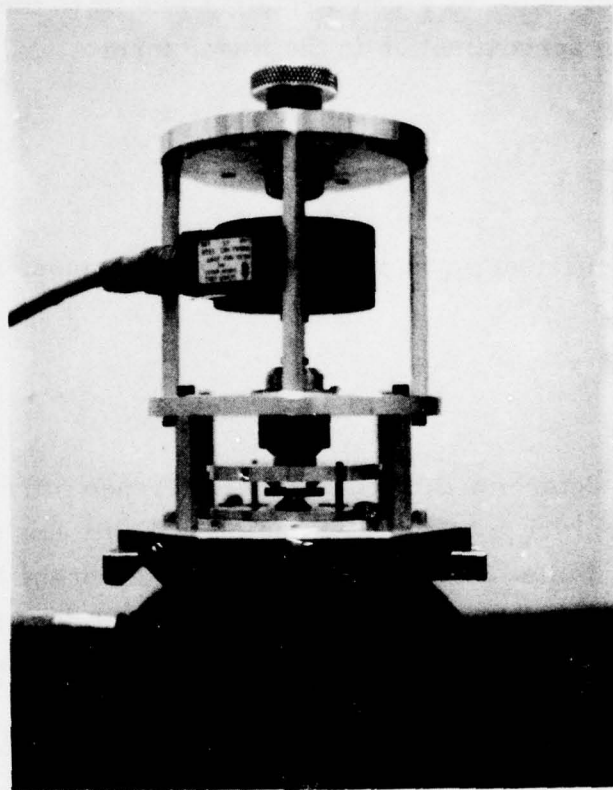


Figure 36. Sample holding and loading apparatus with a sample in place.

average spacing includes a magnification factor  $M$  due to the optical system, the true value of  $d$  referred to the sample as  $d = d'/M$ .

A graph was made of  $\frac{\tan \theta}{d}$  vs  $f$  and a straight line fit to the points was done by the least squares approximation in the linear form

$$\frac{\tan \theta}{d} = mf$$

The strain optic coefficient  $p_{ij}$  is proportional to the slope,  $m$ , of the line

$$p_{ij} = \frac{E\lambda_0 a^3}{12cn^3} m \quad (54)$$

The sign of  $p_{ij}$  was determined by tilting the reference mirror. If an inward tilt of the reference mirror (shortening the optical path length of the top of the reference beam while lengthening the optical path of the bottom of the reference beam) produced the same tilt on the fringe lines as the applied stress had, then  $p_{ij}$  was positive, otherwise  $p_{ij}$  was negative.

### Results and Discussion

Three different materials were measured. The red Corning CS-2-60 filter glass and the Lucite PMS-1 samples are isotropic and only  $p_{11}$  and  $p_{12}$  values are required. For single crystal  $\text{LiNbO}_3$ ,  $p_{11}$ ,  $p_{22}$ ,  $p_{12}$  are measured using an X-cut and a Z-cut wafer. Other quantities required wafers of different cut and were not available at the time of this measurement.

Corning CS-2-60 Glass -- Typical photographs of interference fringe pattern with and without load, as taken with the interferometer, are shown in Figure 37(a) and (b) respectively. The value of  $\tan \theta/d$  were measured for



(a)



(b)

Figure 37. Photograph of fringe lines: (a) with no load and (b) under a load of 26.1 pounds, measured on Corning CS-2-60 glass sample.



various forces used from photographs such as these and the results are plotted in Figure 38. The slope of the least-squares fitted line yields the photoelastic coefficients. The final results are:

$$p_{11} = 0.06 \quad \text{for light polarized parallel to stress direction}$$

and

$$p_{12} = 0.20 \quad \text{for light polarized perpendicular to stress direction}$$

The Young's modulus used for the above calculation are assumed<sup>27</sup> to be  $1.02 \times 10^7$  psi.

Lucite PSM-1 -- Similar measurements were made on lucite and the results are shown in Figure 39. We obtain

$$p_{11} = 0.14$$

$$p_{12} = 0.25$$

These results compare well with the manufacturer specification of  $p_{11} = 0.126$  and  $p_{12} = 0.28$ . It is interesting to note that, because of the large photoelastic effect, the sample under stress causes the beam to deflect like a prism in the vertical direction. It is necessary at times to readjust the reference mirror to compensate for this tilting effect.

LiNbO<sub>3</sub> -- Because of the limited sample size, it is not possible to completely eliminate the fringing stress field, therefore, the results can only be used as a preliminary reference in this case. As mentioned earlier, two samples, one Z-cut and one X-cut were used for this measurement. The data are shown in Figure 40. The results as well as the published data<sup>28</sup> are given in the following tabulation:

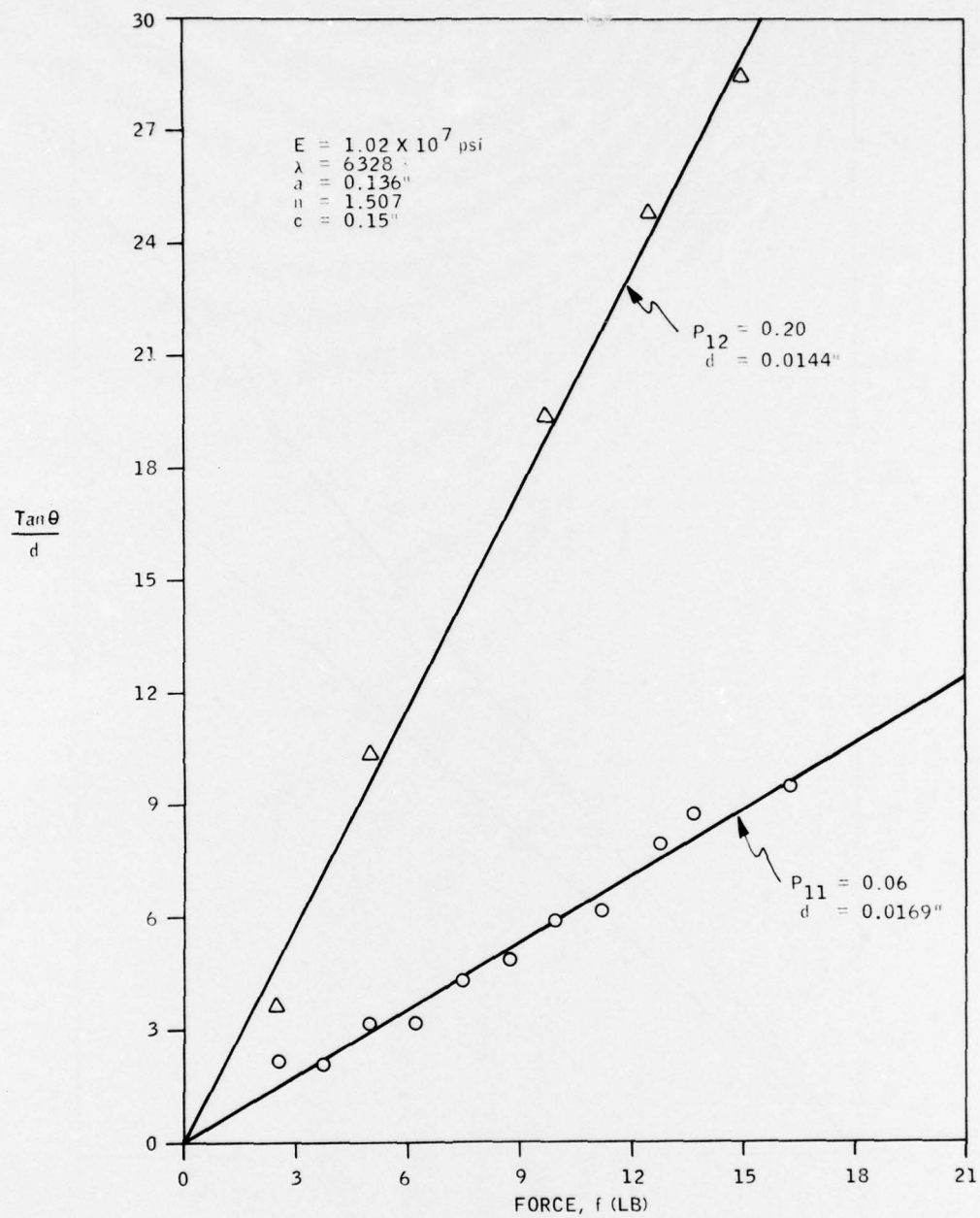


Figure 38. Photoelastic coefficients  $p_{11}$  and  $p_{12}$  of Corning CS-2-60 glass as measured from  $\tan \theta / d$  vs applied force plot.

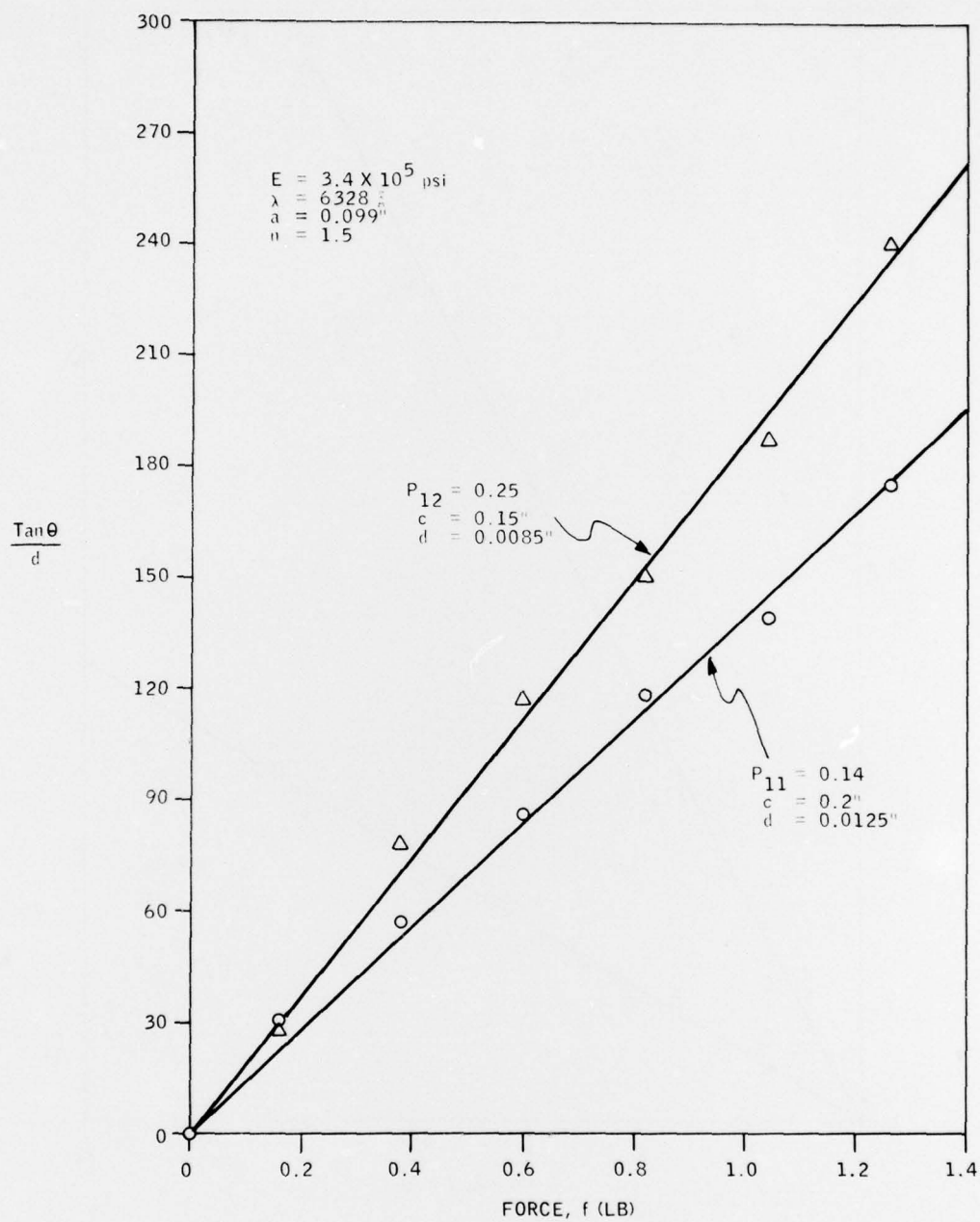


Figure 39. Photoelastic coefficients  $p_{11}$  and  $p_{12}$  of Lucite as measured from  $\tan\theta/d$  vs applied force plot.

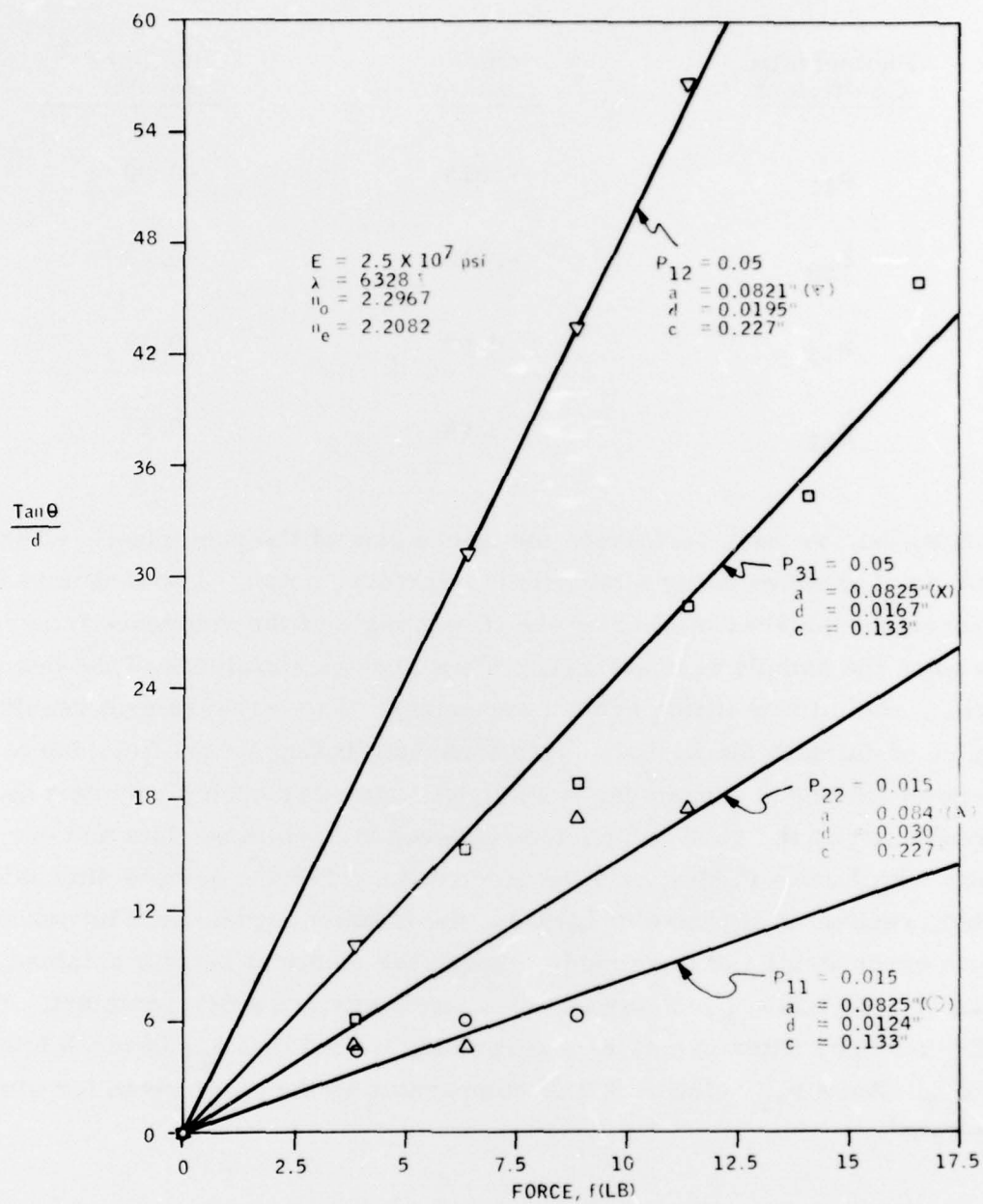


Figure 40. Photoelastic coefficient  $P_{11}$ ,  $P_{12}$ ,  $P_{31}$  as measured by the  $\tan \theta / d$  vs applied force plot.



<u>Photoelastic Coefficient</u>	<u>Our Results</u>	<u>Published<sup>28</sup> Results</u>
$P_{11}$	-. 015	-0. 02
$P_{22}$	-. 015	-0. 02
$P_{12}$	0. 05	0. 08
$P_{31}$	. 05	0. 17

In conclusion, we have performed measurements of the photoelastic effect on a number of samples using a Michelson interferometer. The technique of measurement involves measuring the tilting angle of the reference fringe lines when the sample is under load. Thus precise knowledge of the beam location, and mirror tilting are not necessary. The measurement results on samples of suitable dimensions, such that the fringing stress field due to the four-point loading arrangement is negligible, are reasonably accurate as is demonstrated by the good comparison between the published data and our results with Lucite PSM-1. On the other hand, when the sample dimension is limited, such as in the case of  $\text{LiNbO}_3$ , the fringing stress field introduced certain error in the measurements, though the identical results obtained for  $p_{11}$  and  $p_{12}$  in  $\text{LiNbO}_3$  indicate our measurements are self-consistent. For the CS-2-60 red filter glass, it is surprising to find that  $p_{11}$  is much lower than  $p_{12}$ . But a  $p_{12}$  value of 0. 2 is comparable to the value given for similar materials<sup>5</sup>.

## SECTION V CONCLUSIONS

At the inception of the research investigation on the strain-induced waveguiding in optical material for integrated optics application, we have outlined the objectives of this effort as follows:

- To determine the usefulness of the strain-induced effect for integrated optics applications.
- To obtain basic understanding and perform measurements of the effects of strain on the various physical phenomena in optical materials useful for integrated optics applications.
- To develop device concepts using selected materials and methods. The use of laser beam heating for strain-induced integrated optic circuits will be emphasized.

These objectives have guided our research effort during this period of investigation. Although we have only completed phase I and the initial part of phase II of this research work, substantial progress has been made in fulfilling these objectives. In particular, we have completed all tasks originally outlined. The task goals were:

- To develop techniques of inducing controlled residual strain for optical waveguiding.
- To measure the effect of strain on selected materials and to correlate them to the properties relevant to optical waveguiding.

- To produce strain-induced planar waveguides or channel waveguides and obtain the waveguide properties.
- To fabricate simple channel waveguide circuits by laser heating.
- To construct a microprocessor-controlled facility for automated fabrication of laser-induced channel waveguides.

In this report, we have presented the research results and progress made toward these task goals. To summarize, we have achieved the following:

- Demonstrated laser heating strain-induced (LHSI) channel waveguides in glass:
  - Techniques for the preparation of LHSI channel waveguide have been developed. This includes the determination of the laser heating temperature profile, the relationship of laser power and scanning speed to channel waveguide dimensions and techniques of annealing to stabilize the waveguide.
  - LHSI channel waveguide properties have been measured and analyzed. This includes; the waveguide modes, losses, input coupling angle dispersion and refractive index profile.
  - A model for understanding how the LHSI waveguides are formed has been developed. The strain and fictive temperature change have been analyzed.

- Developed fabrication techniques for LHSI channel waveguide microoptic circuits:
  - Constructed and tested a microcomputer controlled laser beam exposure system (LBES) for automated fabrication of LHSI waveguides.
  - Fabricated LHSI waveguides exceeding 2" in length.
  - Fabricated LHSI waveguide bends and gaps.
  - Fabricated LHSI waveguide directional couplers.
  - Constructed and tested a fiber optic data link for the micro-processor. Controlled two-dimensional translating stage for LHSI waveguide fabrication.
- Characterized the residual or induced strain in materials useful for integrated optics applications:
  - A polishing procedure to introduce a controlled surface strain in  $\text{LiNbO}_3$  has been defined. Both grinding and polishing techniques have been developed to produce residual strain.
  - X-ray characterization techniques for the determination of the polishing-induced strain have been developed. Measurement of strain using Bond techniques has been obtained.
  - The comparison of the lattice parameter changes in  $\text{LiNbO}_3$  by polishing-induced and Ti indiffused modifications has been completed.



- A new interferrometer for the measurements of the photo-elastic effects in material medium was constructed.

In conclusion, we have developed the laser beam heating technique for the fabrication of multimode waveguide circuits automated by microprocessor control. We have advanced the understanding of the effect of strain by laser heating and optical polishing. The major goals originally set forth have been achieved.

## REFERENCES

1. D. Chen and N. Marzwell, "An Investigation of PLZT for Integrated Optics", Final Tech. Report, ONR Contract No. N00014-73-C-0359, April 1, 1975.
2. T. G. Pavlopoulos and K. Crabtree, "Fabrication of Channel Optical Waveguides in Glass by CW Laser Heating", J. Appl. Phys. 45, 4964 (1974).
3. A. J. Werner, Corning Glass Works, Private Communication, and Corning Bulletin CFG.
4. L. G. Pittaway, "The Temperature Distributions in Thin Foil and Semi-infinite Targets Bombarded by an Electron Beam", Brit. J. Appl. Phys. 15, 967 (1964).
5. E. U. Condon, "Physics of the Glassy State: II-Transformation Range", Am. J. Phys. 22, 132 (1954).
6. D. Gloge and E. A. J. Marcatili, "Multimode Theory of Graded-Core Fibers", Bell System Tech. Journal 52, 1563 (1973).
7. S. Timoshenko and J. N. Goodier, Theory of Elasticity, McGraw-Hill, New York (1951), p. 55 and p. 399.
8. C. C. Hsiao, University of Minnesota, private communication (1976).
9. G. B. Hocker and W. K. Burns, "Modes in Diffused Optical Waveguides of Arbitrary Index Profile", IEEE Journal of Quantum Elect., Vol. QE-11, pp. 270-276 (June 1975).
10. H. Kogelnik and V. Ramaswamy, "Scaling Rules for Thin-Film Optical Waveguides", Appl. Opt., Vol. 13, pp. 1857-1862 (August 1974).
11. D. Marcuse, "The Impulse Response of an Optical Fiber with Parabolic Index Profile", Bell Syst. Tech. J., Vol. 52, pp. 1169-1174 (September 1973).
12. D. Chen, B. Koepke, J. D. Zook and E. Bernal G., "Multimode Optical Channel Waveguides Induced in Glass by Laser Heating", Appl. Phys. Lett. 29, 657 (1976).

13. H. Kogelnik, "Modes in Optical Resonators", in Lasers, Vol. 1, ed. by A.K. Levine (M. Dekker, New York, 1966).
14. E.A. J. Marcatili and S.E. Miller, "Improved Relations Describing Directional Control in Electromagnetic Wave Guidance", Bell Syst. Tech. J., Vol. 48, pp. 2161-2188 (September 1969).
15. D. Gloge, Appl. Optics 11, 2506 (1972).
16. D. Marcuse, "The Coupling of Degenerate Modes in Two Parallel Dielectric Waveguides", Bell Syst. Tech. J., Vol. 50, p. 1791 (July-August 1971).
17. B.G. Koepke and R.J. Stokes, J. Mater. Sci., 5, 240 (1970).
18. B.J. Hockey, J. Am. Ceram. Soc., 54, 223, (1971).
19. R.W. Rice, J. Am. Ceram. Soc., 56, 536 (1973).
20. E. Bernal G. and B.G. Koepke, J. Am. Ceram. Soc., 56, 634 (1973).
21. W.L. Bond, Acta. Cryst., 13, 814 (1960).
22. K.E. Beu, Am. Cryst. Assoc., Apparatus and Standards Committee Report No. 2 (1962).
23. G.G. Thomas, Engineering Metrology, Wiley & Sons, New York (1974) p. 245.
24. B.G. Koepke, NBS Special Publication 348, 317 (1972).
25. D.A. Pinnow, "Elastrooptical Materials", Handbook of Lasers, R.J. Pressley ed., The Chemical Rubber Co., 1971, p. 478-484.
26. A.J. Durelli, et al., Introduction to the Theoretical and Experimental Analysis of Stress and Strain, McGraw-Hill 1958, p. 107.
27. F.V. Tooley, ed., Handbook of Glass Manufacture, Ogden, 1953, p. 11.
28. J.F. Nye, Physical Properties of Crystals, Oxford, 1957, p. 244.